Molecular functions of the chromatin-remodeling factor DPF3 and its implication for myogenesis

DISSERTATION

Zur Erlangung des akademischen Grades des Doktors der Naturwissenschaften (Dr. rer. nat.)

eingereicht im Fachbereich Biologie, Chemie, Pharmazie der Freien Universität Berlin

vorgelegt von

Katherina Bellmann

aus Hannover

März 2016

Die Arbeit wurde von August 2011 bis März 2016 am Max-Planck-Institut für Molekulare Genetik sowie am Experimental and Clinical Research Center (Charité Universitätsmedizin Berlin & Max-Delbrück-Centrum für Molekulare Medizin) unter der Leitung von Frau Prof. Dr. Silke Rickert-Sperling angefertigt.

1. Gutachter: Prof. Dr. Silke Rickert-Sperling
Experimental and Clinical Research Center (Charité Universitätsmedizin Berlin & Max-Delbrück-Centrum für Molekulare Medizin)
Lindenberger Weg 80, 13125 Berlin
Mitglied des Fachbereiches Biologie, Chemie, Pharmazie der Freien Universität Berlin

2. Gutachter: Prof. Dr. Ulrich Stelzl
Institut für Pharmazeutische Wissenschaften, Universität Graz
Schubertstraße 1, 8010 Graz

Disputation am: 15.07.2016

Acknowledgements

This work was performed at the Department of Vertebrate Genomics at the Max Planck Institute for Molecular Genetics and at the Experimental and Clinical Research Center, a joint venture between the Charité Universitätsmedizin Berlin and the Max Delbrück Center for Molecular Medicine. Thank you to all the people who have helped and supported me and who have made the last years an invaluable experience.

In particular, I am deeply grateful to Prof. Dr. Silke Rickert-Sperling for giving me the opportunity to work in her group and for supervising my thesis. I would like to thank her for her constant support, her critical but also enthusiastic view on experimental data and thoughtful advice during the last years. Furthermore, I would like to give my sincere thanks to Prof. Dr. Ulrich Stelzl not only for reviewing my thesis but also for giving me the opportunity to perform experiments in his group and his engagement and openness in scientific discussions.

Also, a big thank you goes to all current and former members of the Sperling group who created a more than pleasant working atmosphere. Lab work would only be half as good without the excitement of Huanhuan Cui for all kind of experiments. I very much enjoyed our shared journey through the ups and downs of ChIP and mouse experiments. Invaluable assistance was provided by Kerstin Schulz who created a great lab atmosphere through her joyful manner. Not to forget, I left my sequencing samples in expert hands. Moreover, I would like to thank Dr. Jenny Schlesinger and Dr. Sandra Schmitz for introducing me into the work with mice and Dr. Cornelia Dorn for her supporting accompaniment and advice in practical and theoretical concerns. It was a pleasure to share the room with her. I am also grateful to Dr. Elena Cano-Rincon for introducing me into many aspects of histology. Although they were never at the same time with me in the Sperling group, this work would have been impossible without the previous experiments of Dr. Martin Lange and Ilona Dunkel's knowledge about old samples and suitable protocols. Her humor made her visits to our lab to bright spots in daily lab routine. I would like to thank Dr. Marcel Grunert not only for constant computational support and proofreading my manuscript but also for the great time we worked together at the role of Dpf3 in the kinetic splicing model. I really enjoyed the discussions with him and Sandra Appelt who had performed the computational

analysis. I am also grateful for the teamwork with Vikas Bansal who did a great job on the analysis of ChIPseq and RNAseq data. Moreover, it was a big pleasure for me to share the office and lab with Sophia Schönhals, Ashley Cooper, Sascha Werner and Andrea Behm and nice conversations with Dr. Markus Schüler and Katharina Stenin. I am very grateful to Andreas Perrot for his support in ordering lab supply and for the time we spent writing a book chapter. Finally, I would like to thank Barbara Gibas and Martina Luig for all the excellent support in dealing with administrative paperwork.

From the Max Planck Institute for Molecular Genetics, I would like to thank especially Stefanie Jehle and Dr. Jonathan Woodsmith for the good times I spent in the Stelzl group. Stefanie Jehle did a great job in introducing me into the work with yeast and supporting me with the yeast two-hybrid screen and Dr. Jonathan Woodsmith continued with great enthusiasm to teach me how to perform LUMIER assays.

From the Berlin Institute for Medical Systems Biology, I wish to thank Dr. Markus Landthaler for giving me the opportunity to perform PAR-CLIP experiments in his group. I am very grateful to Dr. Miha Milek for his practical advice and computational analysis and I would like to thank Mirjam Feldkamp for sequencing my samples. Additionally, I want to thank Dr. Lea Haarup Gregersen for sharing her expertise in siRNA testing.

My work with the mouse model was supported in various ways. Dr. Ludger Hartmann from the Max Planck Institute for Molecular Genetics and Dr. Nadja Daberkow-Nitsche from the Max Delbrück Center for Molecular Medicine provided excellent animal facilities. Special thanks go to our animal care taker Mirjam Peetz, Birgit Frenzel and Rebecca Mertke. I am also grateful to Dr. Heinrich Schrewe for providing us with CMV-cre mice. At the Experimental and Clinical Research Center, I would like to thank Sybille Schmidt and Dr. Dörte Lodka for sharing their expertise in mouse muscle dissection and May-Britt Köhler for her support in paraffin embedding.

From the Max Delbrück Center for Molecular Medicine, I am grateful to Dr. Anje Sporbert for providing an excellent facility for advanced light microscopy. Especially, I would like to thank Matthias Richter for introducing me at the confocal microscope.

Finally, I would like to thank the Sonnenfeld-Stiftung for supporting my work with a PhD fellowship.

I am deeply thankful to my family, Nico and close friends for their invaluable support and encouragement during the last years.

Contents

1 Introduction

1.1 The epigenetic transcription factor DPF3

The epigenetic transcription factor DPF3 is a member of the d4 gene family. In 1992, the first member was identified as clone d4 in a cDNA library screen from rat cerebral cortex (Buchman et al. 1992). According to its expression pattern that is restricted to neuronal tissues, the protein was named neuro-d4 (Buchman et al. 1992). Alternative names for neuro-d4 are DPF1 and BAF45b. Two years later, the second member of the d4 gene family was described as ubiquitously expressed gene in murine tissues and as an essential factor for the apoptosis response upon interleukin 3 deprivation in myeloid cells (Gabig, Mantel, et al. 1994). Therefore, the gene was named requiem (req) (Gabig, Mantel, et al. 1994). Alternative names are ubi-d4, BAF45d and DPF2. The third member of the d4 gene family, cer-d4/BAF45c/DPF3, was initally found in chicken and mouse cDNA libraries (Chestkov et al. 1996; Ninkina et al. 2001). The expression is restricted to skeletal muscle and heart in humans whereas in mouse, chicken and zebrafish, an additional expression pattern is observed in neuronal tissues (Ninkina et al. 2001; Lange et al. 2008).

The expression of the d4 gene family is conserved from nematodes to vertebrates (Chestkov et al. 1996). Characteristic domains are the N-terminal 2/3 domain with a nuclear localization signal, a putative nuclear receptor interaction domain within the linker region following the 2/3 domain, a Krüppel-like C2H2 zinc finger and a tandem PHD (plant homeobox domain) finger at the C-terminus (Figure 1.1) (Chestkov et al. 1996; Lange et al. 2008). The 2/3 domain is located within the second and third exon and unique to the d4 gene family. For DPF2, the N-terminus including the 2/3 domain, the nuclear localization signal and the nuclear receptor interaction domain has been shown to interact with BAF chromatin remodeling factor subunits (BRM, BRG1, BAF60a and hSNF5) and RelB/p52, a transcription factor of the noncanonical NF-κB signaling pathway (Tando et al. 2010). In similar experiments, DPF3 was identified as important transactivation factor for the canonical NF-κB heterodimer RelA/p50 (Ishizaka et al. 2012). A crystal structure of the C2H2 zink finger is available for DPF2 (W. Zhang et al. 2011). A two-stranded antiparallel β-sheet and an α-helix are stabilized by coordinate bonds between a zinc atom and two cysteine

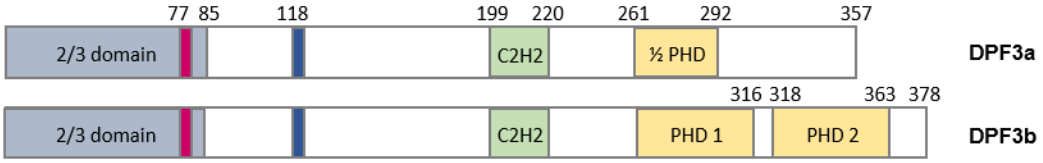

Figure 1.1: Domain structure of DPF3a and DPF3b. The nuclear localization signal is indicated in red and the nuclear receptor interaction domain in blue.

and two histidine residues. It was speculated that the zinc finger domain might mediate protein-DNA contacts (W. Zhang et al. 2011). However, at least DPF3 does not bind to DNA (H. Cui et al. 2015). The tandem PHD finger was observed in DPF1, DPF2 and in the DPF3 isoform DPF3b (Chestkov et al. 1996; Lange et al. 2008). Nuclear magnetic resonance (NMR) spectrometry of the DPF3b tandem PHD fingers bound to the histone H3K14ac peptide revealed two typical PHD folds in a face-to-back direction that are stabilized by in total four coordinated zinc atoms (Zeng et al. 2010). Both PHD modules act as one functional unit to recognize histone modifications (Zeng et al. 2010). Findings that DPF3b interacts with histone acetylation marks as well as mono- and di-methylations but not tri-methylations by Lange et al. (2008) are futher supported by the calculation of dissociation constants between the tandem PHD fingers and histone peptides (Zeng et al. 2010). Acetylation at H3K14 increases the binding affinity fourfold whereas methylation at H3K4 reduces the binding affinity 20-fold compared to unmodified peptides (Zeng et al. 2010). It is proposed that these opposing effects first recruit DPF3b as part of the BAF chromatin remodeling complex. In a second step, H3K4 undergoes methylation causing the release of the chromatin remodeling complex and subsequent transcriptional activation of target genes such as Jmjd1 and Pitx2 (Zeng et al. 2010). In contrast to DPF3b, the isoform DPF3a is characterized by a half PHD finger sequence followed by a unique C-terminus. This domain binds to transcriptional repressors of the hairy and enhancer of split-related (HESR) protein family after posttranslational phosphorylation of the serine at position 348 (H. Cui et al. 2015).

The biological functions of DPF3 are best analyzed during heart and skeletal muscle development. Initially, DPF3 was identified as disease associated gene in a genome-wide cDNA array analysis of human malformed and normal hearts (Kaynak et al. 2003). Hereby, both DPF3 isoforms were found to be upregulated in the right ventricle of patients suffering from the congenital heart disease Tetralogy of Fallot (Kaynak et al. 2003; Lange et al. 2008). In subsequent studies using the zebrafish as animal model, the role of DPF3 during heart development was elucidated (Lange et al. 2008). Upon morpholino knockdown of *dpf3*, abnormal heart looping, a thin and elongated heart tube, a poorly defined atrioventricular

boundary and reduced contractility of the heart was observed. Furthermore, transmission electron microscopy revealed some myofibrils with severely disrupted sarcomeres in ventricles of *dpf3* morphants. Myofibre disarray was also observed in somites of *dpf3* morphants and after Dpf3 siRNA knockdown in the murine skeletal muscle cell line C2C12. In addition to that, the somites in morphant zebrafish showed disrupted boundaries with crossing myofibres. The overall body posture in morphant zebrafish embryos was altered by a curved tail (Lange et al. 2008). Recently, a new role of DPF3a in hypertrophy was described in H. Cui et al. (2015). The casein kinase 2 phosphorylates DPF3a at serine 348 upon hypertrophic stimuli, thereby initiating an interaction of DPF3a with the transcriptional repressors HEY. The recruitment of BRG1 by DPF3a results in the activation of HEY downstram targets (H. Cui et al. 2015).

On molecular level, DPF3 seems to act mainly as part of the BAF chromatin remodeling complex. Tandem affinity purification in combination with mass spectrometry identified nearly all core components of the complex as interaction parters of both DPF3 isoforms (Lange et al. 2008). Moreover, chromatin binding sites for DPF3 and the BAF chromatin remodeling complex subunit BRG1 show a high overlap. Potential target genes in the vicinity of DPF3 binding sites are associated with cell proliferation, nucleosome assembly, chromatin remodeling, cardiovascular development and cytoskeleton organization (Lange et al. 2008). As the phenotype of the *dpf3* morphants is similar to phenotypes observed in Mef2a deficient zebrafish and mice (Naya et al. 2002; Y.-X. Wang et al. 2005), reporter gene assays confirming the assumed role of Mef2a as upstream regulator of Dpf3 were performed (Lange et al. 2008).

During neuronal development, the expression of DPF3 is associated with the promotion of neuronal differentiation (Lessard et al. 2007). The BAF chromatin remodeling complex in neural stem and progenitor cells is composed of several subunits including BAF53a and the PHD finger protein PHF10 (BAF45a). This BAF complex assembly is referred to as npBAF complex. Upon transition from progenitor cells to postmitotic neurons, BAF53a and PHF10 are exchanged by BAF53b and DPF1 or DPF3 forming the nBAF complex (Lessard et al. 2007).

The expression of DPF3 is associated to various diseases besides the aforementioned congenital heart defect Tetralogy of Fallot. Polymorphisms in the 5' region of DPF3 are associated with increased risk of breast cancer development, lymph node metastases, decreased age of onset, and increased tumor size (Hoyal et al. 2005). In non-malignant myeloid cells from patients with chronic lymphocytic leukemia (CLL), increased STAT5 activation results in elevated DPF3 expression levels (Theodorou et al. 2013). An enrichment of STAT5 at the DPF3 promotor in granulocytes from CLL patients compared to cells from healthy individ-

uals was observed (Theodorou et al. 2013). The single nucleotide polymorphism rs2536143 in the DPF3 gene sequence is assosiated with the development of cleft lip and palate in combination with dental anomalies (Vieira et al. 2008). DPF3 expression was also detected in colon segments from patients with Hirschsprung's disease, a developmental disorder characterized by the absence of ganglia in the distal colon, resulting in a functional obstruction (H. Liu et al. 2014). Most recently, the molecular interactions between the casein kinase 2, DPF3a, HEY and BRG1 have been unraveled (H. Cui et al. 2015). Hereby, the phosphorylation of DPF3a at serine 348 is associated with pathological cardiac hypertrophy.

1.2 The mammalian heart and skeletal muscle

Investigated under the light microscope, the mammalian heart and skeletal muscles show a similar striated microstructure. Alternating light and dark bands reflect the ordered molecular protein structure within the smallest contractile unit, the sarcomere. In the following chapter, the mammalian heart and skeletal muscles as well as the sarcomere will be described.

1.2.1 The mammalian heart

More than 5000 species belong to the class of Mammalia (D. E. Wilson and Reeder 2005), which can be found in various terrestial and aquatic habitats. Along with this wide range of natural habitats, a huge variety of body shapes and sizes is observed. Nonetheless, the heart as a central organ in the mammalian organism, shows similar structural and functional characteristics in all mammals (F. Meijler and T. Meijler 2011). It functions as a muscular pump to sustain a continuous blood flow through the whole body that supplies each cell with oxygen and transports, for example nutrients, metabolites and hormones. The heart is surrounded by the pericardium, a double layered fibroserous sac. The inner serous pericardium secrets pericardial fluid to prevent friction during the movement of the heart. The heart wall is composed of three layers, the outer epicardium, the myocardium and the inner endocardium. The myocardium consists of straited muscle that contracts upon innervation by the cardiac conduction system. This system consits of specialiced cells that form the sinus node, the atrioventricular (AV) conduction axis including the AV node and the His-Purkinje system (Dobrzynski et al. 2013). The action potentials originate from the centre of the sinus node near the junction of the superior caval vein and the right atrium. The electric signal is conducted to the secondary pacemaker, the atrioventricular node. With a short delay, allowing a time gap between atrial and ventricular systole, the action potential propagates via the His bundles and Purkinje fibres throughout the ventricles (Dobrzynski

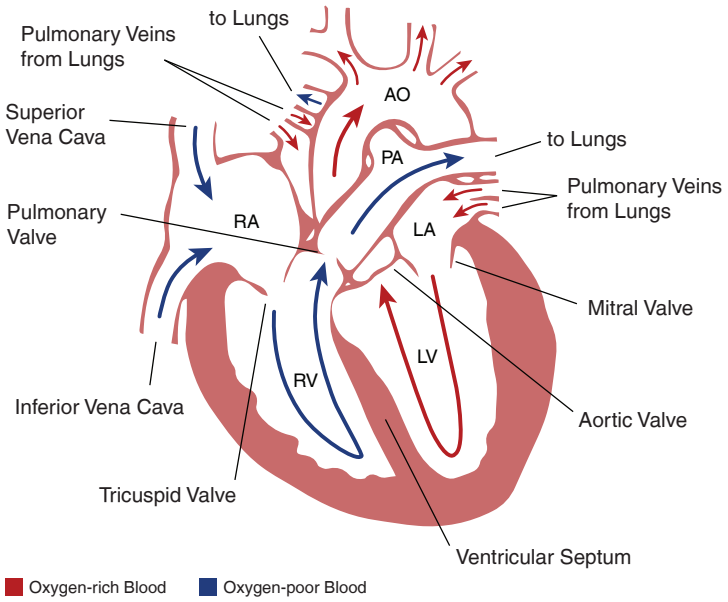

Figure 1.2: The human adult heart. AO, aorta; LA, left atrium; LV, left ventricle; PA, pulmonary artery; RA, right atrium; RV, right ventricle.

et al. 2013). The electric signal is rapidly transduced by gap junctions that allow the passage of ions through adjacent cells. The contraction of cardiomyocytes is then triggered by the depolarization-dependent influx of calcium ions (Fearnley, Roderick, and Bootman 2011).

The coordinated contractions of the four-chambered heart (Figure 1.2) are the driving force for the pulmonary circulation through the lungs and the systemic blood circulation through the rest of the body. Deoxygenated blood from the body circuit enters the right atrium via the superior and inferior caval vein and passes the tricuspid valve into the right ventricle before it flows through the pulmonary valve into the pulmonary artery towards the lungs. Oxygenated blood from the lungs returns to the left atrium through the pulmonary veins. The blood flow passes the mitral valve, the left ventricle and the aortic valve before it enters the systemic circulation via the aorta.

1.2.2 Skeletal muscles

In contrast to the heart muscle that contains mainly mononucleated cardiomyocytes (Olivetti et al. 1996), skeletal muscles form from myoblasts that fuse into multi-nucleated cells, the myofibres. Each myofibre is surrounded by a layer of fascia, the endomysium. Several myofibres form the fascicle, enclosed by the perimysium, and several fascicles give rise to the skeletal muscle, enclosed by the epimysium.

The inner organization of a myofibre includes myofibrils that consist of repeated sarcomeric units, the sarcoplasmic reticulum and the muscular cell membrane, the sarcolemma. The muscular cytoplasm is called sarcoplasm. The nuclei of the syncytium are peripherally located at the inner surface of the sarcolemma while the mitochondria are found in between the myofibrils. The sarcoplasmic reticulum, surrounding the myofibrils, stores calcium in enlarged end structures, the terminal cisternae. A pair of terminal cisternae encloses an invagination of the sarcolemma to form the T-tubule that crosses the myofibre. Action potentials are conducted along the T-tubules causing the release of calcium from the sarcoplasmic reticulum and subsequently the contraction of the muscle.

Skeletal muscles are classified according to their color, contraction speed, myosin ATPase subunit or distribution of myosin heavy chain (MyHC) isoforms (Scott, Stevens, and Binder–Macleod 2001). The color of skeletal muscles ranges from pale to dark red and reflects the content of myoglobin, an iron- and oxygen-binding protein. Red muscle fibres tend to have a high resistance to fatigue and use oxidative metabolism to generate ATP whereas pale fibres generate energy from glycolytic metabolism. The division into fast- and slow-twich fibres reflects the ability to tansduce action potentials, the speed of calcium release and uptake by the sarcoplasmic reticulum and the time to develop muscular force. Slow twitch fibres do overlap with fibres classified as dark red and fast twitch fibres tend to be more pale. The classification according to the ATPase is based on histochemical stainings under varying pH conditions and the MyHC fibre types are determined by immunohistochemistry. As skeletal muscles are usually composed from a mixture of these fibre types, the proportions of individual fibre types are given in percent.

1.2.3 The sarcomere

The smallest contractile unit in a striated muscle cell is the sarcomere (Figure 1.3). In polarized light, the borders of the sarcomere, the Z-disks, appear as dark lines within the isotropic I-bands that alternate with anisotropic A-bands. The I-bands contain thin filament proteins whereas the A-bands are composed of thick filament proteins, which partly overlap with thin filaments. The region where the thick filaments are not superimposed by the thin filaments is called the H-band that contains the thin M-line in its centre.

With more than 200 associated proteins and a connection to the T-tubular system, the Z-disk functions as important mechanosensor and mechanotransductor within the sarcomere (Knöll, Buyandelger, et al. 2011). A central protein of this network is α-actinin that crosslinks actin filaments to the Z-disk. The elastic protein desmin senses deformation within the cellular structure and bridges the Z-disk with the nuclei and in cardiomyocytes also with desmosomes (Knöll, Buyandelger, et al. 2011). The giant proteins titin and nebulin/nebulette are

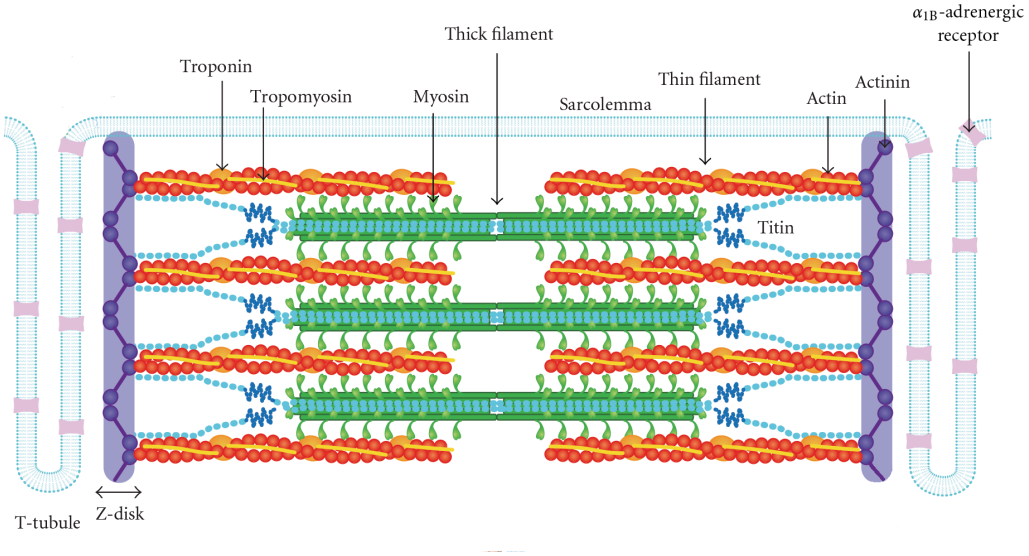

Figure 1.3: The sarcomere. (Figure taken from Kobirumaki-Shimozawa et al. (2012))

anchored in the Z-disk. Titin contributes to the sarcomeric elasticity, centeres the thick filaments and plays important roles in the assembly of the sarcomeres(Linke and Hamdani 2014). Nebulin is expressed in skeletal muscles and its function is related to the regulation of the thin filament length and the mechanical connection between adjacent myofibrils (Ottenheijm and Granzier 2010). In cardiomyocytes, the shorter homologue nebulette is expressed.

The thin and thick filaments of the sarcomere are indispensable for contraction. In skeletal as well as cardiac muscle, action potentials cause the release of calcium from the sarcoplasmic reticulum that is then bound by the troponin complex (Spudich and Watt 1971). Homologous genes with muscle type specific expression encode for the troponin complex subunits tropinin C, troponin I and troponin T. Calcium binding to the troponin complex induces conformational changes that lead to the movement of another thin filament, tropomyosin (Lehman et al. 2009). Before calcium binding, tropomyosin has covered myosin binding sites at the actin filament. The thick filament myosin consists of two heavy and four light chains (Rayment et al. 1993). The head domains of the myosin filaments bind to the free binding sites at the actin filaments. Upon the release of ADP and inorganic phosphate, the head domains are moved by the flexible neck domain resulting in shortening of the sarcomere. The actin-myosin interaction ends by binding of ATP to myosin. The myosin head moves back to its initial position by ATP hydrolysis. As long as ATP is available and calcium bound to troponin C, the myosin head repeats its movements. (Geeves and Holmes 2005) Meanwhile, calcium is actively pumped back to the sarcoplasmic reticulum until the cal-

cium ions dissociate from the troponin complex. Spring-like domains of titin contribute to restoring the initial sarcomere length (Helmes, Granzier, et al. 1996).

1.3 Gene expression and splicing

The information for all cellular components needed to create and maintain a living cell is stored in the DNA. The process to translate this information into functional molecules is called gene expression and comprises the transcription of DNA into RNA such as messenger RNA (mRNA), transfer RNA (tRNA), non-coding RNA or ribosomal RNA. If the gene encodes for a protein, the mRNA is exported from the nucleus to the cytoplasm and translated into an amino acid sequence that folds into the final protein structure. All steps of gene expression follow a defined order and are subject to tight regulatory mechanisms, important ones are described in the following.

1.3.1 Basic mechanisms of transcription

In eukaryotes, the expression of protein coding genes starts with the transcription of DNA into pre-mRNA by the RNA polymerase II (Pol II). The mammalian Pol II consists of 12 subunits named RPB1-12. The largest subunit RBP1 comprises a C-terminal domain (CTD) with 52 repeats of the heptapeptide Tyr-Ser-Pro-Thr-Ser-Pro-Ser in which the serine residues undergo process dependent phosphorylations (Cramer 2002; Napolitano, Lania, and Majello 2014). Due to charge-charge repulsions, the CTD protrudes from the globular portion of Pol II and serves as a binding platform for other transcription related proteins (Jasnovidova and Stefl 2013).

Transcription is initiated at the promotor sequence upstream of the transcriptional start site (TSS) by binding of general transcription factors, the mediator complex and unphosphorylated Pol II to form the pre-initiation complex (Cevher et al. 2014; Sainsbury, Bernecky, and Cramer 2015). By forming a transcription bubble, the pre-initiation complex switches to an open complex with separated DNA strands spanning up to 25 nucleotides (Murakami et al. 2013; Barnes et al. 2015). After phosphorylation of the serine at position 5 in the heptapeptide sequence (Ser-5), Pol II is activated and pauses in a promotor proximal position (Eick and Geyer 2013). All early transcriptional stages are accompanied and modulated by tissue, cell type or time point specific transcription factors and enhancer or repressor elements (Allen and Taatjes 2015). Elongation occurs upon release of the general transcription factors, phosphorylation of Ser-2 and binding of elongation factors (Jonkers and Lis 2015)

until a poly-adenylation signal and its binding factors cause Pol II to stop by mechanisms still poorly understood (Porrua and Libri 2015).

1.3.2 Chromatin remodeling and histone modifications

The transcriptional processes described above do not occur on naked DNA but in a chromatin environment. In order to pack almost two meters of DNA into a nucleus with a diameter of only a few micrometers, the DNA double strand is highly condensed. The first layer of compaction is the beads on a string conformation or so-called 10 nm fibre consisting of a chain of nucleosomes connected by approximately 50 bp long linker DNA. Nucleosomes consist of 147 bp DNA wrapped around an octameric histone complex assembled from two H2A-H2B dimers and one H3-H4 tetramer (Cutter and Hayes 2015). The linker histone H1 stabilizes the condensation into the 30 nm fibre (Allan et al. 1986) that undergoes further compaction into fibres with a diameter of 60–80 nm in interphase nuclei (Kireeva et al. 2004). The DNA in such higher order structures is not accessible for DNA binding molecules and called heterochromatin whereas for example transcription requires an open chromatin structure, the euchromatin.

The transition between open and closed chromatin conformations is to some extend mediated by ATP-dependent chromatin remodelers that bind to the nucleosomes via specific modifications of the histones (Hirschhorn et al. 1992). The N-terminal part of each histone gives rise to a flexible histone tail sticking out of the core nucleosomal particle. Covalent post-translational modifications on these tails constitute the histone code that can be altered by enzymes such as acetyl- and methyltransferases or deacetylases and demethylases (Bannister and Kouzarides 2011). Especially lysine residues carry various post-translational modifications of which acetylation, mono-, di- and trimethylation, ubiquitination, sumoylation and ADP-ribosylation are the most studied ones. Other well known modifications are arginine methylations or serine, threonine, tyrosine and histidine phosphorylations (Rothbart and Strahl 2014). Once the histone modifications are recognized by a chromatin remodeling complex, the nucleosomes are assembled, dissasembled, restructured or shifted along the DNA using the free energy of ATP hydrolysis. Thereby, the ATPase subunit of the remodeling complex anchors in a fixed position on the histone octamer and pushes DNA from the linker into the nucleosome resulting in a loop that propagates around the octamer and breaks the DNA-protein interactions (Clapier and Cairns 2009).

The chromatin remodeling complexes are grouped into four families based on the domain structure of their ATPase subunits (Figure 1.4). All ATPases harbour an ATPase domain consisting of a DExx and HELICc motif and subgroup specific domains. The SANT-SLIDE module is unique for ATPases of the ISWI family and ATPases assigned to CHD chromatin

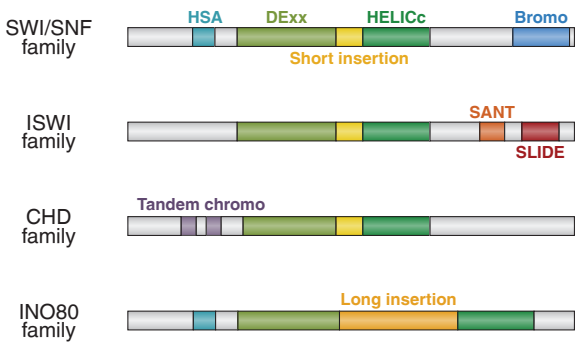

Figure 1.4: Chromatin remodeler families are defined by the domain structure of their ATPases. (Figure based on Clapier and Cairns (2009))

remodelers contain a tandem chromodomain. INO80 ATPases harbour a large insertion between the DExx and HELICc motifs and an N-terminal bromodomain. The latter is also present in ATPAses of the SWI/SNF family that carry in addition a helicase-SANT domain in their C-termini. The non-catalytic subunits of chromatin remodeling complexes modulate the recruitment, substrate affinity and catalytic activity of the chromatin remodelers. (Clapier and Cairns 2009)

The components of the SWI/SNF chromatin remodeling complexes were first discovered in yeast mutants lacking the ability to switch their mating type or to ferment sucrose (Stern, R. Jensen, and Herskowitz 1984; Neigeborn and Carlson 1984). Hence, the subunits of the SWI/SNF chromatin remodeling complexes were referred to as "mating type *swi*tching and *s*ucrose *n*on-*f*ermenting" proteins. In mammals, approximately 10 homologous proteins form two canonical SWI/SNF remodelers, namely the BAF (BRG1/BRAHMA-associated factors) and PBAF (polybromo-associated BAF) complex. These ∼2 MDa protein complexes contain an ATPase, three core subunits and seven variable proteins. BAF complexes contain either the ATPase BRG1 or BRM and the subunit BAF250 whereas PBAF complexes are assembled around BRG1 and BAF180. (G. Euskirchen, Auerbach, and Snyder 2012) Among the variable components are four different gene families with up to four members allowing cell stage and cell type specific assemblies (W. Wang et al. 1996; Lessard et al. 2007; Kaeser et al. 2008; L. Ho et al. 2009; Flores-Alcantar et al. 2011).

The readout of the histone code is only possible with a set of suitable protein domains. The subunits of the SWI/SNF remodelers comprise DNA binding domains (HMG, SANT, ARID, Krüppel), bromodomains for the recognition of acetylated lysine residues and chromodomains to read the methylation levels in the histone tails (G. Euskirchen, Auerbach, and Snyder 2012). The double PHD finger of Dpf3b has been shown to bind histone mono- and dimethylations as well as histone acetylations (Lange et al. 2008).

1.3.3 Co-transcriptional processes

The histone modification patterns at protein-coding genes are associated with the level of gene expression. Silenced genes are rich in for example tri-methylated histone 3 lysine 27 (H3K27me3) and H3K9me3 residues (Barski et al. 2007) whereas actively transcribed sequences can be predicted from the presence of H3K27ac, H4K20me1, H3K79me1 and H2BK5ac (Karlić et al. 2010). The coupling between transcription and a specific histone modification signature occurs in parts via the CTD of Pol II that recruits for example the yeast histone methyltransferases Set1 and Set2 or the histone deacetylases Set3 and Rpd3S (Hsin and Manley 2012). Not only the histone tails but also the composition of the whole nucleosome is altered during transcription. In humans, the histone chaperons HIRA as well as NAP1, FACT and ANP32E facilitate the replacement of the histones H3 and H2A by the variants H3.3 and H2A.Z, respectively (Venkatesh and Workman 2015).

Besides the crosstalk between transcription and chromatin alterations, the CTD of Pol II coordinates various steps of RNA maturation (Eick and Geyer 2013). As soon as the newly synthesized pre-mRNA extrudes from the globular part of Pol II, the 5' end is cleaved to a diphosphate and capped by adding a guanosine monophosphate that is afterwards methylated. The capping enzymes are recruited and activated by the CTD carrying Ser-5 phosphorylations. (C. K. Ho and Shuman 1999) Further pre-mRNA processing involves the excision of introns from the premature transcript by the spliceosome (see section 1.3.4) of which some splicing factors are known to be recruited by the CTD of Pol II. In yeast, it has been shown that Prp40 binds to phosphorylated heptarepeats (D. P. Morris and Greenleaf 2000) and for mammalian cells, U2AF65 and PRP19C (David et al. 2011), SFPQ and NONO (Emili et al. 2002) and SRSF3 (Mata and Kornblihtt 2006) are examples for CTD-recruited splicing factors. Splicing factors are not only recruited in a cotrancriptional manner but also catalytically active. 80 % of active spliceosomes are found at chromatin and the cotranscriptional splicing frequency exceeds 75 % in human genes. The remaining 20 % of active spliceosomes perform post-transcriptional splicing in nuclear speckles. (Bentley 2014; Brugiolo, Herzel, and Neugebauer 2013) Finally, some of the poly(A) adding enzymes and nuclear export proteins are recruited by the CTD at the end of transcription to finish the mRNA maturation process and to export the transcripts into the cytoplasm. (Hsin and Manley 2012; Eick and Geyer 2013)

1.3.4 The spliceosome

Most eukaryotic protein-coding genes are transcribed into pre-mRNAs comprising protein-coding exons and non-coding introns. To gain translatable mRNAs, the introns are removed

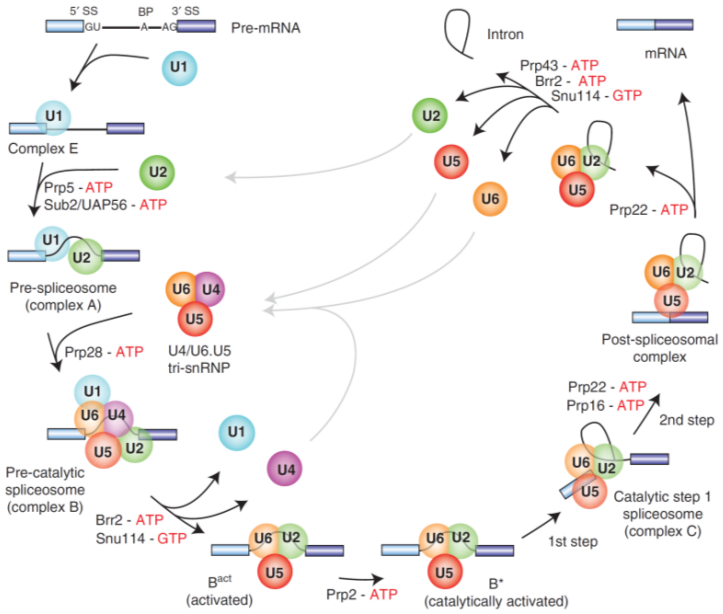

Figure 1.5: Assembly and disassembly of the metazoan spliceosome. Exons are indicated by boxes wheras introns are represented by a line. Non-snRNP complexes are not shown. (Figure taken from Will and Lührmann (2011))

by a dynamic ribonucleoprotein machinery, the spliceosome. In total, the human spliceosome is composed of 244 subunits that assemble, exchange or disassemble during the step-wise splicing reaction (Figure 1.5). 141 of these splicing factors are considered as core-proteins whereas more than 100 proteins have assisting or regulatory functions. The splicing factors are organized in subcomplexes with specific roles during the splicing process. Five spliceosomal complexes are grouped around small nuclear RNAs (snRNA) giving rise to the small nuclear ribonucleoproteins (snRNP) U1, U2, U4, U5 and U6 that are essential for the splice site selection and the catalytic activity. (Wahl, Will, and Lührmann 2009; Will and Lührmann 2011; Hegele et al. 2012)

The first step of the splicing reaction is the recognition of the 5' and 3' splice sites that are characterized by the highly conserved dinucleotides GU and AG, respectively. Less than 0.4 % of human introns carry the dinucleotide AT at the 5' splice site and AC at the 3' splice sites. These introns are spliced outside the nucleus by the minor spliceosome consisting of U11, U12, U4atac/U6atac and U5 snRNPs. (König et al. 2007) As U2- and U12-dependent splicing follows the same principle, only U2-dependent splicing will be described in detail. If not stated otherwise, the protein names refer to the human spliceosome.

The 5' splice site or donor site is recognized by the U1 snRNP via base pairing of the U1 snRNA at position -3 to +6 of the exon-intron boundary. (De Conti, Baralle, and Buratti

2013) This RNA-RNA interaction is supported by protein subunits of the U1 snRNP and some members of the SR protein family. (Staknis and Reed 1994; S. Cho et al. 2011) The intron-exon boundary at the 3' splice site or acceptor site is not only defined by the intronic dinucleotid AG followed by an exonic G but also by the branch point sequence and a 15-20 bp long polypyrimidine tract. The branch point adenosine and the polypyrimidine tract are located within 50 bp upstream of the intron-exon junction and marked by the splicing factors SF1 and U2AF65, respectively. (Gao et al. 2008; Selenko et al. 2003) U2AF65 is the large subunit of the U2AF heterodimer. The small subunit U2AF35 binds weakly to the 3' splice site. (Kielkopf et al. 2001) This early assembly of the U1 snRNP and the non-snRNP splicing factors is called the E complex.

After splice site recognition, a donor and acceptor site are irreversibly paired during A complex formation (Lim and Hertel 2004; Hodson et al. 2012) and the branch point adenosine is exposed inside the U2 snRNP (Feltz et al. 2012). These rearrangements are ATP-dependent and require the ATPases/helicases PRP5 and UAP56 (Will, Urlaub, et al. 2002; Perriman et al. 2003; Shen et al. 2008).

Subsequent to the A complex, the U4/U6.U5 tri-snRNP enters the prespliceosomal assembly giving rise to the precatalytic B complex. (Wahl, Will, and Lührmann 2009; Feltz et al. 2012). The association of the preformed U4/U6.U5 tri-snRNP requires the phosphorylated ATPase/helicase PRP28 (Mathew et al. 2008). The yeast Prp28 is known to destabilize the base pairing between the U1 snRNA and the 5' splice site resulting in the dissociation of the U1 snRNP and enabling a new base pairing between the donor site and the U6 snRNA (Staley and Guthrie 1999; Cordin and Beggs 2013). This base pairing is only possible after unwinding the U4/U6 snRNA duplex by the helicases U5-200kD/Brr2 and UAP56 (Laggerbauer, Achsel, and Lührmann 1998; Shen et al. 2008; Y.-C. Liu and Cheng 2015). The U4 snRNP dissociates during these rearrangements. Further structural changes towards the activated B complex (B^{act}) include base pairings between the U2 and U6 snRNAs and interactions between the 5' exon and the U5 snRNA (Wyatt, Sontheimer, and Steitz 1992; Rhode et al. 2006; Anokhina et al. 2013). The stable association of the U5 and U6 snRNAs requires the Prp19-associated complex NTC (nineteen complex) in yeast (Chan et al. 2003) and human cell extracts depleted of the Prp19/CDC5 complex fail to form activated B complexes (Makarova, Makarov, Urlaub, et al. 2004). The transition into the catalytically active B* complex is mainly studied in yeast. This process is initiated by the ATPase Prp2 and accompanied by several protein subunit exchanges to form the catalytic core (Warkocki et al. 2009; Makarov et al. 2002). During these arrangements, the SF3a and SF3b subcomplexes dissociate from the branch point and Prp2 proofreads the juxtaposition of the branch point and the 5' splice site (Lardelli et al. 2010; Wlodaver and Staley 2014).

Figure 1.6: Conserved sequences at U2-type introns from metazoans. R, purine; Y, pyrimidine. (Figure based on Will and Lührmann (2011))

During the first catalytic reaction, the 2' hydroxy group of the branch point adenosine attacks the 5' phosphate of the donor site resulting in a 5'-2' phosphodiester bond and cleavage of the exon-intron boundary (Will and Lührmann 2011). Subsequent structural rearrangements are driven by the ATPase Prp16 (shown in yeast) and result in repositioning the 5' exon and the intron lariat, which is still attached to 3' exon, for the second catalytic reaction (Schwer and Guthrie 1992; Mefford and Staley 2009). Hereby, the 3'-OH group at the 5' exon attacks the acceptor splice site. The spliceosomal conformation at this stage is referred to as the C complex.

The release and disassembly of the spliceosome is best studied in the yeast model. After ligation of the 5' and 3' exon, the mRNA is released by the ATPase Prp22 (Schwer 2008). The remaining intron lariat as well as the spliceosomal subunits U2, U5 and U6 are disassembled by nineteen complex related proteins in an APT dependent manner (Tsai et al. 2005; Horowitz 2012).

1.3.5 Alternative splicing

The ability to form multiple transcripts from a single gene is based on alternative promotor usage, alternative splicing or the usage of alternative poly-adenylation signals (Keren, Lev-Maor, and Ast 2010). Approximately 95 % of all human multiexon genes give rise to transcripts that undergo alternative splicing (Pan et al. 2008; E. T. Wang et al. 2008). Hereby, several classes of alternative splicing events are distinguished: skipping of single or multiple exons, mutually exclusive exons, alternative 3' or 5' splice site usage and intron retention. Underlying causes are a combination of sequence inherent determinants and the competition of regulatory factors.

Important sequence determinants are the conservation scores of the splice sites (Figure 1.6). The strength of the splice sites is calculated based on the nucleotide sequence at position -3 to +6 at the 5' exon-intron boundary and position -20 to +3 at the 3' intron-exon boundary, the conservation, length and position of the branch point sequence and of the polypyrimidine tract (Yeo and Burge 2004; M. Wang and Marín 2006; Gao et al. 2008; Corvelo et al. 2010; Shepard et al. 2011).

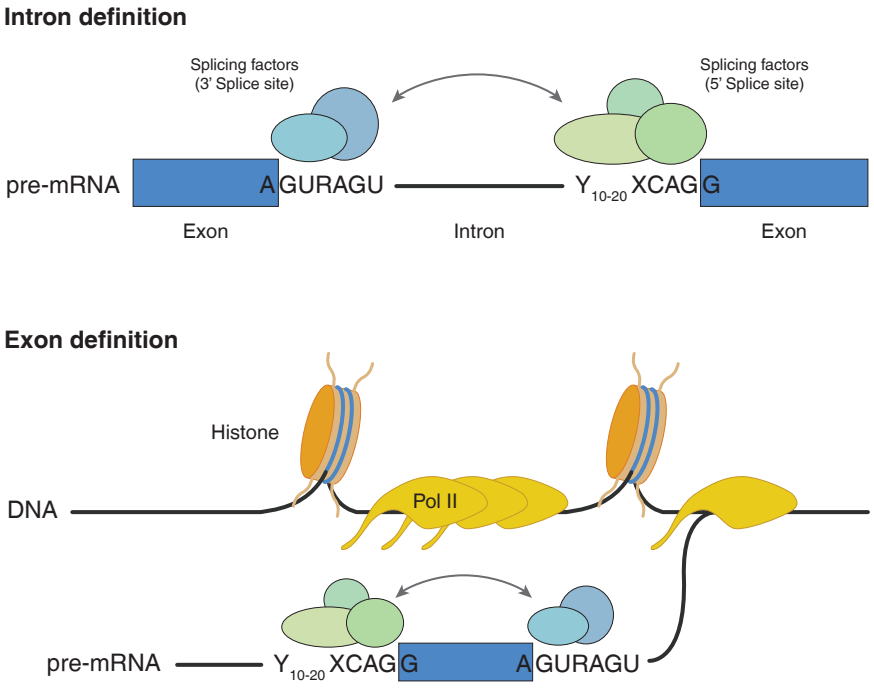

Figure 1.7: Proposed mechanism for intron and exon definition. Short introns are recognized as one unit by the spliceosome on pre-mRNA level. If the introns are long, the splice sites are marked by exon definition. This process is modulated by nucleosomes and their binding factors. (Figure based on Naftelberg et al. (2015))

Further sequence inherent factors are the length of the exon and the flanking introns and the GC content within these regions (Naftelberg et al. 2015). In low-GC content regions, the introns tend to be long and the exonic regions have a higher GC content compared to the flanking introns. In high-GC content regions, the introns tend to be short and both exons and introns have a similar GC content. In the first scenario, splice sites are selected by a mechanism that is referred to as exon definition and weak splice sites as well as low GC contents result in exon skipping. In the second condition, the spliceosome recognises the intron by the intron definition mechanism (Figure 1.7). (Berget 1995; Hertel 2008; Amit et al. 2012)

An additional layer of splicing regulation are *cis*-acting RNA sequence elements (Hertel 2008). Exonic or intronic splicing enhancer elements are recognized by splicing factors such as serine/arginine-rich proteins whereas exonic or intronic splicing silencer elements are bound by repressors such as splicing factors of the snRNP protein family and polypyrimidine tract binding proteins (Oberstrass et al. 2005; Busch and Hertel 2012; Erkelenz et al. 2013).

The impact of epigenetics on alternative splicing will be described in the next section.

1.3.6 Epigenetic regulation of alternative splicing

In recent years, the influence of epigenetic modifications such as CpG methylations or histone modifications on alternative splicing has been investigated (Naftelberg et al. 2015).

As outlined in section 1.3.3, most splicing events occur co-transcriptionally. Besides the recruitment of splicing factors by the C-terminal domain of Pol II, the splicing outcome is affected by the elongation rate of Pol II suggesting a kinetic splicing model (Figure 1.8) (Naftelberg et al. 2015). In most cases, a reduced elongation rate or pausing of Pol II results in inclusion of exons with weak splice sites (Ip et al. 2011; Shukla et al. 2011). A natural barrier for Pol II are the nucleosomes that are preferably positioned at exonic sequences (Schwartz, Meshorer, and Ast 2009). Chromatin remodeling complexes read histone modifications and open the chromatin structure to allow the passage of Pol II (see section 1.3.2). Alterations in histone modifications or the chromatin structure change the splicing patterns of alternatively spliced transcripts. Hnilicová et al. (2011) observed a reduced Pol II elongation rate and altered splicing outcome in approximately 700 human genes upon treatment with histone deacetylase inhibitors. Also alterations in chromatin remodeling complexes such as the SWI/SNF complex go along with alternative splice site selection (Batsché, Moshe Yaniv, and Christian Muchardt 2006; Tyagi et al. 2009; Zraly and Dingwall 2012). However, the reduction of the Pol II elongation rate by the BAF chromatin remodeling complex seems to be independent from the ATPase activity (Batsché, Moshe Yaniv, and Christian Muchardt 2006). The crosstalk between chromatin and alternative splicing is further supported by an enrichment of nucleosomes not only at constitutively spliced exons but also at alternatively spliced exons with a high GC content and weak splice sites (Amit et al. 2012; Huang et al. 2012).

An alternative but not mutually exclusive model for the connection between histone modifications and alternative splicing is the chromatin adapter model (Figure 1.8) (Luco, Allo, et al. 2011). Histone modification patterns are not only associated with gene expression levels but also with alternative splice site selection. For instance, the H3K36me3 level is in general increased over exons compared to intronic sequences but lower at alternatively spliced exons in comparison with constitutively spliced exons (Kolasinska-Zwierz et al. 2009). Moreover, H3K36me3 is recognized by the histone readers MRG15 and Psp1 that recruit the splicing factors PTB and Srsf1, respectively (Luco, Pan, et al. 2010; Pradeepa et al. 2012). Further known adapter molecules between chromatin and the splicing machinery are the chromatin remodeler CHD1 and the BS69 protein (Sims et al. 2007; R. Guo et al. 2014). CHD1 recruits components of the U2 snRNP and BS69 binds to subunits of the U5 snRNP and

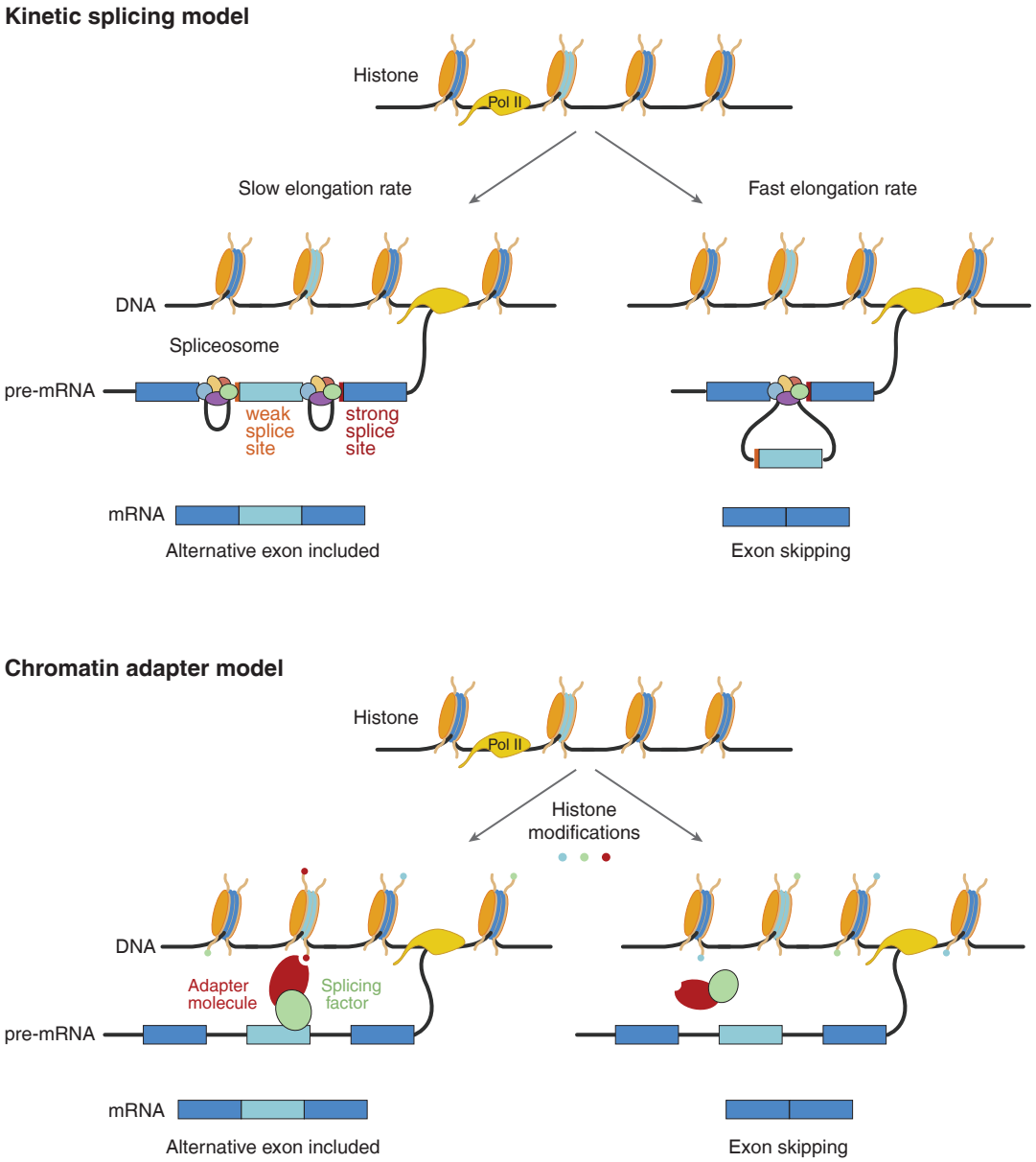

Figure 1.8: Splicing of alternative exons. Kinetic splicing model: A fast elongation rate of the RNA polymerase II (Pol II) promotes the selection of strong splice sites and skipping of exons with weak splice sites. A slow elongation rate or pausing of Pol II allows the recruitment of splicing factors to weak splice sites and the inclusion of the alternatively spliced exon. **Chromatin-adaper model:** Histone readers recruit splicing factors that favor or prevent the inclusion of the alternative exon. Here, only the chromatin-adapter induced inclusion is shown. (Figure based on Luco, Allo, et al. (2011) and H.-L. Zhou et al. (2014))

promotes intron retention. A direct interation between unmodified or specific acetylation or methylation marks at histone 3 is reported for the splicing factor SRSF3 (Loomis et al. 2009). In addition, several computational models exist for the prediction of exon inclusion or exclusion based on combinations of histone modifications (Enroth et al. 2012; Shindo et al. 2013; Zhu et al. 2013; W. Chen et al. 2014).

Besides histone modifications, CpG methylations are associates with alternative splice site selection. As described in section 1.3.5, exons and introns are characterized by different or equal GC contents. In both contexts, the exons show an elevated CpG methylation level (Maor, Yearim, and Ast 2015). In a study analyzing DNA methyltransferase deficient mouse embryonic stem cells and methylated or demethylated mini-genes inserted into human embryonic kidney cells, Yearim et al. (2015) showed that an elevated CpG methylation level leads to H3K9 trimethylation. Subsequent binding of HP1 recruits splicing factors and results in a change of exon inclusion or exclusion.

Not only the adapter model but also the kinetic splicing model can be applied to DNA methylations. A high CpG methylation level in the human CD45 gene prevents binding of the Pol II stopping protein CTCF and further genome-wide analysis of CTCF-depleted cells revealed a release of pausing Pol II and subsequent exon exclusion (Shukla et al. 2011). A second example for a DNA methylation binder that alters the Pol II elongation rate is MeCP2. MeCP2 recruits histone deacetylases and the following histone hypoacetylation seems to decrease the Pol II elongation rate, favouring exon inclusion (Maunakea et al. 2013).

1.4 Aim of the thesis

In the past, the roles and functions of Dpf3 have been investigated in cell culture models and in the zebrafish demonstrating its impact on heart and skeletal muscle formation (Lange et al. 2008). To elucidate if Dpf3 has similar functions in the mammalian system, a conditional knockout mouse strain was generated. In this strain, the second exon of Dpf3 is flanked by loxP sites. Within this thesis, the conditional knockout mouse strain was mated with a cre deleter strain resulting in excision of the second exon and a frame shift start as well as a stop codon in the following two exons. The final DPF3$^{-/-}$ mouse strain was examined on genomic, phenotypic and histologic level. Moreover, genome-wide RNA sequencing of samples from DPF3$^{-/-}$ mice and wild type control animals revealed the impact of Dpf3 on gene expression and alternative splicing.

A second project aimed to investigate the role of DPF3 in the regulation of alternative splicing. Initial experiments identified several splicing factors as binding partners of DPF3.

In light of recent advances in understanding the interplay between epigenetics and alternative splicing (see section 1.3.6), the following hypotheses were experimentally tested:

1) Dpf3 is a chromatin adapter molecule that recruits splicing factors to the nascent transcript.

2) Dpf3 as part of the BAF chromatin remodeling complex influences the splice site selection by altering the elongation rate of Pol II.

3) DPF3 influences the splicing outcome by binding to the pre-mRNA. The recruitment of splicing factors, alterations in the secondary RNA structure or competition for binding sites with splicing enhancers or silencers alters the splice site selection.

2 Materials and methods

2.1 Reagents and consumables

2.1.1 Reagents

1 kb DNA Ladder	New England Biolabs, USA
100 bp DNA Ladder	New England Biolabs, USA
2-methylbutane	Carl Roth, Germany
4-Thiouridine (4SU)	Sigma-Aldrich, USA
Adenine	Sigma-Aldrich, USA
Agencourt® AMPure® XP beads	Beckman Coulter, USA
Ampicillin	Carl Roth, Germany
Anti-Flag M2 Affinity Gel	Sigma-Aldrich, USA
Anti-HA high affinity from rat IgG	Roche, Switzerland
Ascorbic acid	Sigma-Aldrich, USA
Bacto agar	BD Biosciences, USA
Bacto peptone	BD Biosciences, USA
Bacto yeast extract	BD Biosciences, USA
Bovine serum albumin	Sigma-Aldrich, USA
Chloramphenicol	Sigma-Aldrich, USA
Chloroform	Merck Millipore, Germany
Citric acid	Sigma-Aldrich, USA
Claycomb Medium	Sigma-Aldrich, USA
D-Luciferin sodium salt	Sigma-Aldrich, USA
Dimethylsulfoxide (DMSO)	Sigma-Aldrich, USA
Dulbecco's modified Eagle's medium (DMEM)	Thermo Fisher Scientific, USA
Dulbecco's phosphate buffered saline (PBS) w/o Ca/Mg	Thermo Fisher Scientific, USA
Dynabeads® Oligo$(dT)_{25}$	Thermo Fisher Scientific, USA
Dynabeads® Protein A for Immunoprecipitation	Thermo Fisher Scientific, USA
Dynabeads® Protein G for Immunoprecipitation	Thermo Fisher Scientific, USA
Entallan® New	Merck Millipore, Germany
Eosin Y Solution	Sigma-Aldrich, USA

Eucalyptol	Sigma-Aldrich, USA
EZ-Link™ Biotin-HPDP	Thermo Fisher Scientific, USA
Fetal bovine serum (Lot 11A568 for HL-1)	Sigma-Aldrich, USA
Fetal bovine serum (Lot W0036 for C2C12, HEK293T)	Merck Millipore, Germany
Fibronectin from bovine plasma	Sigma-Aldrich, USA
Fluoromount™ Aqueous Mounting Medium	Sigma-Aldrich, USA
Gelatin	Sigma-Aldrich, USA
GelRed™	Biotium, USA
Glucose monohydrate	Merck Millipore, Germany
Glutathione Sepharose Matrix	GE Healthcare, United Kingdom
Hematoxylin solution according to Delafield	Sigma-Aldrich, USA
Histidine	Sigma-Aldrich, USA
Hydrogen peroxide solution, 30 % w/w	Sigma-Aldrich, USA
Kanamycin	Sigma-Aldrich, USA
L-broth (powder)	MP Biomedicals, USA
L-Glutamine	Thermo Fisher Scientific, USA
LB medium agar (powder)	MP Biomedicals, USA
Leucine	Sigma-Aldrich, USA
Linear polyethylenimine (PEI) 25 kDa	Polysciences, Inc., USA
Lipofectamine 2000	Thermo Fisher Scientific, USA
Midori Green Direct	Nippon Genetics, Japan
NuPAGE LDS sample buffer	Thermo Fisher Scientific, USA
Paraformaldehyde	Sigma-Aldrich, USA
Penicillin/Streptomycin	Thermo Fisher Scientific, USA
Pierce™ Streptavidin, Horseradish Peroxidase Conjugated	Thermo Fisher Scientific, USA
Roti®-Phenol-Chloroform-Isoamyl alcohol (25/24/1)	Carl Roth, Germany
Skim Milk Powder	Sigma-Aldrich, USA
Spectra™ Multicolor Broad Range Protein Ladder	Thermo Fisher Scientific, USA
Super Signal™ West Femto Chemiluminescent Substrate	Thermo Fisher Scientific, USA
Super Signal™ West Pico Chemiluminescent Substrate	Thermo Fisher Scientific, USA
Tetracycline hydrochloride	Sigma-Aldrich, USA
Tragacanth	Sigma-Aldrich, USA
Triton™ X-100	Sigma-Aldrich, USA
TRIzol® Reagent	Thermo Fisher Scientific, USA
Trypsin-EDTA (0.25 %)	Thermo Fisher Scientific, USA
Tryptophan	Sigma-Aldrich, USA
Uracil	Sigma-Aldrich, USA
Xylenes	Sigma-Aldrich, USA

Yeast nitrogen base	BD Biosciences, USA

2.1.2 Enzymes

AMV reverse transcriptase	Promega, USA
Antarctic Phosphatase	New England Biolabs, USA
BamHI	New England Biolabs, USA
BP Clonase enzyme mix	Thermo Fisher Scientific, USA
EcoRI	New England Biolabs, USA
FastDigest Bsp1407I	Thermo Fisher Scientific, USA
LR Clonase enzyme mix II	Thermo Fisher Scientific, USA
NotI	New England Biolabs, USA
Phusion High-Fidelity PCR Master Mix with HF Buffer	Thermo Fisher Scientific, USA
Proteinase K	Sigma-Aldrich, USA
RNase A	Sigma-Aldrich, USA

2.1.3 Antibodies

Primary antibodies	**Source**	**Amount/dilution**	**Company**
Anti-actinin	mouse, monoclonal	IF: 1:400	Sigma (A7811)
Anti-desmin	mouse, monoclonal	IF: 1:25	Sigma (D1033)
Anti-Flag(M2)	mouse, monoclonal	WB: 1:2000, PAR-CLIP: 0.25 mg/ml	Sigma (F3165)
Anti-GST tag	rabbit, polyclonal	WB: 1:500	Invitrogen (71-7500)
Anti-H3K4me1	rabbit, polyclonal	ChIP: 2 μg	Abcam (ab8895)
Anti-H4K16ac	rabbit, polyclonal	ChIP: 2 μg	Millipore (07-329)
Anti-HA tag	rat, monoclonal	WB: 1:2000	Roche (11867423001)
Anti-fast myosins (MY-32)	mouse, monoclonal	IF: 1:100	Sigma (M4276)
Anti-slow myosins (NOQ7.5.4D)	mouse, monoclonal	IF: 1:100	Sigma (M8421)
Anti-pDpf3a	rabbit polyclonal	IF: 1:500	Thermo Fisher Scientific, custom generated
Anti-tropomyosin	mouse, monoclonal	IF: 1:50	DSHB (CH1)
Anti-vinculin	mouse, monoclonal	WB: 1:25000	Sigma (V9131)

Secondary antibodies	Source	Amount/dilution	Company
Anti-mouse IgG (Alexa Flour 488)	goat, polyclonal	IF: 1:200	Invitrogen (A-11029)
Anti-mouse IgG (HRP)	goat, polyclonal	WB: 1:10000	Sigma (A0168)
Anti-rabbit IgG (Biotin)	donkey, monoclonal	IF: 1:200	Jackson Immuno Research (711-065-152)
Anti-rabbit IgGMA (HRP)	mouse, monoclonal	WB: 1:10000	Sigma (A2074)
Anti-rat IgG (HRP)	rabbit, polyclonal	WB: 1:20000	Sigma (A9542)

IgG/Serum	Source	Amount/dilution	Company
Normal rabbit IgG	rabbit	ChIP: 5 μg	Santa Cruz Biotech (sc-2027)
Rabbit-anti-sheep IgG	rabbit	LUMIER: 1:750	Jackson Immuno Research (313-005-003)
Sheep gamma globulins	sheep	LUMIER: 1:1000	Jackson Immuno Research (013-000-002)
Donkey serum	donkey	IF: 10 % (v/v)	Sigma (D9663)

Other stains	Source	Amount/dilution	Company
DAPI	synthetic	IF: 1:2000	Sigma (D9542)
Phalloidin-Atto 565	Amanita phalloides	IF: 1:100	Sigma (94072)

2.1.4 Buffers and solutions

Transfection

20x HEBS
0.818 g NaCl
2.5 ml 1 M HEPES
0.0133 g Na_2HPO_4
ad 5 ml H_2O

2x HEBS solution
5 ml 20x HEBS
0.5-0.75 ml 1 N NaOH
ad 50 ml H_2O
adjust pH between 7.1 and 7.2

$CaCl_2$/Tris solution
2.22 g $CaCl_2$
1.16 ml 1 M Tris-HCl pH 7.5
0.65 ml 1 N NaOH
ad 10 ml H_2O
adjust pH to 7.6

Glycerol solution
5 ml 2x HEBS
1.5 ml glycerol
3.5 ml H_2O

PAR-CLIP

NP40 lysis buffer	*High salt lysis buffer*
50 mM HEPES-KOH	1 % NP40
150 mM KCl	500 mM NaCl
2 mM EDTA	50 mM Tris pH 7.2
0.5 % (v/v) NP-40	1 mM DTT
0.5 mM DTT	PIC
PIC	

GST-pulldown and Co-IP

Co-IP buffer	*Lysis Buffer for mammalian cells*
20 mM Tris-Hcl pH 7.4	20 mM Tris-HCL pH 7,4
150 nM NaCl	150 mM NaCl
1 mM EDTA	1 mM EDTA
1 % Triton	1 % Triton X
1 mM DTT	Protease inhibitor (Roche)
0.1 mM PMSF	Benzonase (add before use)
1 mM Na_3VO_4	
Protease inhibitor (Roche)	
Phosphatase inhibitor (Roche)	

Tissue embedding

10.5 g tragacanth
4.2 ml glycerol
spatula tip thymol
105 ml H_2O
mix and store at 4 °C over night before use

Yeast 2-hybrid screen

2x NB medium	*2x Agar*
2.68 g Yeast nitrogen base	8 g Bacto agar
ad 200 ml H_2O	ad 200 ml H_2O

-T/HAUL agar	*-L/HAUT agar*
200 ml 2x Agar	200 ml 2x Agar
200 ml 2x NB medium	200 ml 2x NB medium
25 ml Glucose (40 % stock conc.)	25 ml Glucose (40 % stock conc.)
5 ml Histidine (2 g/l stock conc.)	5 ml Histidine (2 g/l stock conc.)
5 ml Uracil (2 g/l stock conc.)	5 ml Uracil (2 g/l stock conc.)
5 ml Leucine (10 g/l stock conc.)	5 ml Tryptophan (10 g/l stock conc.)
7.5 ml Adenine (2 g/l stock conc.)	7.5 ml Adenine (2 g/l stock conc.)
ad 500 ml H_2O	ad 500 ml H_2O

-ATL/HU agar
500 ml 2x NB medium
10 ml Histidine (2 g/l stock conc.)
10 ml Uracil (2 g/l stock conc.)
50 ml Glucose (40 % stock conc.)
ad 1 l H_2O

YPD agar
5 g Yeast extract
10 g Peptone
10 g agar
25 ml Glucose (40 % stock conc.)
7.5 ml Adenine (2 g/l stock conc.)
ad 500 ml H_2O

-T/HAUL medium
200 ml 2x NB medium
25 ml Glucose (40 % stock conc.)
5 ml Histidine (2 g/l stock conc.)
5 ml Uracil (2 g/l stock conc.)
5 ml Leucine (10 g/l stock conc.)
7.5 ml Adenine (2 g/l stock conc.)
ad 400 ml H_2O

LUMIER assay

Carbonate buffer
70 mM $NaHCO_3$
30 mM Na_2CO_3
pH 9.6

TBST II
10 mM Tris-Base pH 7.4
150 mM NaCl
0.05 % Tween-20

HEPES buffer
50 mM HEPES pH 7.4
150 mM NaCl
1 mM EDTA
10 % Glycerine
1 % Triton X-100
Protease inhibitor (Roche)

RIPA buffer
150 mM NaCl
0.25 mM sodium deoxychelate
50 mM Tris pH 7.5
1 % NP-40
1 mM EGTA
Protease inhibitor (Roche)

Luciferase substrate
250 mM glycylglycine
150 mM potassium phosphate buffer
40 mM EGTA
20 mM ATP
10 mM DTT
150 mM $MgSO_4$
1 mM CoA
75 μM Luciferin

Potassium phosphate buffer
9.4 ml 0.5 M K_2HPO_4
0.6 ml 0.5 M KH_2PO_4

2.1.5 Consumables

Amersham Hybond-H+ membrane	GE Healthcare, United Kingdom
DNA LoBind tubes 1.5 ml	Eppendorf, Germany
Immobilion-P^{SQ} Membrane	Merck Millipore, Germany
Microplate, 96 well, ps, F-bottom (Catalog no 655074)	Greiner Bio-One, Austria
Phase Lock Gel Heavy 1.5 ml	5 Prime, Germany
Precellys Keramik Kit 2.8 mm	Peqlab Biotechnologie, Germany
Protein LoBind tubes 1.5 ml	Eppendorf, Germany

2.2 Vectors

Vector	Size	Resistance	Comment	Reference
pDONR221	4762 bp	Kanamycin	Negative selection (ccdB)	Invitrogen
pBTM116-D9	8276 bp	Tetracycline	Gateway compatible, N-terminal LexA domain	Goehler et al. 2004
pBTMcC24-DM	10871 bp	Tetracycline	Gateway compatible, C-terminal LexA domain	Stelzl laboratory
pGEX-3X	4952bp	Ampicillin	N-terminal GST tag	GE Healthcare Life Sciences, Novagen
pTL-FlagC	4168 bp	Ampicillin	based on pSG5 vector (Stratagene), N-terminal Flag tag	Krobitsch laboratory
pTL-HA1	4.1 kb	Ampicillin	based on pSG5 vector (Stratagene), N-terminal HA tag	Wanker laboratory
pcDNA3.1V5-Fire-DM	8828 bp	Ampicillin	Gateway compatible	Stelzl laboratory
pcDNA3.1PA-D57	7646 bp	Ampicillin	Gateway compatible	Stelzl laboratory

2.3 Oligonucleotides

2.3.1 siRNAs

Company	Name	Target	Accession	Target Sequence
Qiagen	Mm_Dpf3_3	Dpf3a	NM_058212	5'-CTGACTCTGGTCATTGTTCTA-3'
Qiagen	Mm_Dpf3_1	Dpf3a/b	NM_058212	5'-CGGGACAGTCATTCCTAATAA-3'
Qiagen	siDpf3-2-3	Dpf3b	AK039011.1	5'-CGAAATGATCTCATTTAAATT-3'
Qiagen	siDpf3-2-4	Dpf3b	AK039011.1	5'-GAATAGTTACAGAAGGGAATT-3'

2.3.2 Primers

Human primers for cloning

Gene	Name	Sequence	Accession
DPF3	kb108_hDPF3_attB1_start_aa2_f	gggg aca agt ttg tac aaa aaa gca ggc ttc aga acc atg gcgactgtcattcacaaccc	AY803021.1
DPF3	kb109_hDPF3_attB1_ATG_aa198_f	gggg aca agt ttg tac aaa aaa gca ggc ttc aga acc atg tacgtctgtgacatctgtgg	AY803021.1
DPF3	kb110_hDPF3_attB1_ATG_aa259_f	gggg aca agt ttg tac aaa aaa gca ggc ttc aga acc atg aataactactgtgacttctg	AY803021.1
DPF3	kb111_hDPF3_attB2_aa88_r	gggg ac cac ttt gta caa gaa agc tgg gtc tgggtgcaatcgtctcttct	AY803021.1
DPF3	kb112_hDPF3_attB2_aa199_r	gggg ac cac ttt gta caa gaa agc tgg gtc gacgtaaggtttgtcgtggtc	AY803021.1
DPF3	kb113_hDPF3_attB2_aa224_r	gggg ac cac ttt gta caa gaa agc tgg gtc gctggccaggtgagtgtgag	AY803021.1
DPF3	kb114_hDPF3_attB2_aa261_r	gggg ac cac ttt gta caa gaa agc tgg gtc gtagttattgggaatgactg	AY803021.1
DPF3	kb115_hDPF3_attB2_aa378_r	gggg ac cac ttt gta caa gaa agc tgg gtc ggcctggcagccaaaggctg	AY803021.1
DPF3	kb116_hDPF3_attB2_aa356_r	gggg ac cac ttt gta caa gaa agc tgg gtc gcaactgccctttttatctg	NM_012074.4
DPF3	kb117_hDPF3_attB1_aa12_f	gggg aca agt ttg tac aaa aaa gca ggc ttc aga acc atg ctcggggaccagttctacaag	NM_012074.4
DPF3	kb118_hDPF3_attB1_aa170_f	gggg aca agt ttg tac aaa aaa gca ggc ttc aga acc atg aacaggactagaggacgggct	NM_012074.4

Mouse primers for genotyping

Gene	Name	Sequence	Accession
Cre	hc07_jacksonlab_cre_f	gcggtctggcagtaaaaactatc	-
Cre	hc08_jacksonlab_cre_r	gtgaaacagcattgctgtcactt	-
Dpf3	js233-lox1-frd	ctccatgggacatctctgctcg	AK039011
Dpf3	js234-sdl1-rev	ccagaagagctgcatttatggc	AK039011
Dpf3	js235-a2-frd	gtgactttgaggcacagtggcttg	AK039011
Dpf3	js236-f3-rev	gcataagcttggatccgttcttcggac	AK039011
Dpf3	js237-long1-frd	ggaccagacaaagatgatgtgagg	AK039011
Dpf3	js238-pb4-rev	gatggctcggtcagcaatgtg	AK039011
Dpf3	kb090_loxpcre_f	catctctgctcgtgtagtcttt	AK039011
Dpf3	kb091_loxpcre_r	ctcacccacagctaaacaca	AK039011

Mouse primers for cloning

Gene	Name	Sequence	Accession
Luc7l2	kb_068_Luc7l2_m_xaa2_BamHI_f	catg ggatcc a tcggcgcaggcccagatgcg	NM_138680.2
Luc7l2	kb_069_Luc7l2_m_NotI_r	catg gcggccgc ttagatctcccctgcttcac	NM_138680.2
Luc7l2	kb_070_Luc7l2_m_xxaa2_BamHI_f	catg ggatcc at tcggcgcaggcccagatgcg	NM_138680.2
Luc7l2	kb_071_Luc7l2_m_EcoRI_r	catg gaattc ttagatctcccctgcttcac	NM_138680.2
Luc7l2	kb100_EcoRI_Luc7l2_x_f	cgtac gaattc a tcggcgcaggcccagatg	NM_138680.2

Mouse primers for qPCR

Gene	Name	Sequence	Accession
-	all_mr6_f1	cagcgatctgcttacggaatta	AL606962
-	all_mr6_r1	cacgtgcgaaaggcaattag	AL606962
Acta1	acta1_rt_m_f	ttgtgtgtgacaacggctctg	NM_009606
Acta1	acta1_rt_m_r	acccacgtaggagtccttctga	NM_009606
Acta2	acta2_rt_m_f	cctggcttcgctgtctacct	NM_007392
Acta2	acta2_rt_m_r	ttgcggtggacgatgga	NM_007392
Actc1	mactc1_exp_f1	tatgccttaccccatgccat	NM_009608.3
Actc1	mactc1_exp_r1	tcacgttcagcagtggtgaca	NM_009608.3
Cdh8	no_mr1_f1	aggttccagagataggaaccca	AC162867
Cdh8	no_mr1_r1	ggccaccatctgatttagca	AC162867
Csrp3	csrp3_rt_m_f	gcctgtgaaaagacggtctacc	NM_013808
Csrp3	csrp3_rt_m_r	gccatgcagtggaaacaggt	NM_013808
Dnmt1	kb_041_h3k4me1_pos_dnmt1_f	attctactgggcttgtctgc	NM_010066
Dnmt1	kb_042_h3k4me1_pos_dnmt1_r	tccttctagtctttctcccctg	NM_010066
Dpf1	mdpf1_rt_ex9-10_f	agccaagaaagcaccagatg	AK142419
Dpf1	mdpf1_rt_ex9-10_r	actgtaaacacgagggatgtc	AK142419
Dpf2	mdpf2_rt_ex4-5-6_f	ctgggcgagtttcctgttag	AK144954
Dpf2	mdpf2_rt_ex4-5-6_r	ctgctcacaccttactcttg	AK144954
Dpf3	mdpf3_rt_ex2-3_f	acaactgctacatctggatgg	NM_058212
Dpf3	mdpf3_rt_ex2-3_r	gtcgtagttttgggtcctctg	NM_058212
Dpf3a	h1_m_cg_f9	cagacgggacagtcattcctaat	AF362750
Dpf3a	h1_m_cg_r9	ctcccaaatgagcagagcgt	AF362750
Dpf3b	h1_m_r9_f2	cctcatttctaccagcggga	AK039011
Dpf3b	h1_m_r9_r2	gcaacacacgagtggttgatg	AK039011
Gli2	no_mr5_f1	gcacccaggcattttctttca	AC122287

Gli2	no_mr5_r1	tgtgtgtcagttcggagctgag	AC122287
Hprt	hprt_m_f	aaacaatgcaaactttgctttcc	NM_013556
Hprt	hprt_m_r	ggtccttttcaccagcaagct	NM_013556
Igf1	migf1_exp_f1	ttcagttcgtgtgtggaccga	NM_010512
Igf1	migf1_exp_r1	atccacaatgcctgtctgagg	NM_010512
Mdh2	kb_043_h3k4me1_pos_mdh2_f	gaatcagtaaaggagacccagg	NM_008617
Mdh2	kb_044_h3k4me1_pos_mdh2_r	ccggagcatggtaattgtttc	NM_008617
Mid1lp1	mid1ip1_f1	gggatttcgcagtgcaagag	NM_026524
Mid1lp1	mid1ip1_r1	tctcagctcagcccttcgt	NM_026524
Myh7	myh7_m_f1	cagaacaccagcctcatcaacc	NM_080728
Myh7	myh7_m_r1	tcatggcggcatctgtgatag	NM_080728
Notch3	notch3_rt_m_f	tggacaggccagttctgtaca	NM_008716
Notch3	notch3_rt_m_r	tccagccattgacacatacaca	NM_008716
Nppa	manf_rt_f	ctg atg gat ttc aag aac ctg ct	NM_008725
Nppa	manf_rt_r	cct gct tcc tca gtc tgc tca	NM_008725
Phf10	kb106_mPhf10_ex7-8_f	tccaagtgcctcaaggaaag	ENSMUST00000024657
Phf10	kb107_mPhf10_ex7-8_r	gctcatacagggctgtgttta	ENSMUST00000024657
Plekhb2	plekhb2_m_f1	acccctgaggtctacggctat	ENSMUST00000027297
Plekhb2	plekhb2_m_r1	tggttggcaggctgttgtc	ENSMUST00000027297
Rp113a	all_mr9_f1	agctaaatcccgtctcaggcat	AC126256
Rp113a	all_mr9_r1	agttccggagaccctccagtaa	AC126256
Syt6	no_mr7_f1	gctgctaaaggcagaaatgtgg	AC123057
Syt6	no_mr7_r1	aatggaaaaggcgctctgg	AC123057
Tfrc	tfrc_m_f1	catggtgaccatagtgcagtca	ENSMUST00000023486
Tfrc	tfrc_m_r1	agcatggaccagtttaccagaa	ENSMUST00000023486
Tm4sf1	tm4sf1-exp-f.1	tacgaaaactacggcaagcg	ENSMUST00000029376
Tm4sf1	tm4sf1-exp-r.1	cacagtaagcagatcccacgat	ENSMUST00000029376
Tpm2	mtpm2_exp_f1	ctgaagaccgatgcaagca	NM_009416
Tpm2	mtpm2_exp_r1	ttttccacctcgtcctctgtc	NM_009416

2.4 Devices

2100 Bioanalyzer Instrument	Agilent Technologies, USA
ABI PRISM 7900HT Fast Real-Time PCR System	Applied Biosystems, USA

Axio Imager.M2	Zeiss, Germany
Biomek NX	Beckman Coulter, USA
Bioruptor® UCD-300	Diagenode, Belgium
Branson Digital Sonifier 450	Branson Ultrasonics, USA
ChemiDoc™ MP Imaging System	Bio-Rad Laboratories, USA
DTX880 Multimode microplate reader	Beckman Coulter, USA
Eppendorf Centrifuge 5804 R	Eppendorf, Germany
Eppendorf Centrifuge 5810 R	Eppendorf, Germany
Eppendorf Thermomixer comfort	Eppendorf, Germany
FastPrep®-24 instrument	MP Biomedicals, USA
Fujifilm FLA-7000	Fujifilm, Japan
Himac CT 15RE	Hitachi, Japan
HiSeq 2000	Illumina, USA
Kby roboter	Kbiosystems, United Kingdom
Leica CM3050 S	Leica Microsystems CMS, Germany
Leica KL1500 LCD	Leica Microsystems CMS, Germany
Leica MZ75	Leica Microsystems CMS, Germany
Leica TCS SPE	Leica Microsystems CMS, Germany
LightCycler® 480 II	Roche Diagnostics, Switzerland
LUMIstar Omega	BMG Labtech, Germany
Microm HM 340E	Thermo Fisher Scientific, USA
Motic B3 Professional Series 220 ASC	Motic, China
NanoDrop 2000c spectrophotometer	Thermo Fisher Scientific, USA
New Brunswick™ Innova® 44 Incubator Shaker	Eppendorf, Germany
PR 648 Slot Blot Filtration Manifold	Amersham biosciences,United Kingdom
PRC-225 Peltier Thermal Cycler	MJ Research, USA
Qubit® 2.0 Fluorometer	Thermo Fisher Scientific, USA
Safe Imager™ 2.0 Blue Light Transilluminator	Thermo Fisher Scientific, USA
Stratalinker® UV crosslinker 2400	Stratagene, USA

2.5 Software

Axio Vision (release 4.8.2.0)	Zeiss, Germany
Gentle (V1.9.4)	Magnus Manske, University of Cologne, GPL 2003, Germany
ImageJ (version 1.50e)	Wayne Rasband, National Institutes of Health, USA
Image Lab (version 5.0 build 18)	Bio-Rad Laboratories, USA
Integrative Genomics Viewer (IGV) (version 2.3.67 (96))	The Broad Institute, USA
LAS AF (version 2.632)	Leica Microsystems CMS, Germany

LAS AF Lite (version 2.6.3 build 8173)	Leica Microsystems CMS, Germany
LightCycler® 480 Software (release 1.5.0 SP4)	Roche Diagnostics, Switzerland
Multi Gauge (version 3.2)	Fujifilm, Japan
SDS (version 2.2.1)	Applied Biosystems, USA
QtiPlot (version 0.9.8.9 svn 2288)	Ion Vasilief

2.6 Kits

Agilent High Sensitivity DNA Kit	Agilent Technologies, USA
Agilent RNA 6000 Nano Kit	Agilent Technologies, USA
ChIP DNA Clean & Concentrator™	Zymo research, Germany
DNA-free™ DNA Removal Kit	Thermo Fisher Scientific, USA
DyNAmo Flash SYBR Green qPCR Kit	Thermo Fisher Scientific, USA
GoTaq® Probe qPCR Master Mix	Promega, USA
HiSpeed Plasmid Maxi Kit	Qiagen, Germany, The Netherlands
MAGnify™ Chromatin Immunoprecipitation System	Thermo Fisher Scientific, USA
NEXTflex™ Illumina ChIP-Seq Library Prep Kit	Bioo Scientific, USA
peqGOLD Plasmid Miniprep Kit I	Peqlab Biotechnologie, Germany
Plasmid Midi Kit	Qiagen, Germany, The Netherlands
QIAquick Gel Extraction Kit	Qiagen, Germany, The Netherlands
Qubit® dsDNA HS Assay Kit	Thermo Fisher Scientific, USA
Qubit® RNA BR Assay Kit	Thermo Fisher Scientific, USA
Qubit® RNA HS Assay Kit	Thermo Fisher Scientific, USA
ScriptSeq v2 RNA-Seq Library Preparation Kit	Illumina, USA
TruSeq PE Cluster Kit v3-cBot-HS	Illumina, USA
TruSeq SBS Kit v3-HS	Illumina, USA
TruSeq Small RNA Library Preparation Kit	Illumina, USA
TruSeq SR Cluster Kit v3-cBot-HS	Illumina, USA
TSA Plus Cyanine 5 System	Perkin Elmer, USA
Vectastain® Elite ABC Kit (Standard)	Vector Laboratories, USA
Wizard® SV Gel and PCR Clean-up System	Promega, USA
Bright-Glo Luciferase Assay System	Promega, USA

2.7 Mammalian cell cultures and microorganisms

2.7.1 HL-1 mouse cardiomyocytes

HL-1 cells were obtained from Prof. William C. Claycomb (Departments of Biochemistry and Molecular Biology and Cell Biology and Anatomy, Louisiana State University Medical Center, New Orleans) and cultured as described in Claycomb et al. (1998).

2.7.2 C2C12 mouse skeletal muscle cells

C2C12 mouse myoblast cells were provided by Prof. Jakob Schmidt (Department of Biochemistry and Cell Biology, State University of New York, Stony Brook, New York) and cultivated at 5 % CO_2 and 37 °C in Dulbecco's modified Eagle's medium supplemented with 10 % fetal bovine serum and 1 % Penicillin/Streptomycin.

2.7.3 Human embryonic kidney cells

HEK293T human kidney cells were cultivated at 5 % CO_2 and 37 °C in Dulbecco's modified Eagle's medium supplemented with 10 % fetal bovine serum and 1 % Penicillin/Streptomycin. Cells were subcultured at confluency and split 1:10 for the next passage.

HEK 293 Flp-In^{TM} T-REx^{TM} (ThermoFisher Scientific) were cultured at 5 % CO_2 and 37 °C in Dulbecco's modified Eagle's medium supplemented with 10 % fetal bovine serum. Cells were subcultured at confluency and split 1:10 for the next passage.

2.7.4 *Escherichia coli* strains

Escherichia coli (*E. coli*) cells were grown in LB medium (25 g L-broth/l H2O) in a shaking incubator or on LB agar plates (40 g LB agar/l H2O) for 16-20 h at 37 °C. Liquid or solid cultures were immediately processed or stored at 4 °C for a short time. For long-term storage, liquid *E. coli* cultures were supplemented with 25 % glycerol final concentration and frozen at -80 °C.

E. coli DH10B (F^- mcrA Δ(mrr-hsdRMS-mcrBC) ϕ80dlacZΔM15 ΔlacX74 endA1 recA1 $deoR^+$ Δ(ara,leu)7697 araD139 galE15 galK galU Str^R λ^-)

E. coli DB3.1 (F^- gyrA462 endA1 glnV44 Δ(sr1-recA) mcrB mrr hsdS20(r_B^-, m_B^-) ara14 galK2 lacY1 proA2 rpsL20(Smr) xyl5 Δleu mtl1)

E. coli BL21 DE3 pRARE3 (Novagen)

2.7.5 Yeast strains

Yeast cultures were grown in liquid medium or on agar plates as described in Worseck et al. (2012).

L40c MATa: MATa his3Δ200 trp1-901 leu 2-3,112 ade2 lys2-801am can1 LYS2::$(lexAop)_4$-HIS3 URA3::$(lexAop)_8$-lacZ

L40ccα MATα: MATα his3Δ200 trp1-910 leu2-3,112 ade2 GAL4 can1 cyh2 LYS2::$(lexAop)_4$-HIS3 URA3::$(lexAop)_8$-lacZ (Goehler et al. 2004)

2.8 Standard molecular biology techniques

2.8.1 Transformation of bacteria

Plasmid DNA was introduced into *E. coli* cells by heat shock transformation. 100 μl chemically competent DH10B cells were incubated with 10-100 ng of plasmid DNA or 10 μl ligation mix (see section 2.8.7) for 30 min on ice. After a heat shock at 42 °C for 45 sec, the cells were incubated on ice for 3 min and grown in 1 ml LB medium at 37 °C in a thermomixer at 400 rpm. 200-300 μl were plated on selective LB-agar plates containing the appropriate antibiotic an incubated overnight at 37 °C. Single colonies were grown in LB medium and used for plasmid preparations.

2.8.2 Transformation of *S. cerevisiae*

For the yeast two-hybrid screen, the yeast strain L40c MATa was transformed with destination vectors containing DPF3 sequences (see Table 3.8) as described in (Worseck et al. 2012).

2.8.3 Transfection of mammalian cells with expression vectors

PEI transfection

3 x 10^6 HEK293T cells per p150 cm plate were seeded and grown in supplemented DMEM medium. After 48 h, the medium was changed and the cells were transfected additional three hours later. For this, 30 μg plasmid DNA and 90 μl PEI (1 mg/ml) were diluted in 1.5 ml serum-free medium each. The PEI solution was carefully mixed with the DNA

solution and added dropwise to the cells after 15 min incubation at room temperature. The cells were gently washed with Dulbecco's PBS after 24 h and harvested after 48 h.

$CaCl_2$ transfection

62 μl $CaCl_2$/Tris solution and 20 μg plasmid DNA were diluted in purified water ad 1 ml final volume. The mix was added dropwise and slowly to 1 ml 2x HEBS solution under constant bubbling with a second pipette and incubated for 30 min at room temperature. In the meantime, C2C12 cells were seeded to 15 % confluency in a p150 dish. The transfection mix was gently pipetted up and down and added dropwise to the cells. After 24 h, the cells were washed twice with Dulbecco's PBS and incubated with 2 ml glycerol solution for exactly 2 min at room temperature. The glycerol shock was stopped with 8 ml DMEM medium. The cells were washed with Dulbecco's PBS and grown in supplemented DMEM medium for additional 24 h before harvesting.

2.8.4 siRNA knockdown in mammalian cells

HL-1 cells were grown to $\sim$ 90 % confluency within two days in supplemented medium without Penicillin and Streptomycin. 400 000 cells per well were seeded in a coated 6-well plate and cultivated overnight. Prior to transfection, the medium without antibiotics was changed. 15 μl lipofectamine 2000 were diluted in 470 μl DMEM medium without supplements and incubated for 5 min at room temperature. Meanwhile, 4,4 μl Mm_Dpf3_1, 4,4 μl Mm_Dpf3_3, 2,2 μl siDpf3-2-3 and 2,2 μl siDpf3-2-4 from 20 μM stock solutions were mixed and diluted in 270 μl DMEM medium. The siRNA mix was added to the lipofectamine mix, incubated for 20 min at room temperature and carefully droped on the cells. AllStars negative Control siRNA (20 μM, Qiagen) was prepared accordingly as negative control. The medium was changed after 24 h and the cells were harvested after 48 h.

2.8.5 Polymerase chain reaction

Polymerase chain reactions (PCR) were performed on 10 ng plasmid DNA, 100-150 ng genomic DNA or 100 ng purified cDNA using forward and reverse primers (0.5 μM final concentration of each primer) and the Phusion High-Fidelity PCR Master Mix with HF Buffer (New England Biolabs). After an initial denaturation (2 min at 98 °C), the following steps were repeated 34 times: 10 sec denaturation, 20 sec annealing at a temperature suitable for the melting temperature of the primer pair, 20 sec/kb elongation. After a final elongation period of 10 min at 72 °C, the reaction was cooled to 4 °C.

Genotyping of mice was performed by PCRs using the Phire Animal Tissue Direct PCR Kit (Thermo Fisher Scientific) according to the manufacturer's instructions.

Quantitative PCRs were performed in 10 μl reaction volumes on the ABI PRISM 7900HT system (Applied Biosystems) or LightCycler 480 II (Roche). cDNA (see section 2.8.6) or ChIP DNA (see section 2.11.3) solutions were diluted 1:5 and 1:10, respectively. 2 μl template DNA and 0.5 μM (final concentration) forward and 0.5 μM (final concentration) reverse primer were mixed with the GoTaq Probe qPCR Master Mix (Promega) for amplifications at the ABI PRISM 7900HT system or with the DyNamo Flash SYBR Green qPCR mix (Thermo Fisher Scientific) for amplifications at the LightCycler 480 II. Temperature profiles and dissociation curves were set according to standard conditions described in the manuals from Promega and Thermo Fisher Scientific. Primer efficiencies and Ct values were calculated with the respective analysis softwares at default settings.

2.8.6 Reverse transcription

0.5 μg to 1 μg of total RNA was reversely transcribed to cDNA using the AMV-Reverse Transcriptase (Promega) as described in the manual.

2.8.7 Cloning

The sequence of interest was amplified from cDNA with primers carrying suitable restriction sites (see sections 2.8.6 and 2.3.2). The PCR products were purified using Agencourt AMPure XP beads (Beckman Coulter) according to the manufacturer's instructions and digested as described in section 2.8.8. After clean up with the Wizard SV Gel and PCR Clean up System (Promega), the PCR products were ligated with 50 ng already prepared vector (see sections 2.8.8 and 2.2) in a vector to insert ratio of 1:3. The required amount of PCR product was calculated as follows:

$$ng\ (insert) = \frac{3\ *\ 50ng\ *\ bp\ (insert)}{bp\ (vector)}$$

The reaction mix was prepared using 400 U T4 DNA ligase (New England Biolabs) in a total reaction volume of 20 μl 1x T4 DNA ligase reaction buffer (New England Biolabs). After 2 h at room temperature, 10 μl were introduced into *E. coli* DH10B as described in section 2.8.1.

The vectors were isolated from *E. coli* cultures, which had been grown from single colonies, using the peqGOLD Plasmid Miniprep Kit I (Peqlab) according to the manufacturer's in-

structions. The insertion of the PCR product was evaluated by restriction digestion (see section 2.8.8) and Sanger sequencing.

Gateway cloning

The Gateway cloning system is based on site-specific recombination reactions of bacteriophage λ in *E. coli*. PCR products flanked by attB recombination sites were introduced into the pDONR221 vector (see section 2.2) by an *in vitro* BP reaction and the vector was amplified in *E. coli* DH10B (see section 2.8.1). Subsequent *in vitro* recombination via an LR reaction shuttles the sequence of interest from the purified entry vectors into destination vectors (see section 2.2). For positive selection, *E. coli* DH10B cells were transformed with the LR reaction and purified in a 96-well Mini-Prep as described in (Worseck et al. 2012). The entry as well as the destination vectors carry the ccdB cassette before recombination. As the ccdB gene product is lethal in *E. coli* DH10B, only *E. coli* DH10B transformed with successfully recombined vectors will grow on selective agar plates. For propagation of entry and destination vectors with a ccdB cassette, the *E. coli* strain DB3.1 was used. Both BP and LR reactions were performed as described in the Gateway Cloning manual from Invitrogen and the recombinations were monitored by enzymatic digestion and Sanger sequencing.

2.8.8 Restriction digestion

Vectors and PCR products were enzymatically digested during the cloning procedure as described in section 2.8.6. 45 μl PCR reaction or 1 μg vector were incubated with 10 units of the desired restriction enzyme (New England Biolabs) for one hour at 37 $°C$ in a total volume of 50 μl of the recommended 1x NEbuffer (New England Biolabs), supplemented wit 1x BSA (New England Biolabs) final concentration if required. The reaction was scaled down for the evaluation after ligation (see section 2.8.7).

If the vector was prepared for ligation, a dephosphorylation with 5 U (final concentration) Antarctic Phosphatase (New England Biolabs) in 56 μl 1x phosphatase buffer followed. Otherwise, the restriction digestion was assessed by gel electrophoresis (see section 2.8.12).

Gateway cloning was evaluated using 0.1 U FastDigest Bsp1407I enzyme (Fermentas) in a total volume of 20 μl FastDigest Green Buffer (Fermentas). After 30 min at 37 °C and heat inactivation at 65 °C, the restriction digestion was assessed by gel electrophoresis (see section 2.8.12).

2.8.9 Isolation of DNA

Genomic DNA from murine tail or ear biopsies was isolated with the Phire Animal Tissue Direct PCR Kit (Thermo Fisher Scientific) according to the manufacturer's instructions.

Plasmid DNA was isolated from *E. coli* cells using the peqGOLD Plasmid Miniprep Kit I (Peqlab), the Plasmid Midi Kit (Qiagen) or the HiSpeed Plasmid Maxi Kit (Qiagen) according to the protocols in the respective manuals.

2.8.10 Isolation of RNA

RNA was isolated from adherent cells using the TRIzol reagent (Thermo Fisher Scientific) according to the manufacturer's instructions. RNA from tissue samples was isolated using the TRIzol reagent (Thermo Fisher Scientific) and homogenization with the Precellys Keramik Kit 2.8 mm (Peqlab Biotechnologie) at the FastPrep-24 device according to the manufacturer's instructions. DNA was removed with the DNA-free DNA Removal Kit (Thermo Fisher Scientific) as described in the manual.

2.8.11 Nucleic acid precipitation

Nucleic acids were precipitated by adding 2.5 volumes of 100 % ethanol, 1/10 volume 3 M sodium acetate and 1 μl GlycoBlue (15 mg/ml stock concentration, Thermo Fisher Scientific) or 1 μl glycogen (20 mg/ml stock concentration). After an incubation time ranging from at least one hour to overnight at -20 °C, the DNA or RNA samples were centrifuged for 30 min at full speed (13000-20000 g). Alternatively, RNA was precipitated by adding one volume of isopropanol instead of ethanol, the incubation time was reduced to 30 min at room temperature and the centrifugation performed as described above. In both cases, the pellets were washed with 750 μl of 70 % ethanol and again centrifuged at full speed for 10 min. The pellets were allowed to dry at room temperature and resuspended in an appropriate volume of purified water or TE-buffer.

2.8.12 Visualization of nucleic acids and proteins

Nucleid acids were visualized by gel electrophoresis using 1 % or 2 % agarose gels. Samples were stained with GelRed (Biotium) or Midori Green Direct (Nippon Genetics) according to the respective manuals. Appropriate DNA ladders were loaded for size estimation. Nucleic acids were detected with the ChemiDoc MP Imaging System.

Proteins were visualized by Western blotting. Protein lysates were separated in 10 % SDS gels and blotted on PVDF membranes by semi-dry blotting. The Spectra Multicolor Broad Range Protein Ladder (Thermo Fisher Scientific) was loaded for size estimation. The membranes were blocked in 5 % skim milk powder/PBS and incubated with the primary antibody for 1 h at room temperature or at 4 °C overnight. After a minimum of three washes in PBS, the membrane was icubated with the secondary antibody for 1 h at room temperature. The antibodies were dissolved in 5 % skim milk powder/PBS according to the table in section 2.1.3. The membrane was again washed in PBS and incubated with Super Signal West Pico Chemiluminescent Substrate (Thermo Fisher Scientific) according to the manufacturer's instructions. If the signal was weak, the Pico Chemiluminescent Substrate was supplemented with 10 % Super Signal West Femto Chemiluminescent Substrate (Thermo Fisher Scientific). Protein bands were recorded with the ChemiDoc MP Imaging System.

2.9 Characterization of mouse strains

2.9.1 Animals

C57BL6/J, *Dpf3*^{tm1Sper}, *Dpf3*$^{tm1.1Sper}$ and B6.C-Tg(CMV-cre)1Cgn/J mice were housed in the IVC system with Blue Line (536 cm^2) and Green Line (501 cm^2) cages at constant temperature (22 ± 2 °C) and humidity (55 ± 15 %) with a fixed 12 h light/dark cycle. The cages were enriched with nesting material. Standard food and water were provided *ad libitum*. Hygiene was monitored according to the FELASA recommendations for the health monitoring of rodents.

2.9.2 Genotyping

Genomic DNA from tail or ear biopsies was isolated with the Phire Animal Tissue Direct PCR Kit (Thermo Fisher Scientific) according to the manufacturer's instructions and subjected to analysis by PCR as described in section 2.8.5. Primers are listed in section 2.3.2.

2.9.3 Dissection of mice

Mice were sacrificed by cervical dislocation and the body weight as well as the weights of selected organs were determined. Dissected hearts were washed in PBS, fixed in 4 % PFA, embedded in paraffin and stored at room temperature. Skeletal muscles were dissected,

embedded in tragacanth, briefly frozen in 2-methylbutane cooled over liquid nitrogen and then transferred to liquid nitrogen. The specimen were stored at -80 °C.

2.9.4 Histology

Prior to stainings, 5 μm paraffin sections were rehydrated. Rehydrated paraffin sections and 6μm cryo sections were stained in hematoxylin (2 min), washed in tap water and purified water, stained in eosin (30 sec) and washed again. The intensity of the eosin staining was adjusted with 96 % ethanol. After dehydration in absolute ethanol, eukalyptol and xylenes, the slides were mounted with Entellan (Merck Millipore) and analyzed at an Axio Imager.M2 microscope (Zeiss).

For the immunofluorescence analysis of sarcomeric proteins, cryo sections (6μm) were blocked with 10 % donkey serum and 2 % BSA in 0.3 % PBS-Tween and primary antibodies were applied overnight at 4 °C in the same solution. After three washes with PBS, appropriate secondary antibodies were diluted in the same solution and incubated for 1 h at room temperature. The nuclei were counterstained with DAPI and the slides were mounted with Fluoromount (Sigma). Images were captured at a Leica SPE confocal microscope. The antibodies and their respective dilutions are listed in section 2.1.3.

For the immunofluorescence analysis of Dpf3, heat-induced antigen retrieval was performed for 15 min in boiling 10 mM citric acid (pH 6) on PFA-fixed (2 %) cryo sections (6μm). After permeabilization with 0.3 % Triton X-100/PBS (2x 10 min), the slides were briefly washed in PBS and the endogenous peroxidase activity was quenched by applying 6 % hydrogen peroxide solution for 30 min. Blocking and incubation with the primary anti-pDpf3a and the secondary anti-rabbit-Biotin antibody was performed as described above. The nuclei were counterstained with DAPI. Meanwhile, Reagent A and Reagent B from the Vectastain Elite ABC Kit Standard (Vector Laboratories) were diluted 1:100 in PBS and allowed to form complexes of modified avidin and biotinylated peroxidase H with enhanced enzyme activity. After 1 h, the slides were incubated for 1 h with the ABC solution. The fluorescence signal was developed with the TSA Plus Cyanine 5 System Kit (Perkin Elmer) in 3 min using the TSA Cyanine 5 reagent in an 1:100 dilution. The slides were mounted with Fluoromount (Sigma). Images were captured at a Leica SPE confocal microscope. The antibodies and their respective dilutions are listed in section 2.1.3.

2.10 Protein-protein interaction assays

2.10.1 GST-pulldown

GST fusion proteins (see section 2.2) were expressed in *E. coli* BL21 DE3 pRARE3 and coupled to the Glutathione–Sepharose matrix (GE Healthcare) according to the manufacturer's instructions. Recombinant Flag-tagged proteins (see section 2.2) were expressed in HEK293T cells and harvested with Lysis Buffer for mammalian cells (see sections 2.8.3 and 2.1.4) by incubation for 30 min at 4 °C and subsequent centrifugation at 18000 g for 15 min at 4 °C. Protein lysates containing 500 μg Flag-tagged protein were incubated with 250 μl loaded Glutathione–Sepharose matrices and incubated for 2 h at 4 °C in a total volume of 500 μl Co-IP buffer (see section 2.1.4). The matrices were washed three times in Co-IP buffer, resuspended in LDS sample buffer, denatured at 95 °C for 5 min and subjected to Western blot analysis (see section 2.8.12).

2.10.2 Co-immunoprecipitation

Flag- and HA-tagged proteins (see section 2.2) were co-expressed in HEK293T cells (see section 2.8.3) and harvested with Co-IP buffer (see section 2.1.4). A total of 500 μg cell extract were incubated with the Flag M2 matrix (Sigma) or HA-matrix (Roche) for 2 h at 4 °C according to the manufacturer's instructions. The matrices were washed three times with ice-cold Co-IP buffer and eluted with LDS sample buffer for Western blot analysis (see section 2.8.12).

2.10.3 Yeast-2-hybrid screen

Four full lenth and nine truncation constructs of DPF3 isoforms (see Table 3.8 in chapter 3.3.3) were cloned into pBTM116-D9 and pBTMcC24-DM (see section 2.2) via Gateway cloning as described in section 2.8.7. In addition, three constructs from a former Yeast-2-hybrid (Y2H) screen (see chapter 3.3.1) were included in the experiment. The L40c MATa yeast strain was transformed with these bait vectors according to the protocol in Worseck et al. (2012).

The prey matrix had been stored at -80 °C. For reactivation of yeast growth, the matrix was thawed and stamped on -L/HAUT agar plates. After two days at 30 °C, the prey matrix was replicated on 12 -L/HAUT agar plates and again incubated for two days at 30 °C. One day before mating, the baits were picked and grown in liquid -T/HAUL medium at 30 °C overnight. For matings, the baits were filled into 384 well plates. The prey matrix was

stamped solid-liquid-solid on YPD agar plates, using the bait cultures as liquids. After two days at 30 °C, the bait-prey pairs were stamped on selective agar plates (-ATL/HU) and incubated at 30 °C. Pictures for the analysis of colony growth were taken four and seven days later. The compositions of media and agars are listed in section 2.1.4.

2.10.4 LUMIER assay

DPF3 constructs in the pDONR221 vector were shuttled into pcDNA3.1V5-Fire and pcDNA-3.1PA-D57 vectors by Gateway cloning as described in section 2.8.7. 30000 HEK 293 Flp-In™ T-REx™ per well were seeded in a 96-well plate, which had been coated with 0.05 mg/ml D-Lysine. After 24 h, the cells were cotransfected with 100 ng/well pcDNA3.1V5-Fire and 50 ng/well pcDNA3.1PA-D57 with the desired inserts (see Table 2.12) using Lipofectamine 2000 (Thermo Fisher Scientific) according to the manufacturer's instructions. Each transfection was performed in triplicates. The cells were briefly washed with PBS and lysed in 100 μl HEPES-buffer per well 36 h after transfection.

For the co-immunoprecipitation, a microplate (96 well, ps, F-bottom from Greiner Bio-One) was coated with sheep gamma globuline (1:1000 in carbonate buffer), blocked with 1 % BSA/carbonate buffer, washed three times with TBST II, incubated with rabbit-anti-sheep IgG (1:750 in carbonate buffer) and washed again with TBST II. All incubation steps were at 4 °C overnight on a shaker.

The cell lysates were cleared by centrifugation. Meanwhile, a second white 96-well plate was filled with 40 μl PBS and 40 μl self-made luciferase substrate. 5 μl of cell lysate per well was added and the firefly input signal was recorded to assess if the transfection was successful. The PA-fusion constructs were precipitated in the coated 96-well plate by adding 75 μl cell lysate and incubation for 2 h at 4 °C on a shaker. After three wahes with ice-cold PBS, 40 μl PBS and 40 μl Bright-Glo substrate (Promega) per well were added and the luciferase activity measured after 5 min and 10 min. Log 2-fold change binding for the protein pair was calculated from the relative luciferase intensities in comparison to background binding measured in parallel with the firefly-tagged and nonrelated PA-fusion proteins (see Table 2.12, negative controls). Ratios larger than two and a z-score larger than two were considered positive. 20 μl cell lysate were subjected to Western blot analysis (see section 2.8.12) to evaluate the expression of the PA-fusion proteins.

Table 2.12: Protein-protein interactions tested by LUMIER assays.

Type	FIRE-tagged protein		PA-tagged protein
Asssay	SR140 (AKHAb12i23a) SR140 (CCSB_53106) IK (AKHAMPS15b04) IK (CCSB_14974) LUC7L (CCSB_3678) RBM39 (IOH52195) RBM39 (IOH41717)	X	DPF3a DPF3b DPF3a_aa12-357 DPF3a_aa170-357 C2H2 C2H2_L C2H2_halfPHD C2H2_tandemPHD
Neg. control	SR140 (AKHAb12i23a) SR140 (CCSB_53106) IK (AKHAMPS15b04) IK (CCSB_14974) LUC7L (CCSB_3678) RBM39 (IOH52195) RBM39 (IOH41717)	X	GPKOW APPL2 SPATA24 QKI BAT3 U2AF1
Pos. control	hPRP2/DHX16 (CCSB_4899)	X	GPKOW (CCSB_4001)
Asssay	DPF3a_aa12-357 C2H2_L C2H2_tandemPHD	X	SR140 (AKHAb12i23a) IK (AKHAMPS15b04) LUC7L (CCSB_3678) RBM39 (IOH52195)
Neg. control	DPF3a_aa12-357 C2H2_L C2H2_tandemPHD	X	GPKOW PPARA APPL2
Pos. control	SMU1 (RZPDo839F0177) RBM10 (CCSB_4573) LUC7L (CCSB_3678)	X X X	IK (AKHAMPS15b04) SR140 (AKHAb12i23a) LUC7L (CCSB_3678)

Each FIRE-tagged fusion construct listed in a box in the middle column was tested against each PA-tagged fusion construct listed in the respective box in the right column in technical triplicates. Each assay setup including the negative and positive controls was performed at least twice.

2.11 Next-generation sequencing based methods

2.11.1 Whole-transcriptome analysis

Total RNA was isolated as described in section 2.8.10 and purified with Dynabeads Oligo(dT)$_{25}$ (Thermo Fisher Scientific). After poly(A) purification, the RNA was assessed with the Qubit RNA HS Assay Kit (Thermo Fisher Scientific) and the Agilent RNA 6000 Nano Kit (Agilent Technologies). The RNA libraries were prepared with the ScriptSeq v2 RNA-Seq Library Preparation Kit (Illumina) using primers with P5 and P7 adapters and individual 6 bp long indices for each sample. The libraries were evaluated with the Qubit dsDNA HS Assay Kit (Thermo Fisher Scientific) and the Agilent High Sensitivity DNA Kit (Agilent Technologies). For sequencing, nine samples were pooled and split on three sequencing lanes. Paired-end sequencing was performed on a Illumina HiSeq 2000 device (Illumina) using the TruSeq PE Cluster Kit v3-cBot-HS (Illumina) and the HiSeq Sequencing Kit (Illumina). All kits were applied according to the manufacturer's instructions.

For the analysis of differential gene expression, the reads were mapped to the mouse reference genome (mm9) using TopHat (version 2.0.8) (D. Kim et al. 2013). Transcript assembly and calculation of FPKM values (fragments per kilobase of transcript per million fragments mapped) were conducted using Cufflinks (version 2.0.2). Changes in expression between knockout and wild type animals or siRNA knockdown samples and control transfected cells (siNon) were calculated with Cuffdiff (version 2.0.2) (Trapnell et al. 2010). Fold changes (FC) for protein coding genes were filtered for an FPKM value equal or larger than one in at least one condition.

For the analysis of differential expressed isoforms, reads were mapped to the mouse reference genome (GENCODE M4: GRCm38.p3) using Kallisto (version 0.42.1) and differentially expressed genes were called with edgeR (version 3.6.8). Data were filtered for a FC ≥ 2 and a TPM (transcript per million) value larger than one in at least one condition. Heart (left and right ventricle) and skeletal muscle samples from Dpf3$^{-/-}$ mice were compared with samples from wild type littermates. Samples from Dpf3 siRNA knockdown experiments in HL-1 cells were compared with HL-1 cells that were transfected with a scrambled control siRNA.

Isoform proportion estimation was conducted with the mixture-of-isoforms (MISO) model (Katz et al. 2010). The reads were mapped using STAR (version 2.4.0) (Dobin et al. 2013), the files of the technical triplicates were merged into a single bam file and the MISO analysis was conducted using the GENCODE annotation for the mouse genome M4 and the isoform-centric analysis mode. The transcripts were filtered for protein coding transcripts and long

non-coding RNAs. The difference of isoform abundance between knockout or knockdown and control samples is represented by $\Delta\Psi$ values. Ψ (PSI, percent spliced in) values are computed by pairwise comparisons of transcripts taking into account exon junction reads that span from an alternative to an constitutive exon (alternative exon is included) or between two constitutive exons (alternative exon is excluded) and the read density of all exons of the gene. The mean Ψ values of each sample are substracted to result in $\Delta\Psi$. The distribution of estimated $\Delta\Psi$ values is used to calculate Bayes factors that reflect the likelyhood of differenital expression. The results were filtered for recommended Bayes factors ≥ 10 (Katz et al. 2010) and the 95 % quantile of the calculated $\Delta\Psi$ values between the knockout or knockdown and control samples.

Genes that showed an isoform proportion shift were further analyzed in respect of a role of Dpf3 in kinetic splicing regulation. For this, the transcripts were filtered for TPM values larger than one in the knockout or knockdown condition and exons with more than 10 % counts compared to controls (Figure 2.1). Subsequently, the exons were divided into exons with strong and weak inclusion scores (Shepard et al. 2011). Finally, the exons were overlapped with binding sites of histone modifications that are recognized by Dpf3 as well as binding sites of Brg1.

2.11.2 Genome-wide identification of protein-RNA interactions

4-Thiouridine (4SU) labeling and crosslinking

HEK293T or C2C12 cells were transiently transfected with pTL-Flag-Dpf3a and pTL-Flag-Dpf3b as described in section 2.8.3. 16 h before crosslinking and harvesting, 4SU was added to a final concentration of 100 μM (HEK293T) or 400 μM (C2C12). The next morning, the medium was decanted and the cells were crosslinked at 365 nm with 0.15 J cm^{-2} on ice. Immediately after irradiation, the cells were scraped off the plate in 5 ml cold Dulbecco's PBS and collected at 300 g for 10 min at 4 °C. The cell pellets were further processed or snap frozen and stored at -80 °C.

Cell lysis conditions

To work with optimal cell lysis conditions, the NP40 and the high salt lysis buffer were tested. Pellets of labeled and crosslinked cells were resuspended in three volumes of the respective lysis buffer and equally split into two vials per buffer. One sample per buffer was sonicated for 10 sec at 10 % amplitude with the Branson Digital Sonifier equipped with the 1/8″ tapered microtip (Branson Ultrasonics). All samples were incubated for 10 min on

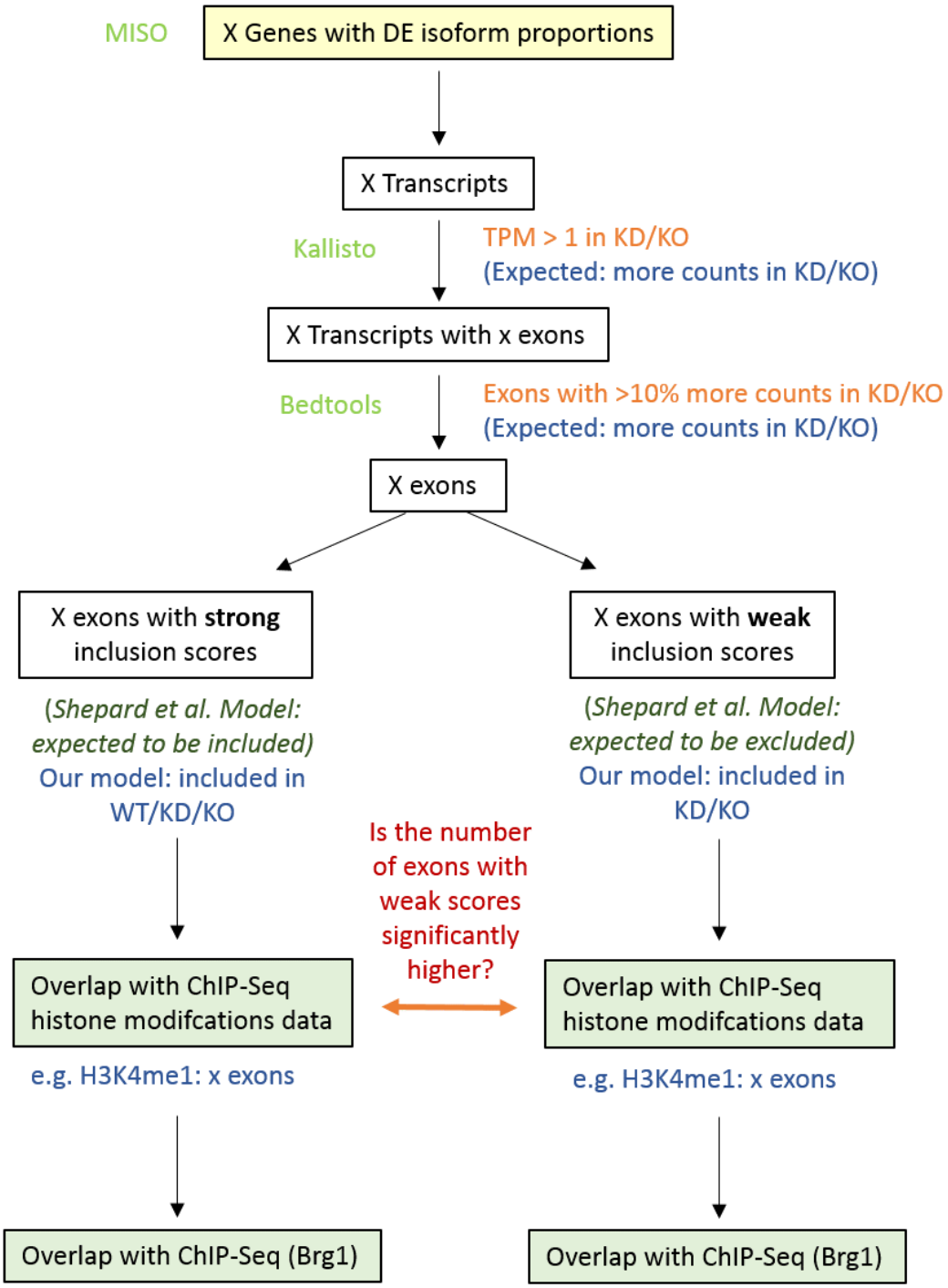

Figure 2.1: Schematic overview of the analysis of Dpf3 dependent exons Light green, analysis tools; orange, filter criteria; blue, expected results if Dpf3 influences the splicing outcome indirectly via the Pol II elongation rate; green, expected exon inclusion/exclusion based on inclusion scores; TPM, transcripts per million; KD, siRNA knockdown of Dpf3; KO, Dpf3 knockout.

ice and the lysates were cleared by centrifugation at 4 °C. The supernatants were loaded on 10 % Western blot gels (see section 2.8.12) and probed with anti-Flag(M2) (Sigma) and anti-vinculin (Sigma).

Analysis of 4SU incorporation

To assess the 4SU incorporation efficiency in C2C12 cells, the cells were transiently transfected with pTL-Flag-Dpf3a and labeled as described above. Cells incubated with 0 μM, 100 μM, 200 μM and 400 μM final 4SU concentrations were harvested after 3 h, 6 h, 9 h and 12 h labeling time. Accordingly transfected HEK293T cells were incubated with 100 μM final 4SU concentration and harvested after 12 h as positive control. RNA was isolated as described in section 2.8.10. 2 μg RNA were mixed with 2 μl 0.1 M Tris-HCl (pH 7.4), 4 μl 5 mM EDTA, 4 μl EZ-Link Biotin-HPDP (1 mg/ml stock concentration) and 8 μl RNAse-free water. After 3 h incubation at room temperature in the dark, the volume was increased to 100 μl with water and the biotinylated RNA was purified using Phase-Lock-Gel tubes and Phenol-chloroform-isoamylalcohol (1:1:24) followed by chloroform. The aquaeous phase was transfered to a Amersham Hybond-N+ membrane (GE Healthcare) and UV-crosslinked with two pulses of 1200 μJ. The membrane was blocked for 20 min in 10 % SDS, 1 mM EDTA/PBS and probed with 0.1 μg/ml streptdavidin-horseradish peroxidase (Thermo Fisher Scientific). After decreasing SDS/PBS washes (2x 10 %, 2x 1 %, 2x 0.1 %), the dots were visualized as described in section 2.8.12. The image was analyzed using ImageJ (version 1.50e) and the relative dot intensities from the experiment in C2C12 cells were normalized to the signal intensity from the HEK293T sample.

PAR-CLIP experiment

The small and large scale PAR-CLIP experiments were conducted according to Spitzer et al. (2014) with minor modifications. For small scale pilot experiments, two plates with transiently transfected HEK293T cells or four plates with transiently transfected C2C12 cells were labeled and crosslinked as described above. The final large scale experiment (Figure 2.2) was performed in duplicate with labeled and crosslinked HEK293T cells from 20 plates per sample (transiently transfected with pTL-Flag-Dpf3a). Deviate from Spitzer et al. (2014), the overexpression of Flag-tagged Dpf3 isoforms was evaluated by Western blotting (see section 2.8.12) before immunoprecipitation. Partial RNA digestion was achieved by an incubation for 8 min with RNase T1 (Fermentas) before immunoprecipitation and by an incubation for 7 min after the immunoprecipitation. After radiolabeling, the small scale experiments were analyzed by autoradiography and Western blot. For the large scale

experiment, the protocol was further followed. The RNA library was prepared with the TruSeq Small RNA Library Preparation Kit (Illunina) using the 3'-adapter NN-RA3, the 5' adapter oR5-NN and the PCR primers RP1 (forward primer) and RPI1 as well as RPI8 (reverse primers with barcodes). The cDNA libraries were amplified with 22 and 23 cycles. The library was purified by gel electrophoresis and the QIAquick Gel Extraction Kit (Qiagen) and concentrated by ethanol precipitation. The libraries were analyzed with the Qubit dsDNA HS Assay Kit (Thermo Fisher Scientific) and the Agilent High Sensitivity DNA Kit (Agilent Technologies) before single-end read sequencing on a HiSeq 2000 device (Illumina). The sequencing data were processed according to an in-house analysis pipeline developed by Marvin Jens (Berlin Institute for Medical Systems Biology, AG N. Rajewsky).

2.11.3 Genome-wide identification of protein-DNA interactions

ChIP experiments with HL-1 cells were performed using the MAGnify Chromatin Immunoprecipitation System (Thermo Fisher Scientific) according to the manufacturer's instructions with some modifications. Sonication was carried out at the Bioruptor UCD300 (Diagenode) by applying 30 cycle of 30 sec ON and 30 sec OFF with a short centrifugation after 15 min to obtain chromatin fragments of approximately 100–500 bp. The shearing efficiency was evaluated by gel electrophoresis with 1 % agarose gels. For the chromatin immunoprecipitation, 2 μg anti-H3K4me1 or anti-H4K16ac per 10^6 cells were bound to Dynabeads Protein A and G (1:1 mix). After immunoprecipitation and washing, the crosslinking was reversed by adding 8 μl of 5 M NaCl to 200 μl of eluted sample and incubation at 65 °C overnight. RNA and protein were digested with RNase A (0.05 mg/ml final concentration) and proteinase K (0.1 mg/ml final concentration). The ChIP DNA was purified using the ChIP DNA Clean & Concentrator kit (Zymo research) (elution in 30 μl elution buffer) and analyzed by qPCR (see Figure 9.2 in the appendix). The concentration was determined with the Qubit dsDNA HS Assay Kit (Thermo Fisher Scientific). The library preparation was performed using the NEXTflex Illumina ChIP-Seq Library Prep Kit (Bioo Scientific). After size selection on a 2 % agarose gel, the library was anaylzed with the Agilent High Sensitivity DNA Kit (Agilent Technologies). Single-read sequencing was performed on a HiSeq 2000 device (Illumina) in technical duplicates with eight pooled samples per lane using the TruSeq SR Cluster Kit v3-cBot-HS (Illumina) and the HiSeq Sequencing Kit (Illumina). Sequence reads were mapped to the mouse reference genome (mm9) using Bowtie (version 0.12.9) with default parameters and replicate BAM files were merged using SAM tools (version 0.1.18.0). Peaks were called using MACS (version 1.4.2) with a p-value cutoff of 0.0001.

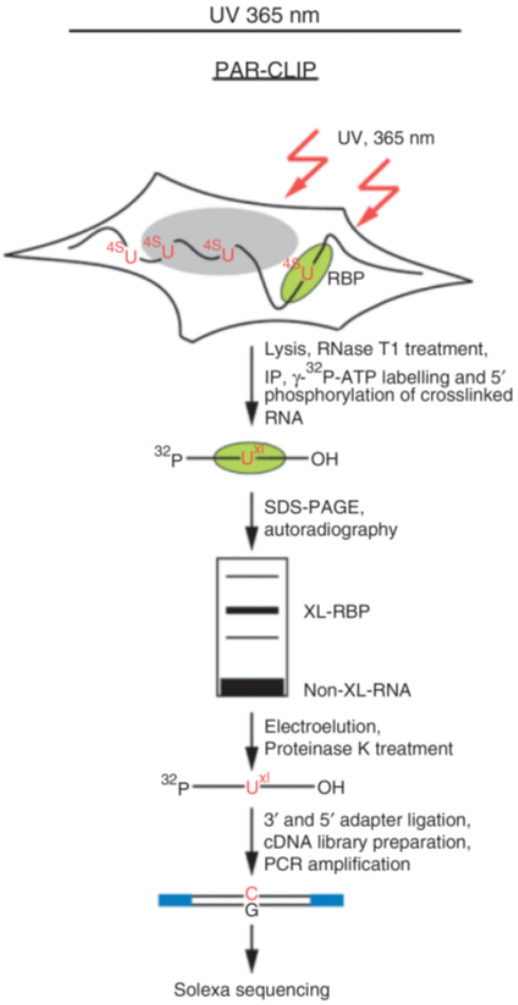

Figure 2.2: Schematic outline of the PAR-CLIP method. Overexpressed Flag/HA-tagged RNA binding proteins (RBP) bind to RNA labeled with 4SU that crosslinks to proteins upon exposure to UV light (365 nm). RNA-RBP complexes are isolated by immunoprecipitation and radioactively labeled for autoradiography after SDS-PAGE. After complex elution from the gel and protein digestion, the RNA fragments are ligated to 3' and 5' adapters. Finally, cDNA libraries are prepared and sequenced by next generation sequencing methods. (Figure taken from Ascano et al. (2012))

3 Results

3.1 Characterization of the Dpf3$^{-/-}$ mouse

In the past, the roles and functions of Dpf3 have been elucidated in cell culture models and in the zebrafish (Lange et al. 2008). With the generation of a Dpf3 knockout mouse strain, we took the next step towards the mammalian system. This mouse line opens up various opportunities to investigate the role of Dpf3 in the four-chambered heart and distinct muscle types.

3.1.1 The generation of the Dpf3$^{-/-}$ mouse strain

The Dpf3 knockout mouse line was generated with the Cre-lox system using the loxP strain *Dpf3^{tm1Sper}* (DIPF) and the cre strain CMV-cre (Schwenk, Baron, and Rajewsky 1995). The loxP strain was generated by the inGenious Targeting Laboratory, Inc. (iTL) by targeting the second DPF3 exon with LoxP sites and a Neomycin cassette (Figure 3.1) for clone selection in mouse embryonic stem cells (C57BL/6N) that were injected into Balb/c blastocysts. Chimeras were selected for high percentage of black coat color and mated with wild type C57BL/6N mice. Upon removal of the Neomycin cassette by matings with C57BL/6 FLP mice, the mice were brought to a C57BL/6 background. FLP-free mice (DIPF) harbour two loxP sites flanking the second exon of the Dpf3 gene sequence. Upon mating with CMV-cre mice, the second exon is excised by the Cre recombinase. Additionally, a frameshift and a stop codon arise. The cytotoxicity of the Cre recombinase and the occurence of cryptic loxP sites in the genome with a rate of one site per 1.2 megabase is well described (Schmidt-Supprian and Rajewsky 2007). Therefore, the Cre expressing Dpf3 knockout mice were back crossed with C57BL/6J mice resulting in the final Dpf3$^{-/-}$ strain which was named *Dpf3$^{tm1.1Sper}$* (Figure 3.1).

The deletion of the second exon of the Dpf3 gene sequence was validated by Sanger sequencing (Figure 3.1). The second exon is missing while the other exons are still detectable. The expected frameshift and the stop codon are verified. In addition, qPCR on heart, skeletal muscle and brain cDNA from Dpf3$^{-/-}$ mice and wildtype littermates showed no amplification

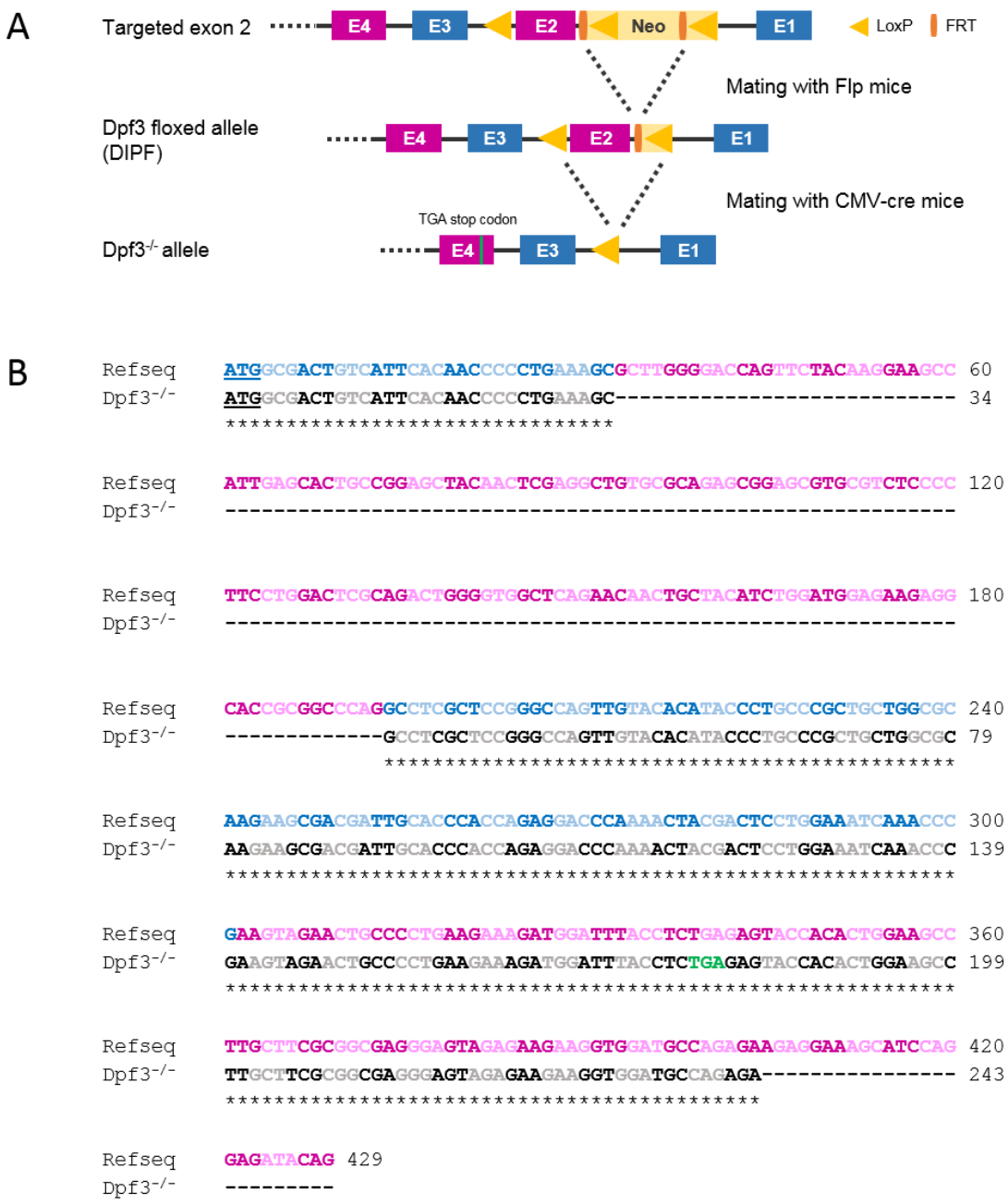

Figure 3.1: Generation of the Dpf3$^{-/-}$ mouse strain and confirmation of the knockout by Sanger sequencing. **A** Important breeding steps in the generation of the Dpf3$^{-/-}$ mouse strain; exons of the DPF3 gene sequence are represented by alternating blue and pink rectangles; Neo, neomycine cassette; introns are indicated by a black line. **B** Sanger sequencing of mouse heart cDNA from a Dpf3$^{-/-}$ mouse, exon sequences are colored according to A, triplets are indicated by alternating dark and light coloring, frameshift starts in the third exon, the stop codon is marked in green.

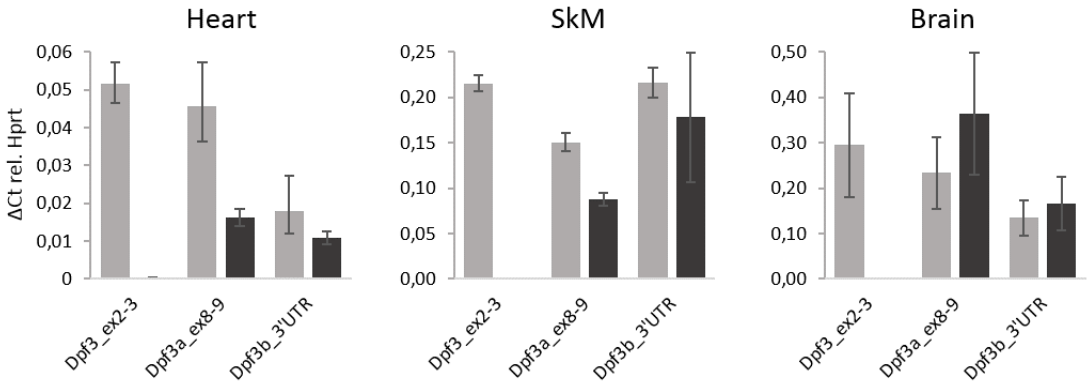

Figure 3.2: Quantitative PCR of Dpf3 in heart, skeletal muscle and brain. Amplification of indicated Dpf3 exons are shown in relation to Hprt expression; light gray, cDNA from wildtype animals was used; dark gray, cDNA from Dpf3$^{-/-}$ mice was used for qPCR.

product in knockout animals for the primer pair spanning the second and third exon (Figure 3.2). The protein level of Dpf3 was analyzed using an anti-pDpf3a antibody that was generated for the analysis of the phosphorylation at serine 348 of Dpf3a (H. Cui et al. 2015). Under standard Western Blot and immunostaining conditions, Dpf3 specific signals were not obtained in tissue samples from heart or skeletal muscles. Using signal amplification kits based on biotin-avidin binding and tyramide amplification revealed a nuclear staining of pDpf3a in the Tibialis anterior from wild type animals but also strong background staining (Figure 3.3). The corresponding staining in the tissue from knockout animals seems to be unspecific.

The matings were monitored by PCR and qPCR on genomic DNA isolated from ear or tail biopsies. The primers for genotyping target the loxP sites, the second exon of Dpf3, adjacent intronic regions and the Cre gene sequence (Figure 3.4 A). Wildtype mice are characterized by one band at 1510 bp, the presence of the floxed sequence of the second exon was displayed by a 1781 bp band and the deletion of exon 2 (homozygous mice) was detected via a 907 bp band (Figure 3.4 B). Heterozygous mice showed a mix of the band sizes described above. The expression of the Cre recombinase was detected by PCR (400 bp band) (Figure 3.4 C) and qPCR (Figure 9.1 in the appendix).

The inheritence of the Dpf3$^{-/-}$ allele followed the Mendelian laws with 23 % wildtype, 50 % heterozygous and 27 % homozygous offspring from heterozygous matings (Table 3.1). The distribution of female to male mice was balanced (Table 3.1). The fertility with 9 $\pm$ 2 pups per litter (n = 23) in heterozygous matings was better compared to homozygous matings (6 $\pm$ 2 pups per litter, n = 5). The animals were viable and the Dpf3$^{-/-}$ mice were visually indistinguishable from wildtype littermates (Figure 3.5). The body weights of Dpf3$^{-/-}$ and

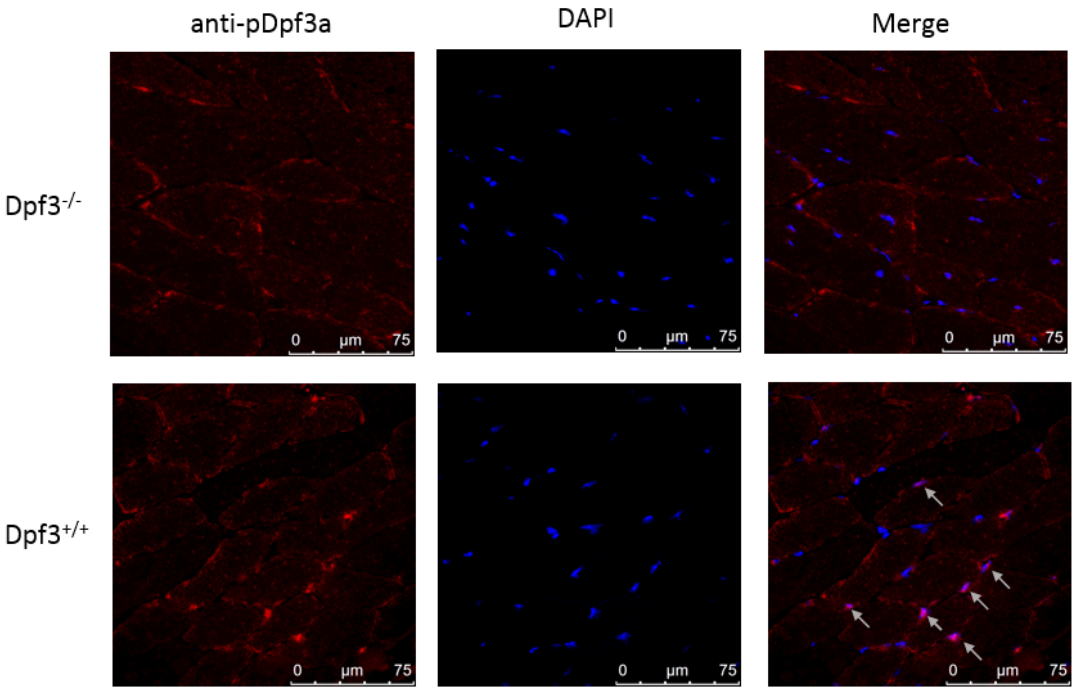

Figure 3.3: Immunostaining of pDpf3a in the Tibialis anterior of Dpf3 knockout mice and wild type littermates. pDpf3a is stained in red, nuclei are counterstained with DAPI (blue). Arrows mark nuclei stained with anti-pDpf3a.

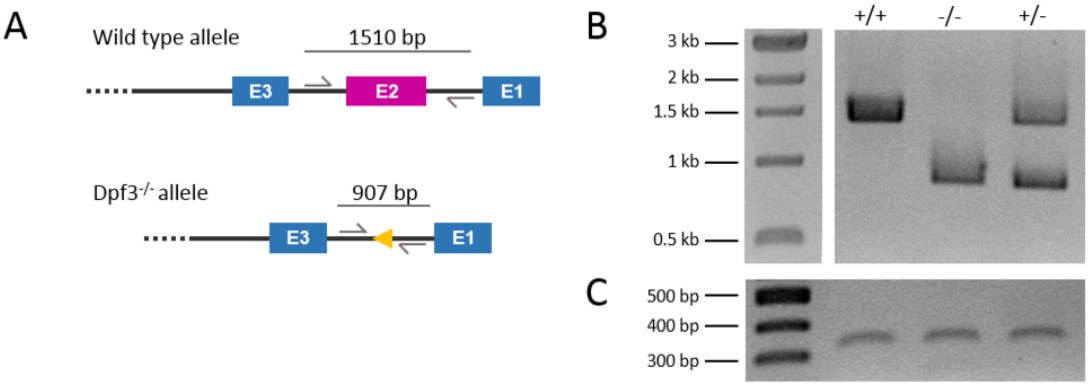

Figure 3.4: Genotyping of the Dpf3$^{-/-}$ mouse strain. A Schematic primer alignment in the wild type and Dpf3$^{-/-}$ allele. **B** Representative genotyping bands in wild type (+/+), heterozygous (+/-) and homozygous (-/-) Dpf3 knockout mice. **C** The presence of the Cre recombinase sequence in the mouse genome resulted in 400 bp bands after PCR.

Table 3.1: Dpf3 allele distribution after heterozygous matings.

Sex	Number	Dpf3$^{+/+}$	Dpf3$^{+/-}$	Dpf3$^{-/-}$
both	205	47 23 %	103 50 %	55 27 %
female	100	22 22 %	50 50 %	28 28 %
male	105	25 24 %	53 50 %	27 26 %

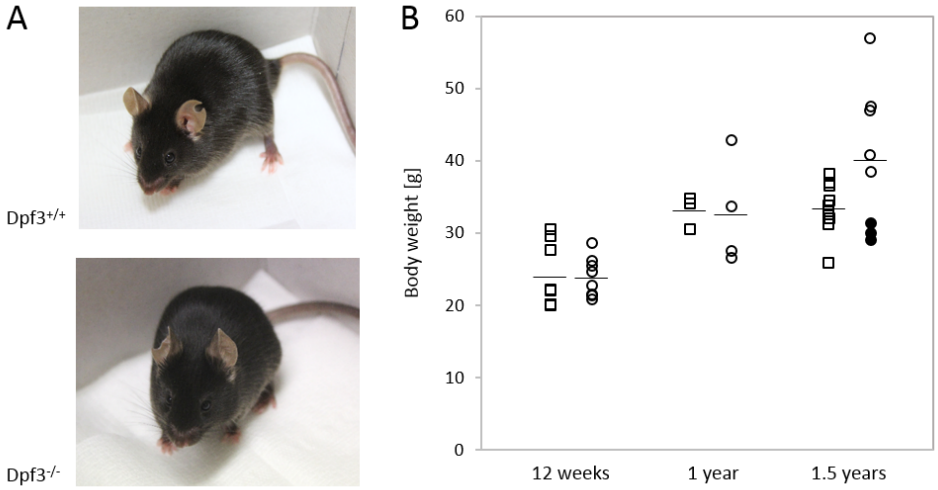

Figure 3.5: Outer appearance and body weights of the Dpf3$^{-/-}$ mouse strain. A Wild type and Dpf3$^{-/-}$ mice are indistiguishable. **B** Body weights of Dpf3$^{-/-}$ mice (circles) and control animals (rectangles); filled circles, body weights of animals with a phenotype (see 3.1.3); bar, mean value.

wildtype controls increased with age and were similar for both animal groups until the age of one year. The average body weight of the control animals shows a modest increase from 33.1 g to 33.4 g. In contrast to this, the average body weights of knockout animals increased from 32.6 g at the age of one year to 40.1 g at the age of 1.5 years. Moreover, the body weights at the age of 1.5 years spread over a wider range (minimum of 29 g to maximum of 56.9 g) compared to controls. Animals with a phenotype (see 3.1.3) have a relatively low body weight (Figure 3.5).

3.1.2 The impact of Dpf3 on gene expression

Changes in gene expression upon the deletion of Dpf3 were analyzed by RNAseq in 12 week old Dpf3$^{-/-}$ mice and wild type littermates. RNA was isolated from skeletal muscle tissue and the left and right ventricle of the heart. For comparison of *in vivo* and *in vitro* expression, RNAseq was performed on RNA from the mouse cell line HL-1 after siRNA knockdown of Dpf3. A pool of four siRNAs targeting both or single Dpf3 isoforms resulted in 71.5 % knockdown of Dpf3a and 57 % knockdown of Dpf3b.

Read mapping resulted in 70 % uniquely mapped reads in the heart samples, 75.7 % uniquely mapped reads in the skeletal muscle samples and 80.2 % uniquely mapped reads in the HL-1 cell samples. Fold changes (FC) in expression of protein coding genes were filtered for an FPKM (fragments per kilobase of transcript per million fragments mapped) value equal or larger than one in at least one condition. The number of genes with an up- or downregulation of at least 1.5-fold is given in Table 3.2. In each sample, the number of up- and downregulated genes is balanced. The gene names are listed in the appendix (chapter 9.1).

With few exceptions, the changes in gene expression are below a sixfold up- or downregulation ($|0.58| \leq \text{Log}_2\ (\text{FC}) \leq |2.7|$) (Figure 3.6). More than 75 % of differentially expressed genes in each sample do not exceed a twofold up- or downregulation ($\text{Log}_2\ (\text{FC}) \geq |1|$). In the left ventricle of Dpf3$^{-/-}$ mice, 83 genes (14 %) are more than twofold up- or downregulated compared to the expression level in wild type littermates. For the right ventricle and skeletal muscle, 75 genes (22 %) and 74 genes (25 %) fall into this category, respectively. Upon the siRNA-knockdown of Dpf3 in HL1-cells, 37 genes (25 %) show a more than twofold up- or downregulation compared to control transfections.

Taking into account the gene expression level, the genes with the strongest up- or downregulation upon the depletion of Dpf3 tend to be lowly expressed in the basic situation (wild type mice or HL-1 cells transfected with a scrambled siRNA) (Figure 3.6). Only 12 to 14 genes in the heart and skeletal muscle samples shwo a strong up- or downregulation ($\text{Log}_2\ \text{FC} \geq |1|$) that starts from a higher expression level (FPKM > 10). In the Dpf3 siRNA knockdown sample, six genes are characterized by a strong up- or downregulation starting from higher expression levels. Among these genes, three are upregulated in both Dpf3$^{-/-}$ heart samples as well as the Dpf3 siRNA knockdown (HL1-cells) sample: the co-chaperone and protein trafficking protein Fkbp8, the cytochrome oxidase subunit Cox5b and a putative splicing factor 2310036O22Rik (orgholog to the human splicing factor C19orf43). The highly expressed skeletal muscle α-Actin (Acta1) is upregulated in both Dpf3$^{-/-}$ heart samples whereas the cardiac α-Actin (Actc1) is upregulated in skeletal muscles from Dpf3$^{-/-}$ mice.

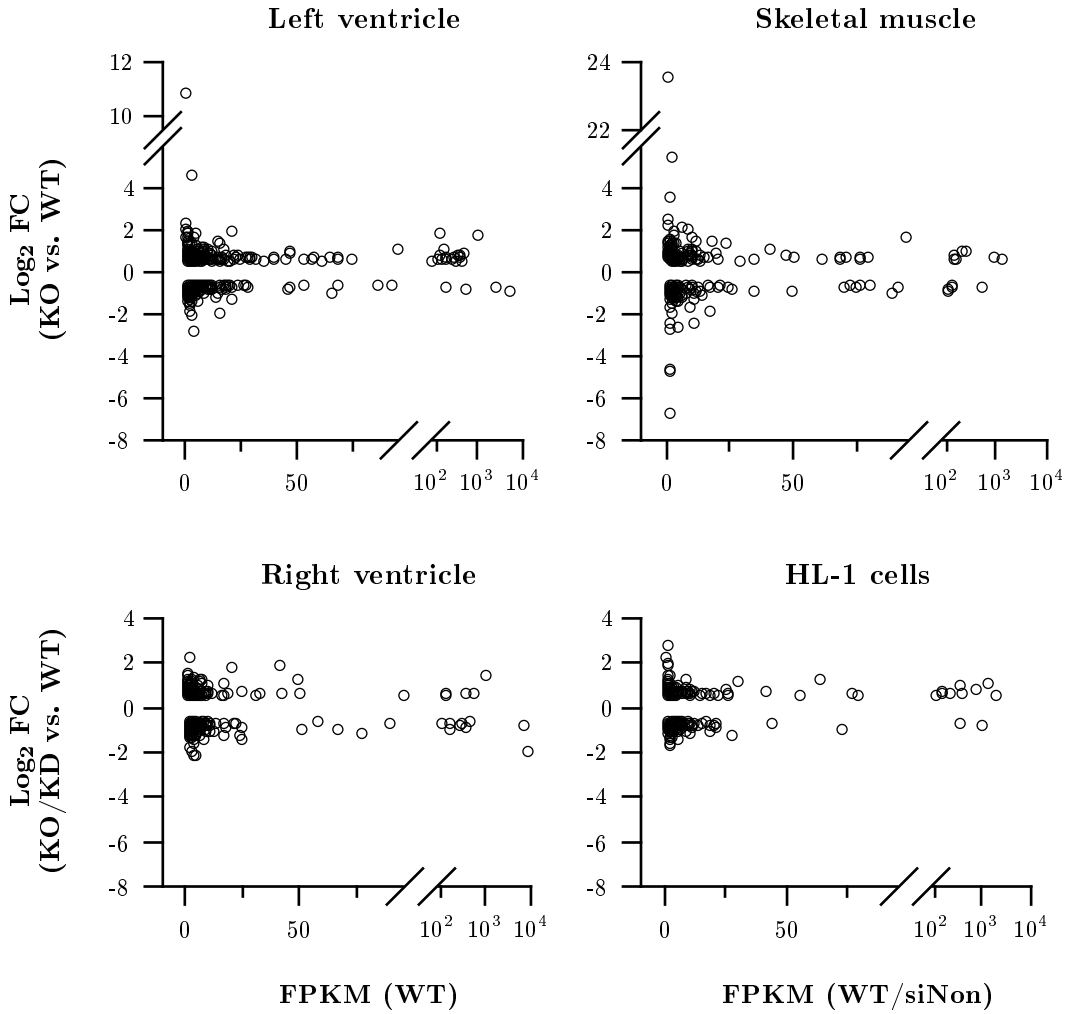

Figure 3.6: Differential gene expression upon the loss of Dpf3 in relation to the gene expression levels in the control conditions. Changes in gene expression between Dpf3$^{-/-}$ mice (KO) and wild type littermates (WT) or siRNA knockdown (KD) of Dpf3 in HL-1 cells and control transfections (siNon) are given in Log_2 FC with a cutoff of Log_2 FC $\geq |0.58|$. The gene expression levels in the control conditions are expressed in FPKM (fragments per kilobase of transcript per million fragments mapped) values. FC, fold change.

Table 3.2: Number of up- and downregulated genes in Dpf3$^{-/-}$ mice and after siRNA knockdown in HL-1 cells.

	LV	RV	SkM	HL-1
Up-/downgregulated genes total	595	339	293	243
Upregulated genes	304	167	139	125
Downregulated genes	291	172	154	118

Changes in gene expression between Dpf3$^{-/-}$ mice and wild type littermates or Dpf3 siRNA knockdown and control transfection of HL-1 cells are equal to or more than 1.5-fold; LV, left ventricle; RV, right ventricle; SkM, skeletal muscle.

The changes in gene expression measured by RNAseq were validated by qPCR for selected genes. There is a good correlation between fold changes based on FPKM values (RNAseq) and fold changes in relation to the expression of Hprt (qPCR) (Figure 3.7). Expression values for the samples from wild type animals or siRNA control transfections are set to one.

Dpf3 belongs to the d4 gene family with its additional members Dpf1 and Dpf2. The expression of Dpf1 is restricted to the central and peripheral nervous system (Buchman et al. 1992) whereas Dpf2 shows a ubiquitous expression pattern (Gabig, Crean, et al. 1998). All d4 proteins have been detected in BAF chromatin remodeling complexes (Lange et al. 2008; Lessard et al. 2007). An additional PHD finger protein, PHF10, has been shown to be replaced by Dpf1 or Dpf3 during neuronal differentiation (Lessard et al. 2007). Thus, the mRNA level of Dpf1, Dpf2 and PHF10 in Dpf3$^{-/-}$ mice and wild type littermates were of particular interest. As shown in Figure 3.8, the expression level of the Dpf3 orthologs does not change in the absence of Dpf3.

3.1.3 Physical and histologic examination of Dpf3$^{-/-}$ mice

Four animals groups were physically and histologically examined: One year old Dpf3$^{-/-}$ mice, one year old Dpf3$^{+/+}$ littermates, 1.5 years old Dpf3$^{-/-}$ mice and 1.5 years old C57BL/6J mice. The 1.5 years old knockout animals still expressed the Cre recombinase, the one year old animals were Cre-free. Cage activities such as food intake, grooming and running were normal for the one year old animals and the 1.5 years old control mice. Among the 1.5 years old Dpf3$^{-/-}$ mice, three out of eight animals showed stereotypic running behaviour (circling) to various degrees (Table 3.3).

Hearts from Dpf3$^{-/-}$ mice and control animals were dissected, weighed and stained with hematoxylin and eosin (HE). No significant difference was noticed in the heart to body

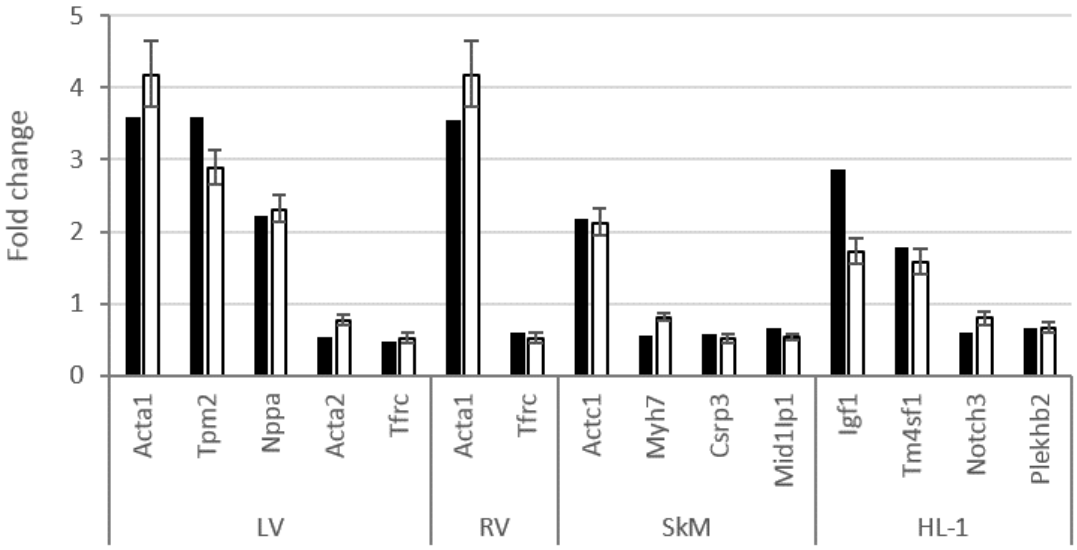

Figure 3.7: Validation of FPKM fold changes by qPCR. Black, fold changes between FPKM values of Dpf3$^{-/-}$ mice and wild type littermates or between FPKM values after Dpf3 siRNA knockdown and control transfection of HL-1 cells, expression values for controls are set to one; white, fold changes in expression relative to Hprt determined by qPCR, expression values for controls are set to one; LV, left ventricle; RV, right ventricle; SkM, skeletal muscle.

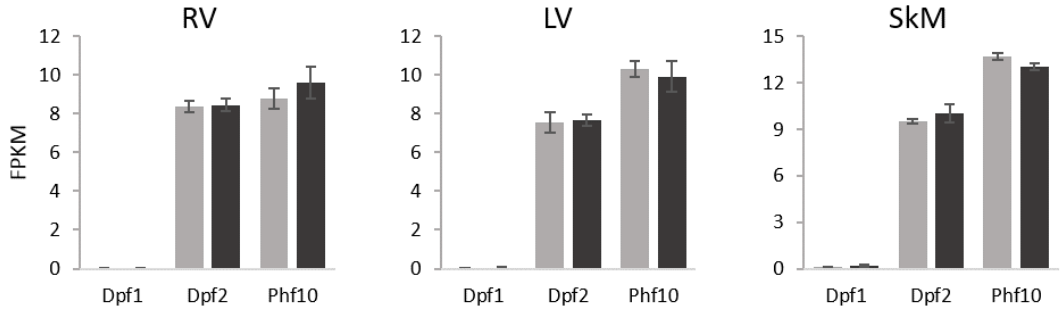

Figure 3.8: Expression levels of Dpf3 orthologs in Dpf3$^{-/-}$ mice. Expression levels were determined in the indicated tissues from 12 week old Dpf3$^{-/-}$ mice (dark gray) and wildtype littermates (light gray) by RNAseq; RV, right ventricle; LV, left ventricle; SkM, skeletal muscle.

Table 3.3: Running behaviour in cages of 1.5 years Dpf3$^{-/-}$ mice.

Mouse ID	Sex	EDL phenotype	Behaviour	Cage ID	Cage info
W44-116	M	Centralized nuclei	Circling	33	5 additional mice, 2 of them circling
W44-122	F	Some centr. nuclei	Sometimes circling	34	1 additional mouse, normal behaviour
W44-123	F	Centralized nuclei	Normal		
W44-125	F	Centralized nuclei	Circling		
W44-134	M	Normal	Normal	37	2 additional mice, normal behaviour
W44-137	M	Normal	Normal		
W44-138	M	Normal	Normal		
W44-140	F	Some centr. nuclei	Normal	38	5 additional mice, normal behaviour

EDL, extensor digitorum longus; F, female; M, male.

weight ratios of Dpf3$^{-/-}$ animals compared with controls (Figure 3.9). Also the HE stainings were indistinguishable between the animal groups at both time points (Figure 3.10).

For the examination of skeletal muscles, the soleus, tibialis anterior (TA) and extensor digitorum longus (EDL) were dissected from the hind limbs of the animal groups described above. The skeletal muscle to body weight ratios are similar for the muscle types analyzed (Figure 3.11). However, the muscle to body weight ratios of animals with a phenotype (see below) cluster at high ratios. The HE staining of all muscle types from one year old mice is comparable between knockout and wildtype animals (Figure 3.12). Here, the myonuclei are located in the periphery of the myofibres. The same localization of myonuclei is observed in the soleus fibres of 1.5 years old mice. Besides peripherally placed nuclei, a myonuclear centralization occurs in the TA and EDL of some Dpf3$^{-/-}$ mice. The TA is altered in three out of eight Dpf3$^{-/-}$ mice throughout the whole cross-sectional area and the EDL of these animals shows the same phenotype. Additionally, a myonuclear centralization in the EDL is detected in two other Dpf3$^{-/-}$ mice at some spots. In all control groups, the vast majority of muscle fibres contains peripherally located nuclei and the number of central myonuclei does not exceed the natural abundance of up to 5 % (Caccia, Harris, and Johnson 1979; Wood et al. 2014; Barns et al. 2014).

To assess the impact of Dpf3 on the molecular structure of fast twitch skeletal muscles, several sarcomeric proteins were visualized by immunostainings in EDL and TA muscles from 1.5 years old animals. According to the α-actinin and desmin staining (Figure 3.13 and Figure 3.14), the integrity of the z-disc is given in both animal groups. Fibrillar actin is stained by phalloidin and results in 1.5 years old Dpf3$^{-/-}$ mice as well as control animals in an regular striation pattern (Figure 3.13 and Figure 3.14). This result is replicated by

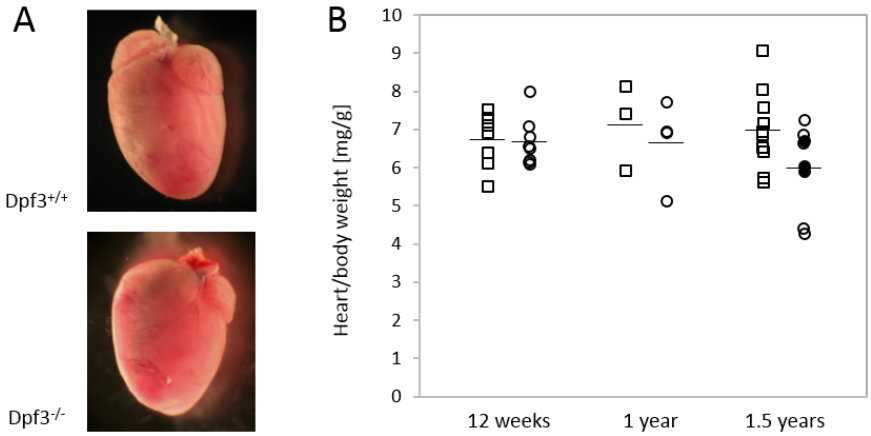

Figure 3.9: Hearts and heart to body weight ratios in the Dpf3$^{-/-}$ strain. A Hearts of wild type and Dpf3$^{-/-}$ mice are indistiguishable. **B** Heart to body weight ratios of Dpf3$^{-/-}$ mice (circles) and control animals (rectangles); filled circles, animals with a phenotype (see text); mean values are indicated by small bars.

staining of tropomyosin, which is wrapped around the actin polymers (Figure 3.13). Also the thick filaments seem to align in parallel patterns as shown by staining of fast myosin isoforms (Figure 3.13). The centralization of the myonuclei in some Dpf3$^{-/-}$ mice seems not to disturb the parallel sarcomeric structures.

The myosin heavy chain composition within skeletal muscles is mainly dependent on the muscle type. However, exercise, age or regeneration have an additional impact on the myosin isoform expression pattern (Wernig, Irintchev, and Weisshaupt 1990). To examine if the centralization of myonuclei is fibre type dependent, the slow myosin (myosin type I) was stained in the TA and EDL of 1.5 years old Dpf3$^{-/-}$ mice. This staining reveals some myosin type I positive fibres that have a smaller cross sectional area compared to non-stained fast twitch fibres (Figure 3.15). In most cases, the stained fibres contain peripheral myonuclei and rarely centralized nuclei. However, the occurence of fibres with nuclei exclusively in the periphery does not always overlap with the slow myosin staining.

3.1.4 Conclusion

The generation of the Dpf3 knockout mouse strain *Dpf3$^{tm1.1Sper}$* was achieved via the cre-lox system and resulted in viable and fertile animals that pass on the Dpf3$^{-/-}$ allele according to the Mendelian laws. The loss of Dpf3 alters the expression of $\sim$ 300 to 600 genes in heart and skeletal muscle samples from 12 week old animals. The expression levels of orthologous proteins are not affected in the knockout condition. The physical and histologic examination

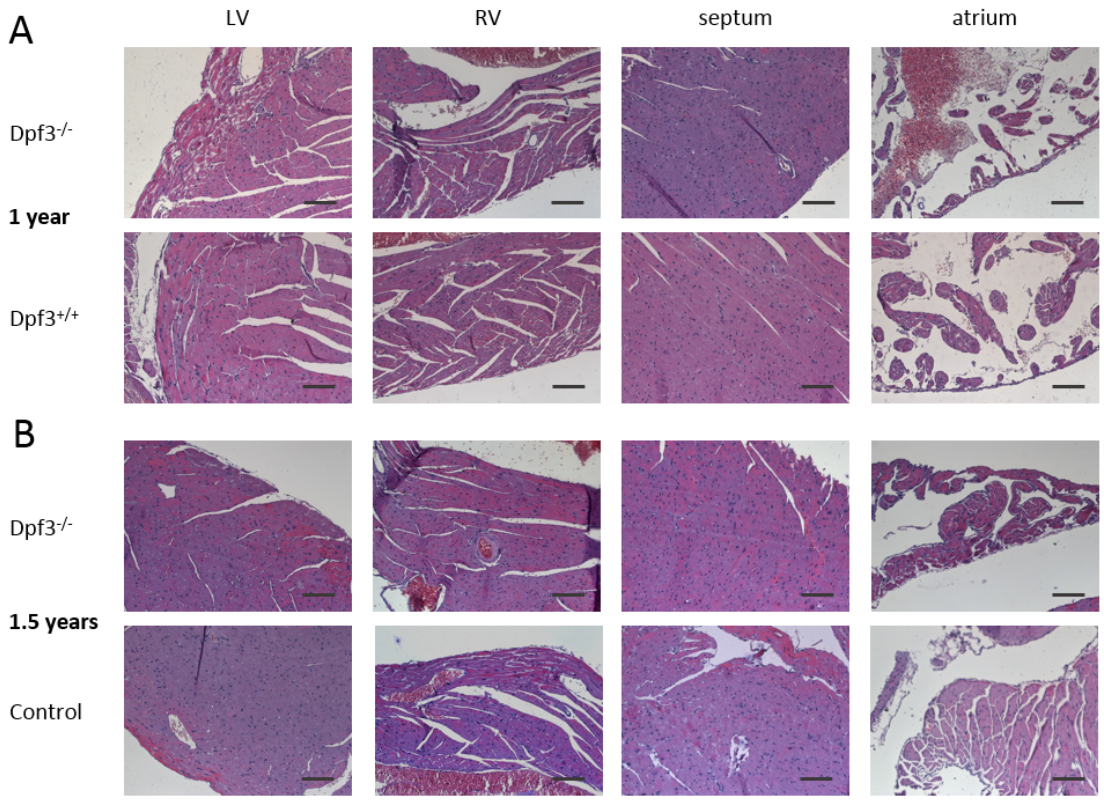

Figure 3.10: Hematoxylin and eosin staining in hearts of Dpf3$^{-/-}$ mice. A Sagittal paraffin sections (5 μm) of hearts from 1 year old Dpf3$^{-/-}$ mice and wild type littermates. **B** Sagittal paraffin sections (5 μm) of hearts from 1.5 years old Dpf3$^{-/-}$ mice and control animals; LV, left ventricle; RV, right ventricle; scale bar, 100 μm.

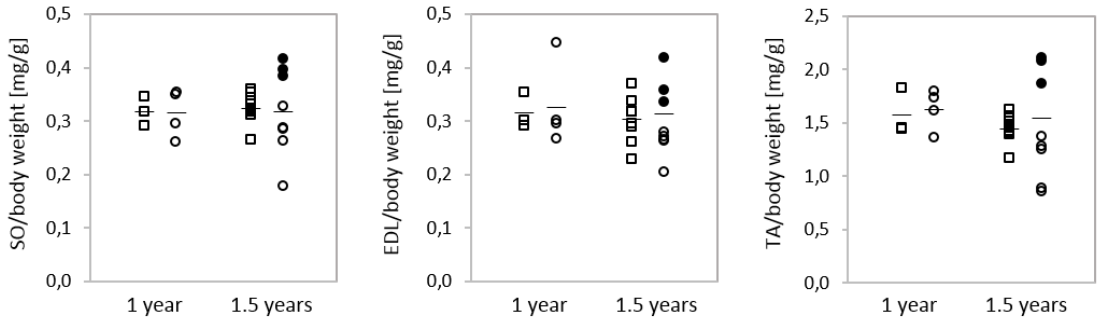

Figure 3.11: Skeletal muscle to body weight ratios in the Dpf3$^{-/-}$ strain. The skeletal muscle to body weight ratios for the indicated muscle types were calculated for Dpf3$^{-/-}$ mice (circles) and control animals (rectangles); filled circles, animals with a phenotype (see text); SO, soleus; EDL, extensor digitorum longus; TA, tibialis anterior.

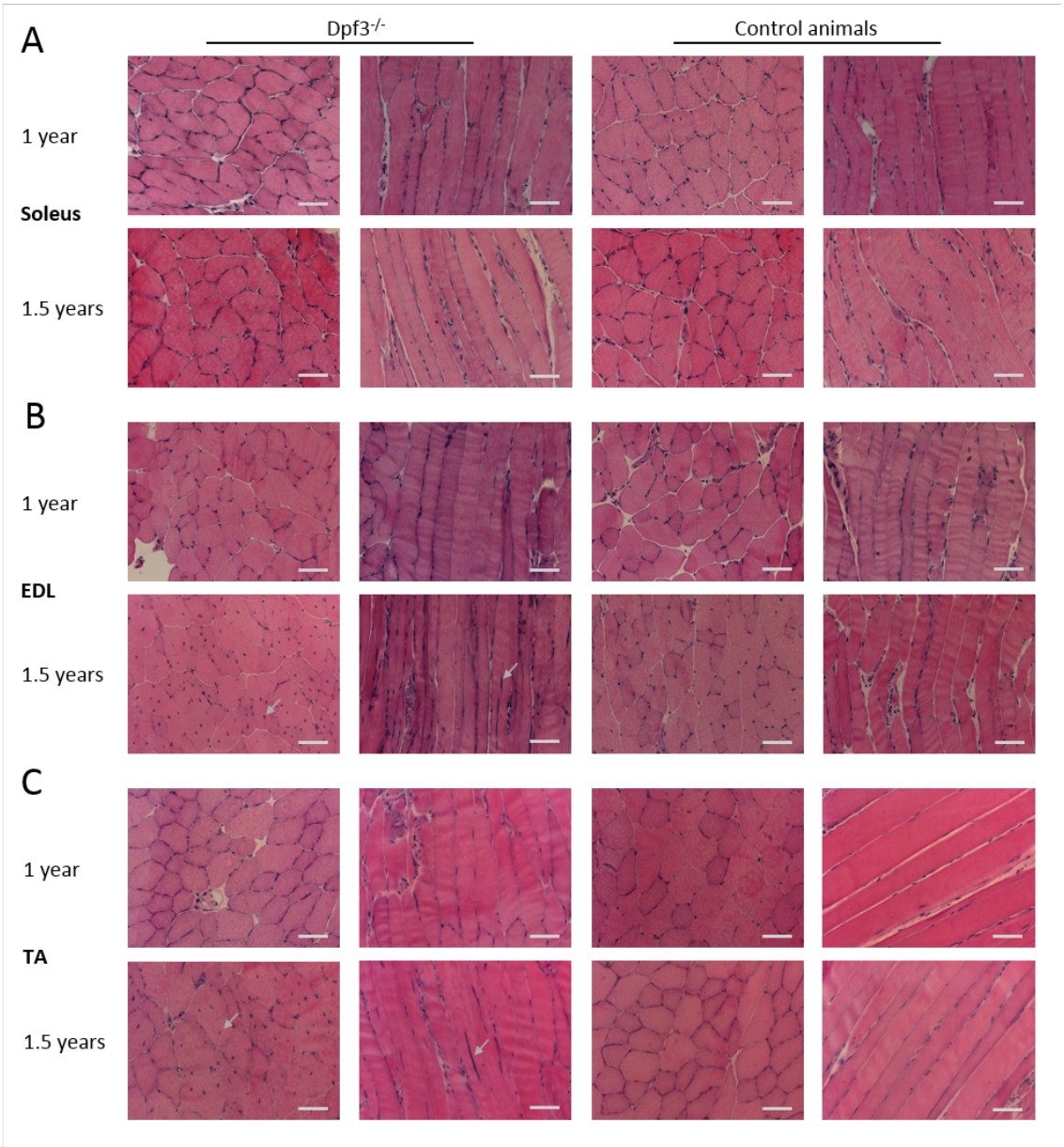

Figure 3.12: Hematoxylin and eosin staining of skeletal muscle types in the Dpf3$^{-/-}$ strain. **A** Transversal and longitudinal cryosections (6 μm) of the soleus from Dpf3$^{-/-}$ mice and controls. **B** Transversal and longitudinal cryosections (6 μm) of the extensod digitorum longus (EDL) from Dpf3$^{-/-}$ mice and controls C Transversal and longitudinal cryosections (6 μm) of the tibialis anterior (TA) from Dpf3$^{-/-}$ mice and controls; the animal age is indicated on the left; scale bar, 50 μm.

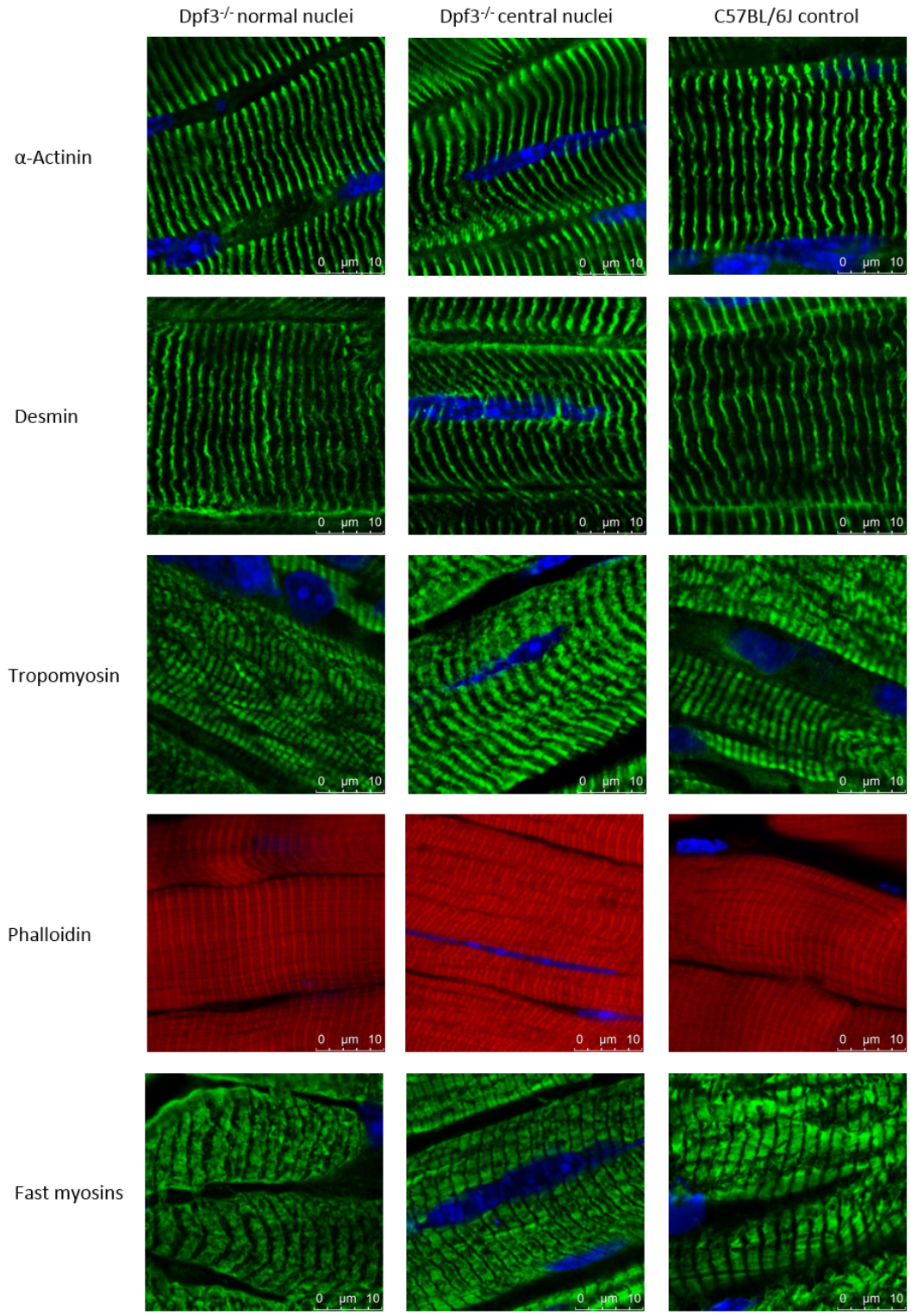

Figure 3.13: Immunostaining of sarcomeric proteins in EDL of 1.5 years Dpf3$^{-/-}$ mice and control animals. 6 μm longitudinal cryosections; sarcomeric proteins (green or red) and animal groups are indicated; blue, DAPI.

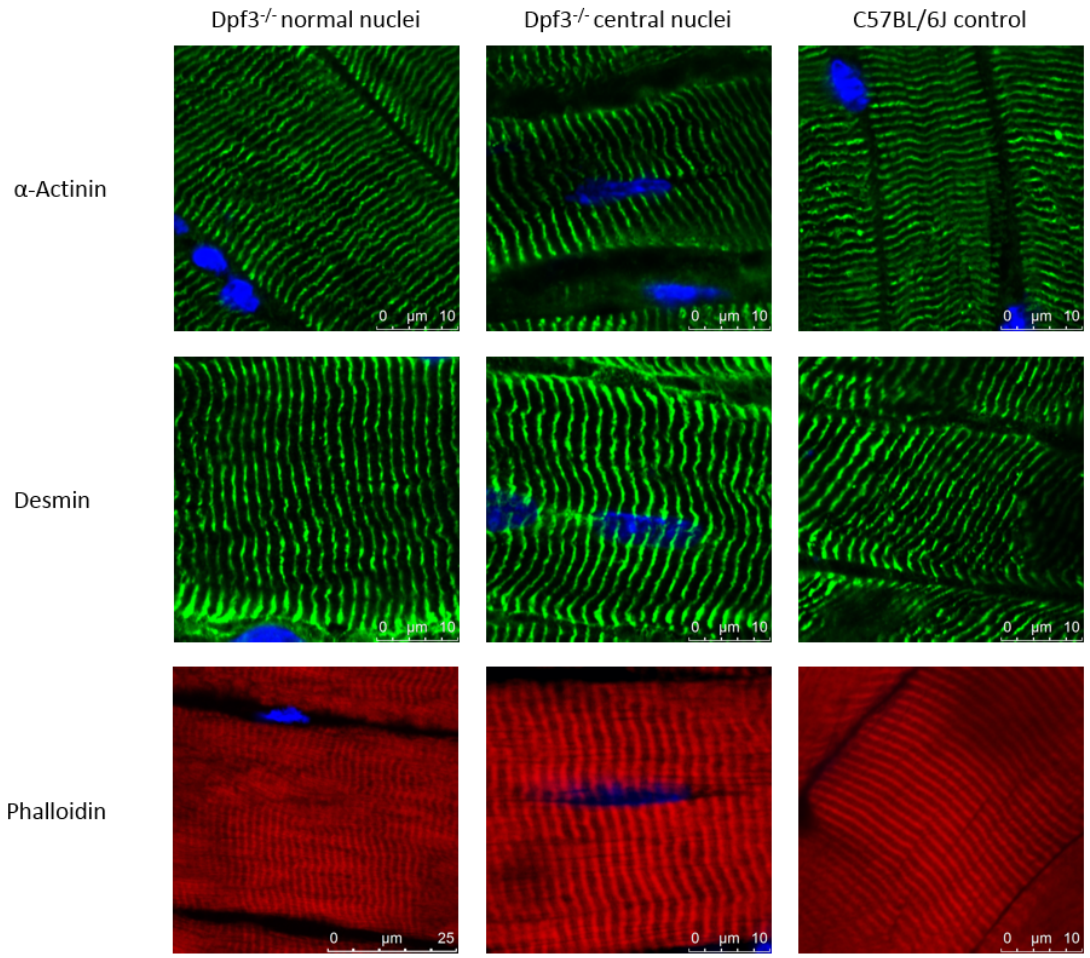

Figure 3.14: Immunostaining of sarcomeric proteins in TA of 1.5 years Dpf3$^{-/-}$ mice and control animals. 6 μm longitudinal cryosections; sarcomeric proteins (green or red) and animal groups are indicated; blue, DAPI.

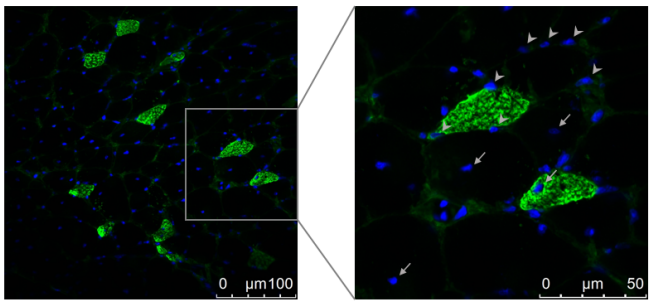

Figure 3.15: Immunostaining of slow myosin in the EDL of a 1.5 years Dpf3$^{-/-}$ mouse. 6 μm transversal cryosection; green, slow myosin heavy chain; blue, DAPI; arrow, centralized nucleus; arrow head, peripheral nucleus.

of Cre-free Dpf3$^{-/-}$ and wild type littermates up to the age of one year was similar in both animal groups. In 1.5 years old knockout animals still expressing the Cre recombinase, a fibre-type dependent phenotype with incomplete penetrance, that is characterized by myonuclear centralizations in the fast-twitch muscles EDL and TA, was observed. The striated patterns of sarcomeric proteins in the EDL and TA of Dpf3$^{-/-}$ mice is regular irrespective of the myonuclear location. The myonuclear positionig in the soleus (slow-twitch muscle) is not affected by the loss of Dpf3.

3.2 The impact of Dpf3 on alternative splicing

Based on results from tandem affinity purification followed by mass spectrometry (TAP-MS) (see section 3.3.2) and from a yeast two-hybrid (Y2H) screen (see section 3.3.1), an interaction of DPF3 with the spliceosome was postulated. To investigate if these interactions are relevant *in vivo*, alternative splicing patterns in the presence and absence of Dpf3 were compared.

3.2.1 Differential expressed isoforms after knockout and knockdown of Dpf3

As outlined in section 3.1.2, RNA isolated from heart and skeletal muscle of the Dpf3$^{-/-}$ mouse strain as well as RNA from Dpf3 siRNA knockdown experiments in HL-1 cells were analyzed by next generation sequencing. These data sets were analyzed in respect of differential isoform expression between tissue samples from Dpf3$^{-/-}$ mice and wild type littermates and between samples from Dpf3 siRNA knockdown experiments in HL-1 cells and transfections with a scrambled control siRNA (see chapter 2.11.1. The average number of uniquely mapped reads for all samples was 93.5 %. The number of differentially expressed transcripts that pass the filter criteria (FC ≥ 2 and a TPM (transcript per million) larger than one in at least one condition) ranges from 553 to 757. The number of up- and downregulated isoforms is balanced (Table 3.4). Overrepresented pathways include "striated muscle contraction", "cardiac muscle contraction", "signaling" and "spliceosome". These keywords match with GO terms such as "striated muscle", "myofilament", "heart contraction", "sarcomere" or "cardiac chamber development" (Table 3.4).

The underlying causes for the changes in transcript expression upon the loss of Dpf3 can be of different manner. In one case, the expression level of every transcript of a certain gene might be elevated or reduced to the same extend. For these genes, the splicing outcome is not affected by the loss of Dpf3. In another case, the expression level of a subset of transcripts of a certain gene is elevated or reduced due to an altered splicing regulation in the Dpf3

Table 3.4: Differential expressed isoforms in the absence of Dpf3.

	LV_KO vs. LV_WT	RV_KO vs. RV_WT
# Transcripts	713 (630 genes)	553 (481 genes)
	Up: 336	Up: 285
	Down: 377	Down: 268
Pathways	81	3
(FDR $\leq$ 5 %)	Striated Muscle Contraction, mRNA Splicing, Signaling, Cardiac Muscle Contraction, Trancriptional Activity (SMAD2/3,4), Spliceosome	Striated Muscle Contraction, TCA cycle and respiratory electron transport, Cardiac Muscle Contraction
GO terms	283	190
(FDR $\leq$ 5 %)	BP: 160 CC: 86 MF: 37	BP: 98 CC: 83 MF: 9
	Intracellular, Cytoplasm, Sarcomere, Muscle System/Development, Myofilament, Actomyosin, Cardiac Chamber Development, Cardiac Ventricle Development	Intracellular, Cytoplasm, Sarcomere, Muscle System, Striated Muscle, Myofilament, Adult Heart Development, Actomyosin, Heart Contraction, Muscle Development
	SkM_KO vs. SkM_WT	siDpf3 vs. siNon
# Transcripts	666 (574 genes)	757 (684 genes)
	Up: 288	Up: 428
	Down: 378	Down: 329
Pathways	75	74
(FDR $\leq$ 5 %)	Striated Muscle Contraction, mRNA Processing, Signaling, Muscle Contraction, Immune System, mRNA Stability	miRNAs in Cardiomyocyte, Hypertrophy, Muscle contraction, Toll Like Receptor, Signaling Pathways, SUMO
GO terms	244	191
(FDR $\leq$ 5 %)	BP: 166 CC: 57 MF: 21	BP: 103 CC: 61 MF: 27
	Intracellular, Cytoplasm, Sarcomere, Muscle Cell Differentiation, Myosin Complex, Heart Development, Regulation of heart rate	Intracellular, Organelle, Metabolic process, Actin binding, Striated Muscle, Myofilament, Death, Muscle Structure Development

Transcripts are filtered for FC $\geq$ 2 and a TPM $>$ 1; siDpf3, siRNA knockdown in HL-1 cells; siNon, control transfection with a scrambled siRNA;RV, right ventricle; LV, left ventricle; SkM, skeletal muscle; vs, versus; Pathways, based on KEGG, Reactome and Wikipathways; GO, gene ontology; BP, biological process; CC, cellular component; MF, molecular function.

Table 3.5: Genes with isoform proportion shifts in the absence of Dpf3.

	LV_KO vs. LV_WT	RV_KO vs. RV_WT
# Genes	218	175
Pathways	60 (FDR $\leq$ 5 %)	9 (FDR $\leq$ 5 %)
	mRNA Processing, mRNA Splicing, Signaling Pathways	Signaling,SUMO, Circadian Regulation
GO terms	66	27
(FDR $\leq$ 5 %)	BP: 15 CC: 26 MF: 25	BP: 3 CC: 19 MF: 5
	Cytoplasm, Intracellular, Nucleotide binding, Cellular localization	Intracellular, Organelle, Cytoplasm, U5 snRNP
	SkM_KO vs. SkM_WT	**siDpf3 vs. siNon**
# Genes	97	171
Pathways	3 (FDR $\leq$ 5 %)	0 (FDR $\leq$ 5 %)
	MHC antigen processing, Adaptive Immune System	
	4 (FDR $\leq$ 10 %)	32 (FDR $\leq$ 10 %)
	RNA Polymerase, mRNA Capping	mRNA Splicing, Spliceosome, mRNA Processing
GO terms	22	51
(FDR $\leq$ 5 %)	BP: 7 CC: 10 MF: 5	BP: 15 CC: 33 MF: 3
	Metabolic process, Intracellular, Cytoplasm, Ligase activity	Intracellular, Organelle, Metabolic process, Ribosome

GO, gene ontology; BP, biological process; CC, cellular component; MF, molecular function.

knockout condition. To determine the number of genes with an altered splicing pattern in the absence of Dpf3, isoform proportion estimation was conducted with the mixture-of-isoforms (MISO) model (Katz et al. 2010) (see chapter 2.11.1. In the left and right ventricle of Dpf3 knockout mice compared to wild type animals, $\sim$ 35 % of the genes with differentially expressed transcripts show an altered isoform distribution. In the skeletal muscle samples, 17 % of genes with differentially expressed isoforms show a shift in isoform proportions and in the data sets from siRNA knockdown of Dpf3a and transfections with a scrambled control siRNA in HL-1 cells, 25 % of the genes with differentially expressed transcripts show an altered isoform distribution. The total numbers of genes with isoform proportion shifts are listed in (Table 3.5).

Overrepresentation analyses were performed on the lists of genes with isoform proportion shifts in the Dpf3 knockout or knockdown condition compared to controls. Overrepresented pathways and GO terms include general terms such as "signaling", "mRNA processing" or "metabolic process" (Table 3.5). The overlap with public data sets comprising tissue specific genes (cardiac genes from the Cardiovascular Gene Annotation Initiative in collabo-

Table 3.6: Overlap of public data sets with genes with isoform proportion shifts in the absence of Dpf3.

	siDpf3 vs. siNon	RV_KO vs. RV_WT	LV_KO vs. LV_WT	SkM_KO vs. SkM_WT
258 splicing factors[a]	7*	6*	5	3
4083 cardiac-related genes[b]	32	43*	59*	20
347 skeletal muscle genes[c]	5	6	9*	5*
609 muscle-related genes[d]	6	5	12*	6*

P values are based on hypergeometric testing; * significant P values ($p < 0.05$); [a] Hegele et al. (2012); [b] Cardiovascular Gene Annotation Initiative in collaboration with EMBL-EBI; [c] The Human Protein Atlas, filtered for muscle related GO terms; [d] MGI database, filtered for muscle related GO terms.

ration with EMBL-EBI and muscle related genes from The Human Protein Atlas and MGI database, both filtered for muscle related GO terms) reveals specific matches (Table 3.6): Cardiac related genes are enriched among the genes with isoform proportion shifts in the hearts of Dpf3 knockout mice compared to hearts from wild type animals. A small overlap of skeletal muscle related genes with genes characterized by an altered isoform distribution in the absence of Dpf3 was significant ($p < 5$, hypergeometric testing) for the left ventricle and skeletal muscle samples. As splicing related pathways and GO terms are associated with the genes with isoform proportion shifts, these genes were overlapped with a comprehensive list of splicing factors (Hegele et al. 2012). Genes of the data set from the Dpf3 siRNA knockdown experiment in HL-1 cells and from the right ventricle show a small significant ($p < 5$, hypergeometric testing) overlap.

3.2.2 Characteristics of differential expressed isoforms after knockout and knockdown of Dpf3

Isoform proportion shifts are represented by differences in Ψ (psi, percent spliced in) values between the knockout or knockdown and the control condition. High expression changes of predominantly expressed transcripts are reflected in high $\Delta\Psi$ values whereas expression changes in minor transcripts result in low $\Delta\Psi$ values (Figure 3.16). To assess the isoform proportion shifts caused by the loss of Dpf3, the size distribution of $\Delta\Psi$ values for each knockout or knockdown to control comparison pair was plotted (Figure 3.17). The majority of $\Delta\Psi$ values in all data sets is below 0.35 meaning that in many cases not the predominantly expressed isoform abundance changed but the abundance of minor isoforms.

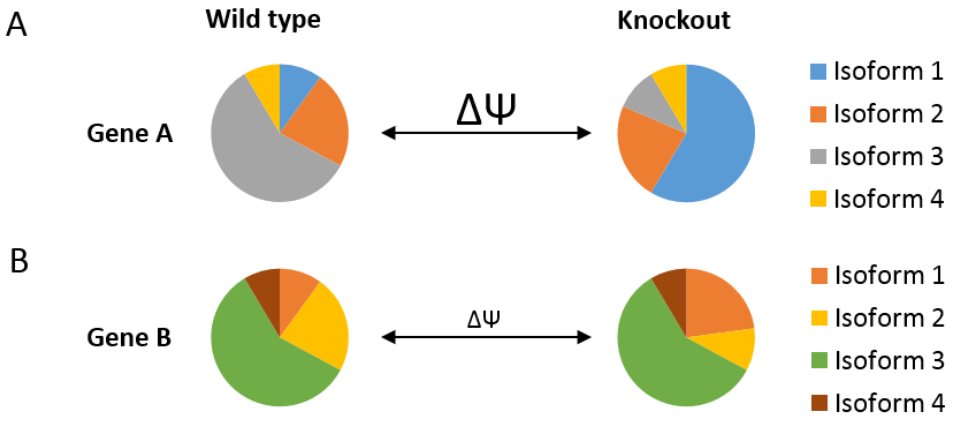

Figure 3.16: Proportion shifts of major and minor expressed isoforms. **A** Expression changes of the predominantly expressed isoform in the wild type compared to the knockout condition results in large changes of the isoform distribution that is represented by high $\Delta\Psi$ (psi, percent spliced in) values. **B** Expression changes of minor expressed transcripts in the wild type compared to the knockout condition results in small changes of the isoform distribution, represented by small $\Delta\Psi$ values.

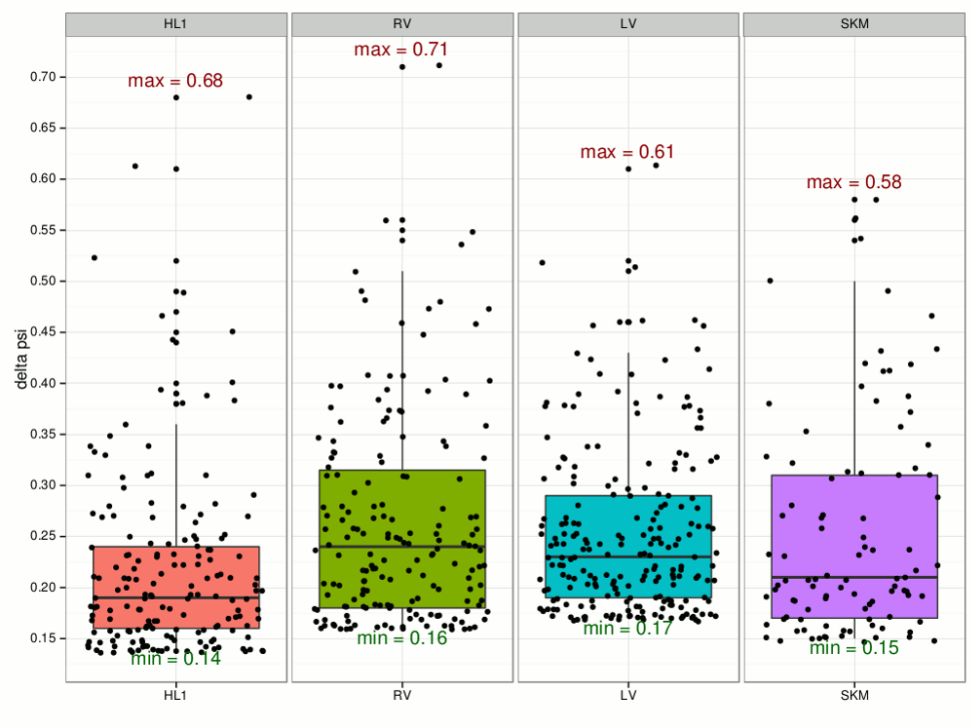

Figure 3.17: Distribution of $\Delta\Psi$ values. Isoform proportion shifts are calculated for Dpf3 siRNA knockdown in HL-1 cells compared to control transfections (HL1) and indicated tissue samples from Dpf3$^{-/-}$ mice and wild type littermates; RV, right ventricle; LV, left ventricle; SKM, skeletal muscle.

3.2.3 Conclusion

The loss of Dpf3 in Dpf3$^{-/-}$ mice and upon siRNA knockdown in HL-1 cells results in up to $\sim$ 750 differentially expressed transcripts assigned to $\sim$ 680 genes. The transcripts of 17 % (siRNA knockdown sample), 25 % (skeletal muscle sample) and 35 % (left and right ventricle samples) of these genes show an altered isoform distibution, mainly represented by $\Delta\Psi$ values in the low to moderate range.

3.3 The interaction of DPF3 with the spliceosome

DPF3 may influence the splicing outcome in three potential ways (see chapter 1.4). First, DPF3 may act as an adapter molecule that links the histone code functionally with splice site selection. Second, the splice site selection is affected by the elongation rate of Pol II, which is modulated by the activity of chromatin remodeling complexes. Hereby, DPF3 may influence the Pol II elongation rate by recruiting the BAF chromatin remodeling complex. Third, the accessibility of splicing enhancer and/or silencer sequences is influenced by DPF3. Experimental testing of the first hypothesis will be described in the following.

3.3.1 Yeast two-hybrid screen using preys from a human fetal brain library

In 2003, a genome-wide array analysis of normal and malformed human hearts had revealed a set of interesting novel cardiac expressed genes including Dpf3a (Kaynak et al. 2003). This gene set was tested in a yeast two-hybrid (Y2H) screen against a human fetal brain library (Goehler et al. 2004) revealing an interaction of DPF3a with the splicing factor LUC7L2 (Martin Lange, unpublished data).

Validation of the DPF3 - LUC7L2 interaction

To validate the interaction between LUC7L2 and DPF3a, both proteins were expressed as GST- and Flag-tag fusion proteins. Subsequently, binding between purified recombinant GST fusion proteins from *E. coli* cultures and Flag-tagged proteins from HEK293T whole cell lysates were tested in GST pulldown assays. For the sake of completeness, DPF3b fusion proteins were also included in the pulldown assays.

Both GST-DPF3a and GST-DPF3b were able to pull down Flag-tagged LUC7L2, while the reverse experiment with changed tags was negative (Figure 3.18).

As posttranslational modifications and protein folding machineries differ between prokaryotes and eukaryotes (Beltrao et al. 2013; Rosano and Ceccarelli 2014), the interaction between LUC7L2 and DPF3 was further assesed by coimmunoprecipitation. HA- and Flag-tagged fusion proteins were overexpressed in HEK293T cells. Neither Flag-LUC7L2 nor HA-LUC7L2 was able to precipitate HA-DPF3a, HA-DPF3b and Flag-DPF3a, Flag-DPF3b, respectively. The reverse experiments, DPF3 constructs coimmunoprecipitate LUC7L2, were negative as well.

3.3.2 Tandem affinity purification followed by mass spectrometry

Besides the Y2H screen in 2003, additional protein-protein interaction data support an interaction of Dpf3 with the spliceosome. TAP-MS in nuclear extracts of HEK293T and C2C12 cells reveal subunits of the BAF chromatin remodeling complex as well as several splicing factors (Table 3.7) (Lange et al. 2008). The significance threshold is passed by a Mascot score greater than 50, a minimum of two matcing MS/MS spectra and if they had not been identified in the control sample nor were they part of common background tables (Gingras et al. 2005; G. I. Chen and Gingras 2007; Lange et al. 2008). The Mascot score reflects the probability that the experimentally determined peptide mass matches with the reference peptide mass and that the match is not a random event. Mascot scores for splicing factors do not exceed 255 whereas the vast majority of BAF complex subunits reach Mascot scores of several hundred up to 2413. The nine splicing factors in the C2C12 cell sample and the three splicing factors in the HEK293T cell sample interact with Dpf3b (Table 3.7).

3.3.3 Yeast two-hybrid screen using a spliceosomal prey matrix

To further investigate direct protein-protein interactions of both Dpf3 isoforms with a focus on splicing, several DPF3 constructs were tested against a spliceosomal prey matrix in a Y2H screen. The spliceosomal prey matrix contains 237 out of 244 known human splicing factors represented by 442 clones (Hegele et al. 2012).

Generation of DPF3 baits

Bait constructs include four DPF3 full length proteins (Figure 3.19) of which DPF3a_S348A is not phosphorylated at the serine at position 348 while DPF3a_S348D carries a constitutive phosphorylation. As other protein-protein interactions of Dpf3a with the family of HEY repressors depend on the phosphorylation status of the serine at position 348 (H. Cui et al.

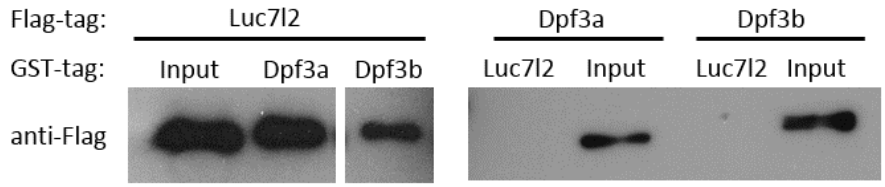

Figure 3.18: GST-pulldown assays with DPF3 and LUC7L2 fusion proteins. Recombinant GST-tagged proteins were immobilized on glutathione-sepharose beads and incubated with HEK293T cell lysates overexpressing the Flag-tagged protein. Bound proteins are detected by immunoblotting using anti-Flag (M2) (Invitrogen). Input: 1 % HEK293T lysate overexpressing the Flag tagged protein.

Table 3.7: Interaction partners of DPF3a and DPF3b identified by a combination of tandem affinity purification and mass spectrometry.

Cell line	Spliceosome	Mascot Score	BAF complex	Mascot Score
C2C12	Ddx17	236	Baf53	54[b]
	Ddx41	98	Baf57	486, 275
	Ilf3	50	Baf60a	261
	Prpf4b	58	Baf60b	242, 393
	Sfrs1	100	Baf60c	600, 263[a]
	Sfrs2	103	Baf170	1573, 804
	Srrm1	154	Baf250a	2413, 1930
	Srrm2	255	Baf250b	1061, 571
	U2af2	152	Brg1	1862, 1202
			Dpf3	708, 379
			Snf5	108, 54
HEK293T	ASPA8	69	Beta-Actin	697, 1461
	DDX5	94	Baf53	826, 699
	MATR3	181	Baf57	982, 969
			BAG60a	80, 1062
			Baf60b	846[a]
			BAG60c	644, 616
			BAF155	2401, 1511
			Baf170	2160[a]
			Baf250a	1844[a]
			Baf250b	1171, 457
			Brg1	2196, 1912
			BRM	959, 792
			Snf5	659, 880

Only Dpf3b interacts with the spliceosome. If not indicated otherwise, both isoforms interact with the BAF complex (Mascot scores refer to Dpf3a, Dpfb); [a] interaction with Dpf3a; [b] interaction with Dpf3b.

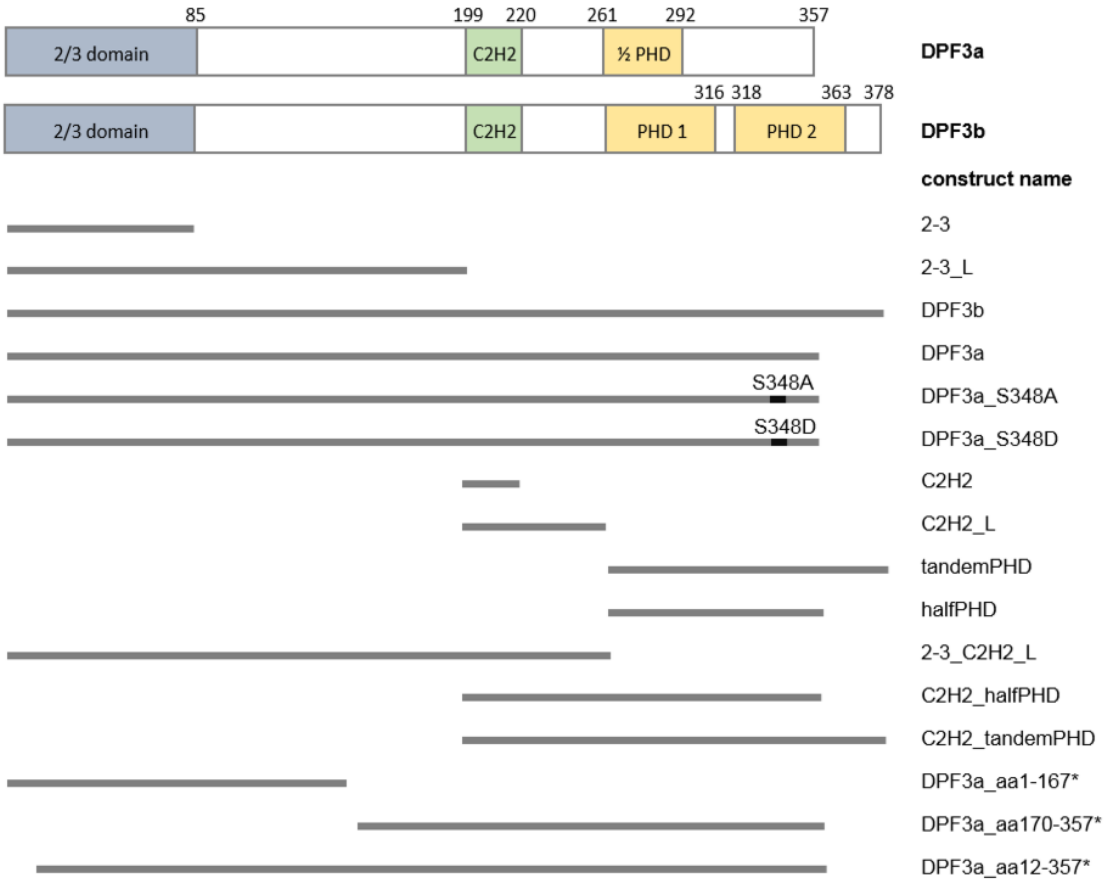

Figure 3.19: Human DPF3 baits. Constructs are represented by gray bars, individual start and endpoints are matching with the domain borders depicted in the schematic representation of DPF3a and DPF3b above. L, linker region between functional domains; aa, amino acid; * constructs used in the Y2H experiment described in 3.3.1.

2015), these constructs were included in the assay setup. Additionally, nine domain constructs and three DPF3a constructs from a former Y2H screen (see section 3.3.1) were used (Figure 3.19). The DPF3a_aa12-357 and the DPF3a_aa170-357 constructs were expressed from the pBTM116 vector and the DPF3a_aa1-167 construct was in the pBTM118c vector yielding N-terminal fusions with a LexA DNA binding domain (Table 3.8) (Martin Lange, unpublished data). The other bait constructs were first cloned into the pDONR221 donor vector and shuttled via Gateway cloning into the vectors pBTM116-D9 and pBTMcC24-DM (Table 3.8). Expression from the pBTM116-D9 vector results in hybrids with N-terminal LexA DNA binding domains whereas the LexA DNA binding domain is C-terminally fused upon expression from the pBTMcC24-DM vector.

Table 3.8: Number of colonies after mating of DPF3 constructs with the spliceosomal prey matrix.

DPF3 construct	Vector	# colonies
Dpf3a	pBTM116-D9	1
	pBTMcC24-DM	1
Dpf3a_aa12-357	pBTM116	19 big colonies
Dpf3a_S348A	pBTM116-D9	0
	pBTMcC24-DM	1
Dpf3a_S348D	pBTM116-D9	0
	pBTMcC24-DM	1
Dpf3b	pBTM116-D9	0
	pBTMcC24-DM	0
2-3	pBTM116-D9	1
	pBTMcC24-DM	0
2-3_L	pBTM116-D9	1
	pBTMcC24-DM	0
C2H2	pBTM116-D9	0
	pBTMcC24-DM	2
C2H2_L	pBTM116-D9	13
	pBTMcC24-DM	3
tandemPHD	pBTM116-D9	autoactive
	pBTMcC24-DM	autoactive
halfPHD	pBTM116-D9	3
	pBTMcC24-DM	autoactive
2-3_C2H2_L	pBTM116-D9	0
	pBTMcC24-DM	0
C2H2_halfPHD	pBTM116-D9	8
	pBTMcC24-DM	autoactive
C2H2_tandemPHD	pBTM116-D9	50
	pBTMcC24-DM	6 big colonies
Dpf3a_aa1-167	pBTM118c	0
Dpf3a_aa170-357	pBTM116	5

Big colonies: Only prominent colonies were counted on plates with excessive colony growth.

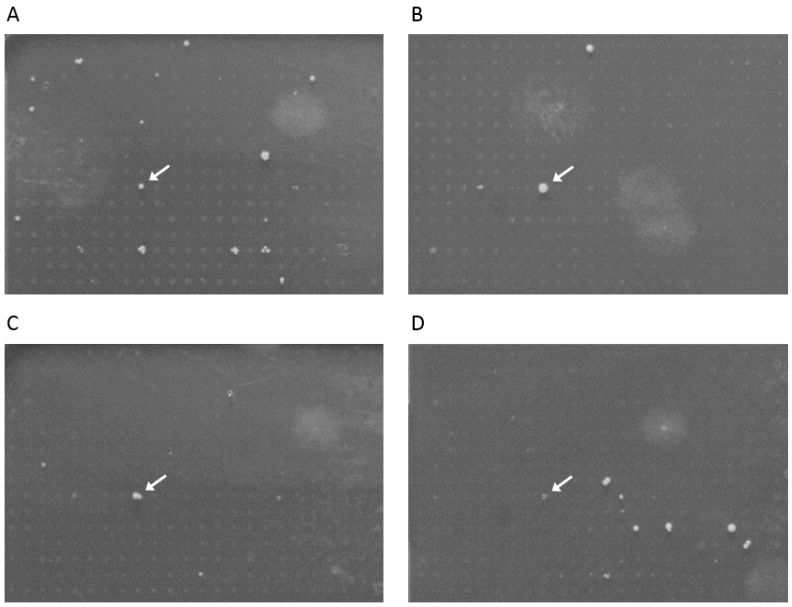

Figure 3.20: Colony growth at day 4 on selective agar plates. Arrows mark colony growth upon an interaction of DPF3 constructs with SR140. **A** C2H2_tandemPHD in pBTM116-D9; **B** C2H2_tandemPHD in pBTMcC24-DM; **C** Dpf3a_aa170-357 in pBTM116; **D** Dpf3a_aa12-357 in pBTM116.

Mating of DPF3 baits with spliceosomal preys

L40c MATa yeast strains were transformed with the bait vectors and mated with the prey matrix in L40ccα MATα strains in a 384 array format. Interacting bait-prey pairs were detected by growth on selective agar plates (Figure 3.20). The number of identified colonies for each DPF3 construct is summarized in Table 3.8. Bait truncation constructs including the tandem PHD finger or the half PHD finger were autoactive or showed excessive colony growth. If possible, prominent colonies were counted. Otherwise, these baits were excluded from further analyses. The full-length and N-terminal constructs showed no or one colony whereas a few colonies were detected for the C2H2 domain extended by the linker region or in combination with the C-terminal ends. The DPF3a construct starting from amino acid 12 yielded 19 big colonies, while various small colonies were not counted.

In total, the positions of colony growth are assigned to 15 splicing factors (Table 3.9). More than one DPF3 construct interacts with the respective splicing factor in nine cases. Typically, two or three out of 25 constructs with evaluable colony growth were found to interact with one splicing factor. Of note, SR140 interacts with six constructs including the C2H2 zinc finger as single domain, the C2H2 domain extended towards the C-terminus and the Dpf3a construct starting from amino acid 12. The overlapping domains of the

DPF3 constructs are considered as putative binding domains. Except of the N-terminally mediated interaction between DPF3a and CBP80, all bait-prey interactions seem to rely on the presence of the C2H2 zinc finger domain. In total, the assay setup comprised 19 Dpf3 constructs that carried a C2H2 zinc finger domain and did not show autoactive colony growth. Consequently, 13 to 16 constructs with a C2H2 domain did not interact with the 15 splicing factors.

The vast majority of splicing factors are represented by one or two full length clones in the prey matrix whereas larger proteins such as hBRR2 (200 kDa) were divided into multiple fragments (Hegele et al. 2012). Additionally, some splicing factors were present in multiple copies. Thus, the number of detected colonies exceeds the number of prey clones for interactions with FAM50B, hPRP31, SF3b145 and SKIP (Table 3.9).

The first 12 bait-prey pairs in Table 3.9 are based on strong conlony growth of at least one bait-prey pair. Interactions with weak colony growth were only included if the DPF3-splicing factor interaction was already supported by other constructs with strong colony growth (C2H2_L-RED interaction and C2H2_tandemPHD-hPRP31 interaction) or if the interaction was supported by other experiments. NFAR (*ILF3*) and RBM39 were coprecipitated by DPF3b in the TAP-MS experiment (see section 3.3.2) and SNRPF interacted with DPF3a in a SILAC (stable isotope labeling with amino acids in cell culture) experiment aiming to identify specific interaction partners of phosphorylated and non-phosphorylated DPF3a (Huanhuan Cui, unpublished data).

The spliceosome is a highly dynamic protein machinery that undergoes several structural rearrangements during splicing (see 1.3.4). A comprehensive list of human splicing factors and their assignment to specific spliceosomal subcomplexes can be found in Hegele et al. (2012). Unexpectedly, the DPF3 constructs interact with splicing factors of not only one but 11 spliceosomal subgroups ranging from early spliceosomal complexes (A and B complex) to late complexes (C complex, Prp19 related factors).

Moreover, the splicing factors are grouped as core spliceosomal components and non-core subunits. The core splicing factors are further divided into proteins that are conserved between *S. cerevisiae* and humans and spliceosomal components that are specific for the human spliceosome (Hegele et al. 2012). As alternative splicing has not been described in *S. cerevisiae*, core splicing factors that are conserved between yeast and human are associated with constitutive splicing (Ast 2004). hBRR2, CBP80, SF3b14b, SF3b130, SF3b145, hPRP31, SKIP and SNRPF fall into this category. Non-core splicing factors and spliceosomal proteins that are specific for humans are involved in alternative splicing and/or have regulatory functions. Three non-core splicing factors (hLUC7, NFAR, RBM39) and four human specific splicing factors (FAM50B, RED, SR140, U2AF35) interact with Dpf3 constructs.

Table 3.9: Protein-protein interactions between DPF3 constructs and splicing factors detected by a Y2H screen.

DPF3 construct (bait)	Putative binding domain	Prey-Symbol (Name)	# Prey clones	# Known PPIs	Category (Group)
4x C2H2_tandemPHD_116 3x DPF3a_aa12-357_116	C2H2_L	SNRNP200 (hBRR2)	10	4	core YC (U5)
1x C2H2_L_116 1x C2H2_halfPHD_116 3x C2H2_tandemPHD_116	C2H2_L	FAM50B (FAM50B)	1	0	core HA (C)
2x C2H2_L_116* 2x C2H2_halfPHD_116 2x C2H2_tandemPHD_116	C2H2_L	IK (RED)	2	17	core HA (B)
1x DPF3a_aa12-357_116	Dpf3a full length	LUC7L ^{Y} (hLuc7)	1	3	Non-core (A)
1x 2-3_L_116 1x DPF3a_24	N-terminus	NCBP1 (CBP80)	2	2	core YC (mRNA)
1x DPF3a_aa12-357_116	Dpf3a full length	PHF5A^{Tb} (SF3b14b)	3	1	core YC (U2)
5x C2H2_tandemPHD_116* 4x C2H2_tandemPHD_24 5x DPF3a_aa12-357_116	C2H2_L with C-terminus	PRPF31 (hPRP31)	2	6	core YC (U4/U6)
7x C2H2_L_116 8x C2H2_tandemPHD_116	C2H2_L	SF3B2 (SF3b145)	3	22	core YC (U2)
3x C2H2_tandemPHD_116	C2H2_L with tandem PHD	SF3B3 (SF3b130)	5	4	core YC (U2)
1x C2H2_L_116 1x C2H2_halfPHD_116 4x C2H2_tandemPHD_116	C2H2_L	SNW1 (SKIP)	2	9	core YC (Prp19rel)
1x C2H2_24 1x C2H2_L_24 1x C2H2_tandemPHD_116 1x C2H2_tandemPHD_24 1x DPF3a_aa170-357_116 1x DPF3a_aa12-357_116	C2H2	U2SURP (SR140)	2	7	core HA (U2rel)
1x DPF3a_S348A_24 1x DPF3a_S348D_24 1x DPF3a_aa12-357_116	Dpf3a full length	U2AF1 (U2AF35)	2	20	core HA (U2rel)
2x C2H2_tandemPHD_116*	C2H2_L with tandem PHD	ILF3^{Tb} (NFAR)	3	8	Non-core (MISC)
1x C2H2_tandemPHD_116*	C2H2_L with tandem PHD	RBM39^{Tb} (RBM39)	2	16	Non-core (A)
1x C2H2_L_24*	C2H2_L	SNRPF^{Sa} (F)	1	11	core YC (Sm)

Legend to Table 3.9

* weak colony growth; ^{Y} PPI supported by a Y2H screen with the ortholog LUC7L2 (see 3.3.1); ^{Tb} PPI supported by TAP-MS (Dpf3b specific); ^{Sa} PPI supported by a SILAC experiment (DPF3a specific); YC (yeast core) splicing factors that are conserved between *S. cerevisiae* and human; HA (human addition) splicing factors that are specific for the human spliceosome; bait expression vectors are indicated by _116 (pBTM116 vectors) and _24 (pBTMcC24-DM).

3.3.4 Validation by LUMIER assays

A maximum of six out of 19 C2H2 zinc finger containing Dpf3 constructs with evaluable colony gwroth showed an interaction with splicing factors in the Y2H screen. To determine if these interactions are sound or false positive, LUMIER assays as another protein-protein inteaction method were performed. Splice site selection occurs during early steps of splicing (see chapter 1.3.4 and chapter 1.3.5). Therefore, early acting regulatory splicing factors from Table 3.9 were choosen for validation by LUMIER assays.

A LUMIER assay is a coimmunoprecipitaion with a luminescence based readout (Barrios-Rodiles et al. 2005), here applied in a 96 well format. After coexpression of PA- and firefly-tagged fusion proteins in HEK293 T-Rex cells, PA-tagged proteins are immobilized on the bottom of IgG coated 96 wells and the firefly-tagged interaction partners are detected by a luciferase assay. Log_2-fold changes and z-scores were calculated from luciferase activities of the protein pair and background binding. Log_2-fold changes larger than one with z-scores larger than 2 were considered positive.

Eight DPF3 constructs (C2H2, C2H2_L, C2H2_halfPHD, C2H2_tandemPHD, DPF3a, DPF3b, DPF3a_aa12-357, DPF3a_aa170-357) were shuttled into the vectors pcDNA3.1V5-Fire and pcDNA3.1PA-D57. Expression from the pcDNA3.1V5-Fire vector results in firefly-tagged fusion proteins and expression from the pcDNA3.1PA-D57 vector yields PA-tagged hybrids. The splicing factors SR140, IK (RED) and LUC7L were available as Firefly- and PA-tagged hybrids from the Stelzl lab. RBM39 was shuttled into the respective destination vectors. To determine the background fluorescence intensity, several PA-tagged proteins were included into the assay setups (APPL2, BAT3, GPKOW, PPARA, QKI, SPATA24 and U2AF1). Firefly-tagged hPRP2 (DHX16) and PA-tagged GPKOW (Hegele et al. 2012) or Fire-SMU1/PA-IK, Fire-RBM10/PA-SR140 and Fire-LUC7L/PA-LUC7L served as positive controls in each setup. A detailed overview of the experimental setups is given in Table 2.12 in chapter 2.10.4.

Under normal assay conditions (cell lysis with HEPES buffer and washing with PBS), all assays with PA-tagged DPF3 constructs and firefly-tagged splicing factors were negative. Exemplary results are shown in Figure 3.21 A-D. Each pair was tested two to three times in independent assays. Reverse experiments with PA-tagged splicing factors and firefly-tagged

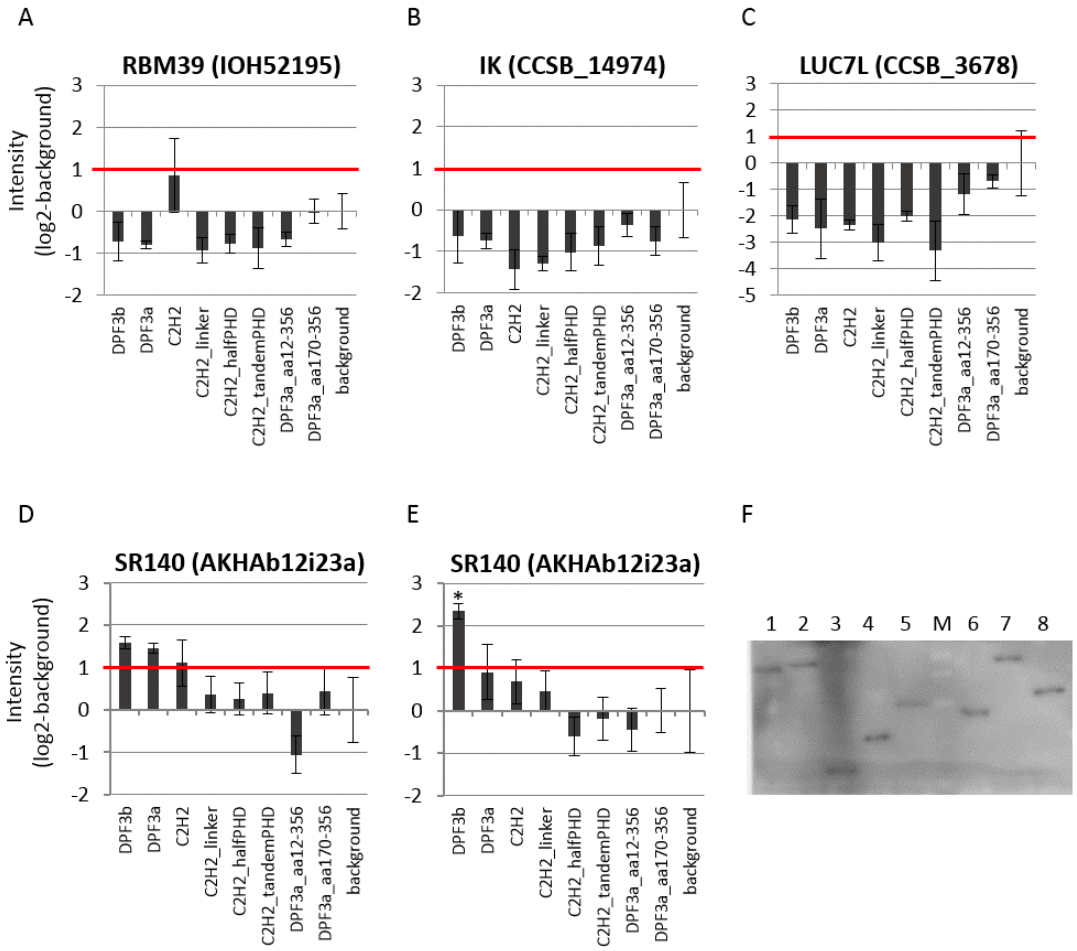

Figure 3.21: Validation of Y2H PPIs by LUMIER assays. Log_2-fold changes larger than one with z-cores larger than 2 were considered positive. **A-D** LUMIER assays with PA-tagged DPF3 constructs and firefly-tagged splicing factors as indicated, standard assay conditions (cell lysis with HEPES buffer, washing with PBS). **E** LUMIER assay with PA-tagged DPF3 constructs and firefly-tagged SR140, modified assay conditions (cell lysis with HEPES buffer, washing with high salt PBS). **F** Western blot with 20 % whole cell lysate, immunodetection of the PA-tag, 1: PA-DPF3b, 78 kDa; 2: PA-DPF3a, 78 kDa; 3: PA-C2H2, 38 kDa; 4: PA-C2H2_L, 43kDa; 5: PA-C2H2_halfPHD, 55 kDa; 6: PA-C2H2_tandemPHD, 55 kDa; 7: DPF3a_aa12-357, 78 kDa; 8: DPF3a_aa170-357, 56 kDa; M: PageRuler Plus Prestained Protein Ladder (Thermo Scientific), reference bands from top to bottom mark 100 kDa, 70 kDa, 55 kDa, 35 kDa.

DPF3 constructs were repeatedly negative as well. Western blot analysis of PA-tagged proteins after each assay (Figure 3.21 F) and measuring the firefly activity of 5 % whole cell lysate excluded negative results due to failed overexpression. The signal intensities of the positive controls were as expected.

With the exception of assays including SR140, the raw signals with a maximum of approximately 8000 were very low. Under normal assay conditions, the raw signals for SR140-DPF3 construct interactions reached a maximum of approximately 50000. However, the background signals were high as well. To reduce the background binding, other combinations of cell lysis and washing buffers were tested. RIPA buffer in combination with PBS washing or washing with 0.05 % Tween/PBS as well as 1 % BSA/HEPES lysis buffer and PBS washing did not improve the LUMIER assay. Cell lysis with HEPES buffer in combination with a high salt PBS washing buffer reduced the background binding and the DP3b-SR140 interaction increased to 4-fold with a z-score of 3.3 (Figure 3.21 E).

3.3.5 Conclusion

The protein-protein interactions of Dpf3 and splicing factors analyzed by different methods yield contradicting results or do barely overlap. The interaction of LUC7L2 with Dpf3a is positive in the Y2H screen with a fetal brain library, positive if Luc7l2 pulls down Dpf3a but negative when the pull-down tags are changed. Coimmunoprecipitation of Luc7l2 and Dpf3 in both directions is negative as well. The Y2H screen testing DPF3 constructs against a spliceosomal prey matrix resulted in 15 DPF3-splicing factor pairs. Four pairs comprising early acting splicing factors were selected for further validation by LUMIER assays and were negative except of the interaction between DPF3b and SR140. However, this protein pair did not result in colony growth in the Y2H screen and five other DPF3 constructs that showed colony growth in the YH2 screen did not pass the significance criteria in the LUMIER assays (Figure 3.22). Consequently, the results from the Y2H screens seem to be false positive results. In addition, the splicing factors detected in TAP-MS experiments in HEK293T cells do not overlap with results from TAP-MS experiments in C2C12 cells or other experiments. Only three splicing factors from the TAP-MS lists (C2C12) were also present in the Y2H lists. However, ILF3 and RBM39 showed weak colony growth and the Mascot scores of RBM39 and SR140 were slightly below the cutoff of 50. Taken together, the data do not support and interaction of DPF3 with the spliceosome.

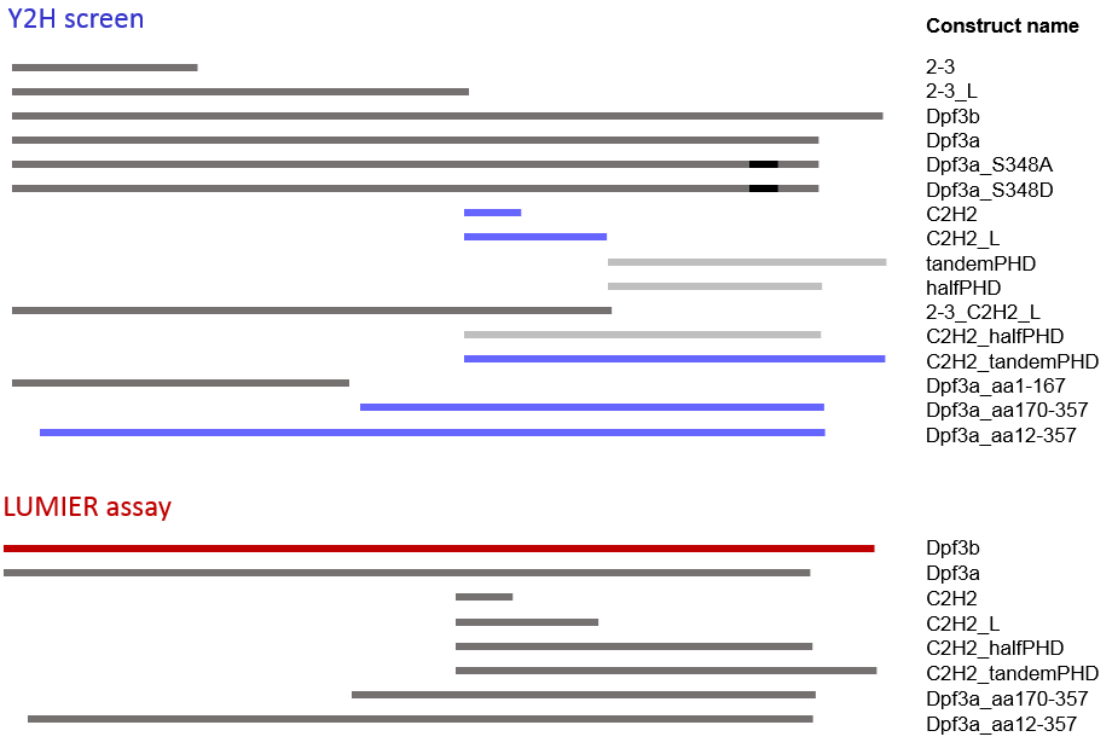

Figure 3.22: Comparison of Dpf3 constructs that interact with Sr140 in LUMIER assays and Y2H screen. Dark gray, tested constructs; light gray, autoactive constructs; blue, constructs with colony growth in the Y2H screen; red, construct interacts with SR140 in the LUMIER assay.

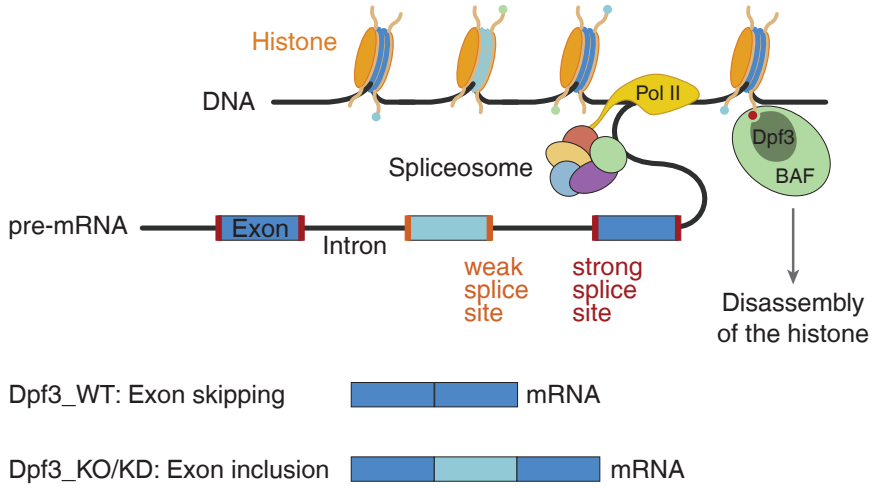

Figure 3.23: Schematic model for the role of Dpf3 in kinetic splicing regulation. In the presence of Dpf3 (Dpf3_WT), the BAF complex is recruited to open the chromatin structure. The fast elongation rate of the RNA polymerase II (PolII) results in exon skipping. In the absence of Dpf3 (Dpf3_KO/KD), histone disassembly is impaired resulting in a slow Pol II elongation rate and exon inclusion.

3.4 The role of Dpf3 in the kinetic splicing model

Although several protein-protein interactions between DPF3 and splicing factors were detected, none of them was significant in more than one method (see section 3.3.5). Therefore, the potential role of DPF3 in the kinetic splicing model was tested. According to this model, the selection of weak and strong splice sites is dependent on the elongation rate of the RNA polymerase II (Naftelberg et al. 2015). Besides other factors, nucleosomes can act as "speed bumps" that slow down the RNA polymerase II (Pol II) (Kornblihtt et al. 2009).

The analyses described below are based on the following (Figure 3.23):

1. Dpf3 recognizes histone methylations and acetylations and the recruitment of the BAF chromatin remodeling complex opens the chromatin structure.

2. Exon skipping of alternative exons with weak splice sites occurs in the absence of histones allowing a fast Pol II elongation rate.

3. Histone disassembly is impaired in the absence of Dpf3 (Kockout or knockdown condition) resulting in a slow Pol II elongation rate and inclusion of alternative exons with weak splice sites.

Table 3.10: Dpf3 dependent exons with strong and weak inclusion scores (see Figure 2.1 in chapter 2.11.1.

	Dpf3 vs siNon	RV_KO vs. RV_WT	LV_KO vs. LV_WT	SkM_KO vs. SkM_WT
Genes with diff. isoform proportions (Transcripts)	171 (863)	175 (881)	218 (1100)	97 (493)
Transcripts (TPM > in siDpf3 or KO) (Exons)	288 (1969)	232 (1609)	317 (2758)	116 (867)
Exons (> 10 % more counts in siDpf3 or KO)	455	773	2059	445
Exons with strong score	209	379	1077	210
Exons with weak score	246	394	980	235

3.4.1 Analysis scheme

The calculation of isoform proportion shifts in differentially expressed transcripts is described in section 3.2.1. Heart (left and right ventricle) and skeletal muscle samples from Dpf3$^{-/-}$ mice were compared with samples from wild type littermates. Samples from Dpf3 siRNA knockdown experiments in HL-1 cells were compared with HL-1 cells that were transfected with a scrambled control siRNA. These transcripts were filtered for TPM values larger than one in the knockout or knockdown condition and exons with more than 10 % counts compared to controls (Figure 2.1 in chapter 2.11.1). Subsequently, the exons were divided into exons with strong and weak inclusion scores (Shepard et al. 2011). Finally, the exons were overlapped with binding sites of histone modifications that are recognized by Dpf3 as well as binding sites of Brg1.

3.4.2 Dpf3 dependent exons with weak inclusion scores

The number of exons with TPM values larger than one in the knockout or knockdown condition and more than 10 % counts compared to controls ranges from several hundred to more than 2000. 455, 773, 2059 and 445 exons match the filtering criteria for the siRNA knockdown, right ventricle, left ventricle and skeletal muscle samples, respectively. The number of exons with strong and weak inclusions scores is balanced in each data set (Table 3.10).

3.4.3 Overlap of Dpf3 dependent exons with binding sites of histone modifications and the BAF complex

To overlap the positions of included exons characterized by weak inclusion scores with binding sites of histone modifications and BAF chromatin remodeling subunits, publicly available data sets (Table 3.11) and experimentally determined binding sites were used.

ChIPseq in HL-1 cells was performed for the histone modifications H3K4me1 and H4K16ac. 55658 peaks were called for H3K4me1 and 10910 peaks were called for H4K16ac using MACS (version 1.4.2) with a p-value cutoff of 0.0001. Selected binding sites were confirmed by qPCR (Figure 9.2 in the appendix 9.2).

Exons with weak and strong inclusion scores that are expressed in the Dpf3 siRNA knockdown condition and that are characterized by at least 10 % more read counts compared to the control sample, overlap with H3K4me1, H3K4me2, H3K14ac, H3K9ac and H4K16ac binding sites. Binding sites of histone modification are from HL-1 cells, mouse embryonic stem cells, mouse embryos (E14) and adult mouse hearts. In total, 109 exons with weak inclusions scores and 49 exons with strong inclusion scores are related to histone modification binding sites (Table 3.11).

Exons in the heart samples from the Dpf3 $^{-/-}$ strain that are characterized by the criteria described above, overlap with H3K4me1, H3K4me2, H3K14ac and H3K9ac binding sites detected in cardiomyocytes, mouse embryonic stem cells, mouse embryos (E14) and adult mouse hearts. 394 and 181 exons with weak inclusions scores and 273 and 107 exons with strong inclusion scores are associated with histone modifications in the left and right ventricle, respectively (Table 3.11).

For the skeletal muscle data set, 89 filtered exons (see above) with weak inclusion scores and 62 exons with strong inclusion scores are associated with H3K4me1, H3K4me2, H3K14ac, H3K9ac and H4K12ac binding sites (Table 3.11). Reference data sets for histone modification binding sites are from C2C12 myotubes, mouse embryonic limbs (E11.5), mouse embryonic stem cells and mouse embryos (E14).

The number of exons associated with histone modification binding sites does not exceed approximately one third (HL-1 cells and right ventricle) or one quarter (left ventricle and skeletal muscle) of all exons matching the filter criteria described above. However, significantly more exons characterized by weak splice sites are associated with histone modification binding sites compared to exons with strong inclusion scores (Table 3.11).

Subsequently, the exons associated with histone modification binding sites were overlapped with binding sites of Brg1 as a representative subunit of the BAF chromatin remodeling

Table 3.11: Histone modifications at Dpf3 dependent exons.

Modification	Tissue	# peaks	caller	all exons	weak ss	strong ss
					HL-1	
H3K4me1	HL-1	55658 [a]	MACS 1.4	472/1969 (24%)	74/246 (30%)	38/209 (18%)
	cardio-myocytes	40900 [b]	Poisson model	81/1969 (4%)	15/246 (6%)	5/209 (3%)
H3K4me2	ESC	32254 [c]	MACS	210/1969 (11%)	40/246 (16%)	7/209 (3%)
H3K14ac	E14 embryo	29669 [d]	MACS	101/1969 (5%)	19/246 (8%)	4/209 (2%)
H3K9ac	adult heart (8wks)	29915 [e]	MACS	381/1969 (19%)	67/246 (27%)	15/209 (7%)
	E14 embryo	58563 [f]	MACS	469/1969 (24%)	83/246 (34%)	22/209 (10.5%)
H4K16ac	HL-1	10910 [g]	MACS 1.4	226/1969 (11.5%)	48/246 (19.5%)	14/209 (7%)
					RV	
H3K4me1	adult heart (8wks)	86167 [h]	MACS	341/1609 (21%)	90/394 (23%)	80/379 (21%)
	adult heart	75216 [i]	MACS 1.4	324/1609 (20%)	85/394 (22%)	67/379 (18%)
	cardio-myocytes	40900 [b]	Poisson model	82/1069 (8%)	15/394 (4%)	16/379 (4%)
H3K4me2	ESC	32254 [c]	MACS	130/1609 (8%)	60/394 (15%)	15/379 (4%)
H3K14ac	E14 embryo	29669 [d]	MACS	101/1609 (6%)	42/394 (11%)	13/379 (3%)
H3K9ac	adult heart (8wks)	29915 [e]	MACS	345/1609 (21%)	116/394 (29%)	41/379 (11%)
	E14 embryo	58563 [f]	MACS	343/1609 (21%)	131/394 (33%)	41/379 (11%)
					LV	
H3K4me1	adult heart (8wks)	86167 [h]	MACS	499/2758 (18%)	194/980 (20%)	182/1077 (17%)
	adult heart	75216 [i]	MACS 1.4	477/2758 (17%)	193/980 (20%)	142/1077 (13%)
	cardio-myocytes	40900 [b]	Poisson model	116/2758 (4%)	41/980 (4%)	45/1077 (4%)
H3K4me2	ESC	32254 [c]	MACS	249/2758 (9%)	112/980 (11%)	43/1077 (4%)
H3K14ac	E14 embryo	29669 [d]	MACS	129/2758 (5%)	58/980 (6%)	28/1077 (3%)
H3K9ac	adult heart (8wks)	29915 [e]	MACS	482/2758 (17.5%)	256/980 (26%)	87/1077 (8%)
	E14 embryo	58563 [f]	MACS	537/2758 (19.5%)	249/980 (25%)	105/1077 (10%)

Modification	Tissue	# peaks	caller	all exons	weak ss	strong ss
					SkM	
H3K4me1	C2C12 myotubes	360720 [j]	Qeseq	186/867 (21.5%)	51/235 (22%)	31/210 (15%)
	embryonic limb (E11.5)	58162 [k]	MACS 1.4	111/867 (13%)	34/235 (14.5%)	7/210 (3%)
H3K4me2	ESC	32254 [c]	MACS	98/867 (11%)	28/235 (12%)	14/210 (7%)
	C2C12 myotubes	86502 [l]	Qeseq	113/867 (13%)	34/235 (14.5%)	17/210 (8%)
H3K14ac	E14 embryo	29669 [d]	MACS	39/867 (4.5%)	11/235 (5%)	9/210 (4%)
H3K9ac	E14 embryo	58563 [f]	MACS	182/867 (21%)	51/235 (22%)	27/210 (13%)
	C2C12 myotubes	39523 [m]	Qeseq	34/86 v (4%)	7/235 (3%)	5/210 (2%)
H4K12ac	C2C12 myotubes	70763 [n]	Qeseq	44/867 (5%)	14/235 (6%)	10/210 (5%)

[a] Sperling Lab (sp139); [b] E-GEOD-47949 (GSM1163093); [c] E-GEOD-18515 (GSM461266); [d] E-GEOD-31284 (GSM775314); [e] E-GEOD-31039 (GSM1000149); [f] E-GEOD-31284 (GSM775313); [g] Sperling Lab (sp141); [h] E-GEOD-31039 (GSM769025); [i] E-GEOD-52123 (GSM1260013); [j] E-GEOD-25308 (GSM721289); [k] E-GEOD-37151 (GSM1371052); [l] E-GEOD-25308 (GSM721291); [m] E-GEOD-25308 (GSM721301); [n] E-GEOD-25308 (GSM721305); gray, difference in histone mark occupancy between exons with weak and strong inclusion scores is not significant; ESC, embryonic stem cell; wks; weeks.

Table 3.12: Brg1 binding sites at Dpf3 dependent exons.

	Tissue	weak score	strong score	weak score - 1 kb	weak score + 1 kb	strong score - 1 kb	strong score + 1 kb
HL-1							
Histones	(see Table 3.11)	109	49	108	109	48	48
Brg1	Heart (E11.5)	8/109	3/49	10/108	16/109	3/48	4/48
RV							
Histones	(see Table 3.11)	178	107	168	173	104	103
Brg1	Heart (E11.5)	6/178	1/107	21/168	21/173	10/104	6/103
LV							
Histones	(see Table 3.11)	386	272	370	368	263	267
Brg1	Heart (E11.5)	10/386	4/272	32/370	46/368	13/263	14/267
SkM							
Histones	(see Table 3.11)	86	62	83	83	61	55
Brg1	Limb (E11.5)	8/86	3/62	8/83	8/83	3/61	3/55

Brg1 binding site for the heart (E11.5) are from E-GEOD-37151 (GSM1011085); Brg1 binding sites for the limb (E11.5) are from E-GEOD-37151 (GSM912549).

complex. Less than 10 Brg1 binding sites are associated with the exon subsets (Table 3.12). Extension of the exons one kilobase up- and downstream into the intronic regions does scarcely alter the number of histone modification binding sites. The number of Brg1 binding sites increases to a maximum of nine to 14.5 % (Table 3.12). Nevertheless, these numbers do not support a biologically relevant role of Dpf3 in the kinetic splicing model.

3.4.4 Conclusion

Assuming a role of Dpf3 in the kinetic splicing model with the hypothesis that Dpf3 recruits the BAF chromatin remodeling complex to open the chromatin structure and allowing a fast Pol II elongation rate, would result in the inclusion of alternatively spliced transcripts in the knockout condition and exon skipping in the wild type condition. Although several hundred exons with weak inclusion scores show a more than 10 % higher inclusion rate in the Dpf3 knockout or knockdown condition compared to controls, the positions of the vast majority of these exons are not in the proximity of the BAF complex subunit Brg1. Taken together, these results do not support a relevant function of Dpf3 in the kinetic splicing model with the BAF complex promoting a fast Pol II elongation rate. The contrary assumption, Dpf3 recruits the BAF complex as a barrier for Pol II, was not further tested.

3.5 The interaction of Dpf3 with RNA

Recruitment of splicing factors to splice sites can occur via the C-terminal domain of the RNA polymerase II, adapter molecules, histone modifications or RNA binding proteins such as RBM20, which has been shown to regulate titin splicing (W. Guo et al. 2012). Moreover, it has been shown that the BAF complex subunit Brm is associated with snRNPs in an RNA dependent manner (Tyagi et al. 2009). To elucidate if DPF3 influences the splicing outcome via RNA binding, PAR-CLIP (photoactivatable ribonucleoside-enhanced crosslinking and immunoprecipitation) experiments were performed.

3.5.1 PAR-CLIP pilot experiments in different cell lines

The standard PAR-CLIP protocol (Spitzer et al. 2014) starts with the stable transfection of Flp-In HEK 293 cells with an pFRT/TO/FLAG/HA vector carrying the desired insert (Hafner et al. 2010). Expression is inducible with doxycyclin. Unfortunately, this expression system was not suitable for the expression of Flag/HA-tagged DPF3a and DPF3b. As shown by western blot analysis, the Dpf3 isoforms were expressed but without the Flag-tag

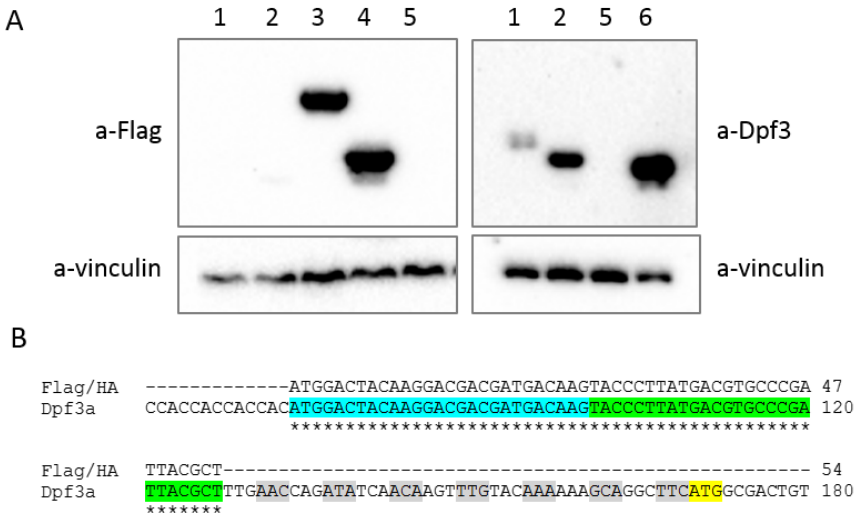

Figure 3.24: pFRT/TO/FLAG/HA-DPF3 vector analysis. A Expression of DPF3a and DPF3b from the pFRT/TA/FLAG/HA vector results in protein expression without the Flag/HA tag. **B** Sequencing of the pFRT/TA/FLAG-DPF3a vector confirms the presence of the Flag (blue) and HA (green) tag, the first start codon is at the beginning of the Flag tag sequence, the start codon of the DpF3a sequence (yellow) is in frame. a-Flag, immunodetection of the Flag tag; a-DPF3, immunodetection of DPF3a and DPF3b; a-vinculin, immunodetection of Vinculin (loading control), 1: Flag/HA-DPF3a (43 kDa); 2: Flag/HA-DPF3b (43 kDa); 3: Flag/HA-METTL16 (63 kDa); 4 Flag/HA-ALKBH5 (44 kDa); 5: mock control; 6: HA-Dpf3b (positive control)

(Figure 3.24 A) that is required for immunoprecipitation in the PAR-CLIP protocol. pFRT/-FLAG/HA-ALKHB5 (expression without doxycyclin induction) and pFRT/TO/FLAG/HA-METTL16 (expression requires doxycylin induction) served as positive controls. Sequencing of the vector shows the Flag and HA tag sequence with a start codon at the beginning of the Flag sequence. The sequence of DPF3a follows in frame (Figure 3.24 B). Similar results were obtained for sequencing of the pFRT/TO/FLAG/HA-DPF3b vector.

To circumvent this expression problem, transient transfection with the vector pTL-FlagC carrying the DPF3a or DFP3b sequence was conducted. As endogenous DPF3 expression is restricted to the heart and skeletal muscle, the skeletal muscle cell line C2C12 was choosen for transfections. To adapt the PAR-CLIP protocol to transient transfections in this cell line, pilot experiments testing transfection and doxycylin conditions as well as lysis buffer conditions were required. 4SU labeling with 400 μM final concentration 12 hours after transfection (Figure 3.25) and cell lysis with a high salt lysis buffer and sonication after additional 12 hours incubation time gave the best results (Figure 3.26). However, the transfection and labeling efficiecies were not sufficent for successful immunoprecipitation.

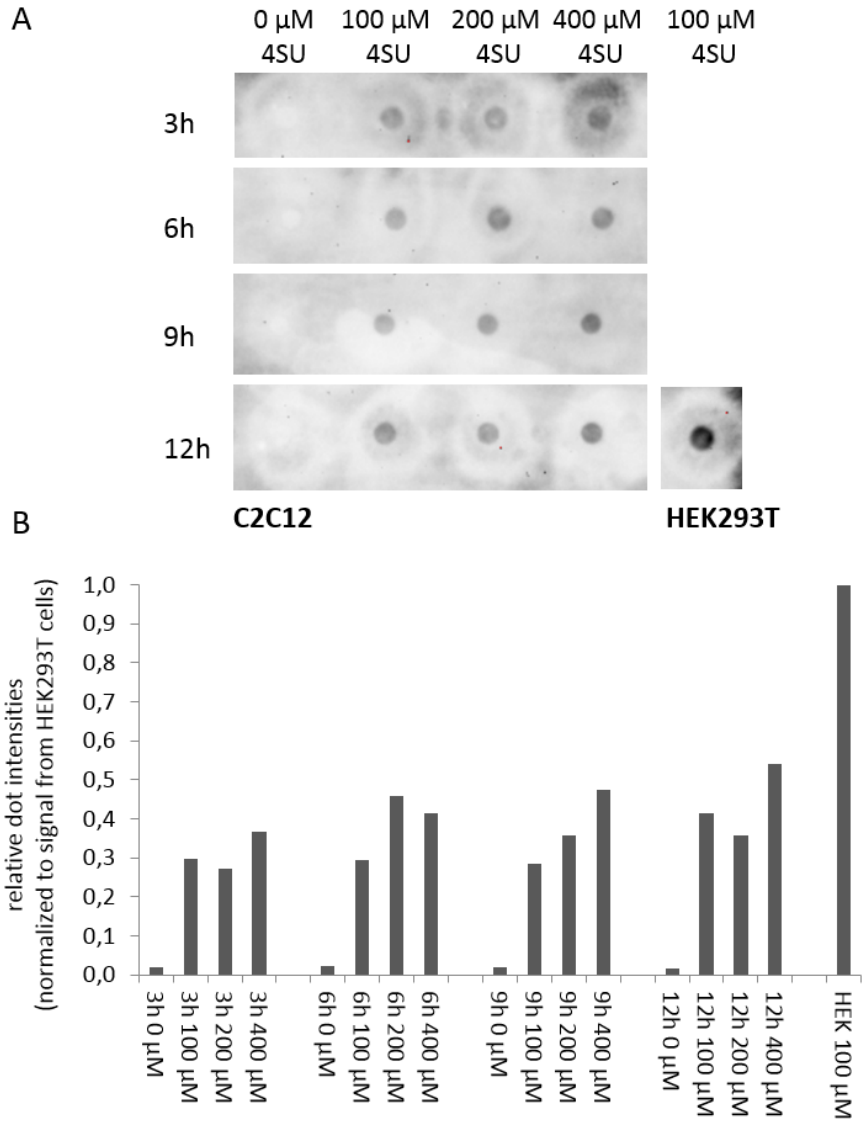

Figure 3.25: 4SU labeling conditions in C2C12 cells. A C2C12 cells were labeled with different 4SU concentrations and incubated as indicated. 2 μg total RNA were used for the dot blot assay. The thiol groups of 4SU were biotinylated, the RNA crosslinked on a Hybond N+ membrane and probed with strepdavidin-HRP conjugated antibodies. **B** Quantification of dot intensities relative to the signal from HEK293T cells.

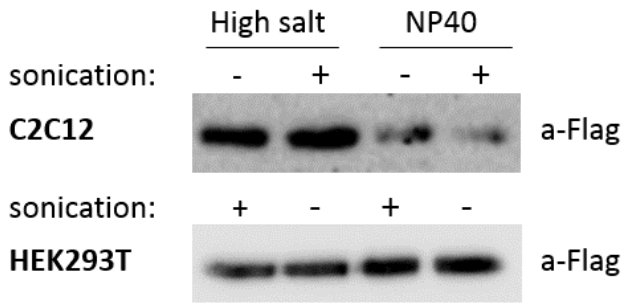

Figure 3.26: PAR-CLIP lysis buffer test in C2C12 and HEK293T cells. Lysis with sonication and high salt lysis buffer is optimal for Flag-Dpf3a extraction from C2C12 cells. For lysis of HEK293T cells, the NP40 lysis buffer is more efficient than the hight salt buffer. a-Flag, immunodetection of the Flag tag of Flag-DPF3a.

Finally, the PAR-CLIP protocol was applied with transient transfections in HEK293T cells using the standard 4SU concentration (100 μM final concentration) and NP40 lysis buffer without sonication (Figure 3.26). In two small scale experiments stopping after SDS-PAGE and autoradiography (Figure 2.2 in chapter 2.11.2), DPF3a was identified as moderate RNA binder whereas DPF3b does not bind to RNA (Figure 3.27).

3.5.2 PAR-CLIP experiments in transiently transfected HEK293T cells

The large scale PAR-CLIP experiment for DPF3a with transiently transfected HEK293T cells that included library preparation, was performed in duplicates. The pooled libraries passed the Bioanalyser check before 1x50 bp single read sequencing on a HiSeq 2000 device. The data were analyzed according to an in-house analysis pipeline developed by Marvin Jens. The conversion statistics for the RNA bound by DPF3a shows the number of collapsed reads mapping to intergenic regions, to transcripts and to decoy sequences (Figure 3.28). The relatively high abundance of decoy sequences indicates a low quality of the sequencing library. However, the data quality was sufficient for a first analysis of nucleotide conversions and a motif search. Due to the 4SU labeling, labeled uridines are transcribed as cytidines during cDNA synthesis. Based on these artificial point mutations, the exact position of DPF3a binding can be determined. Subsequently, the reads characterized by a T:C conversion were analyzed with regard to binding motifs. Overrepresented motifs were not found.

3.5.3 Conclusion

PAR-CLIP experiments in C2C12 and HEK293 cells identified Dpf3a as a moderate RNA binding molecule whereas Dpf3b does not bind to RNA. However, further analysis of the

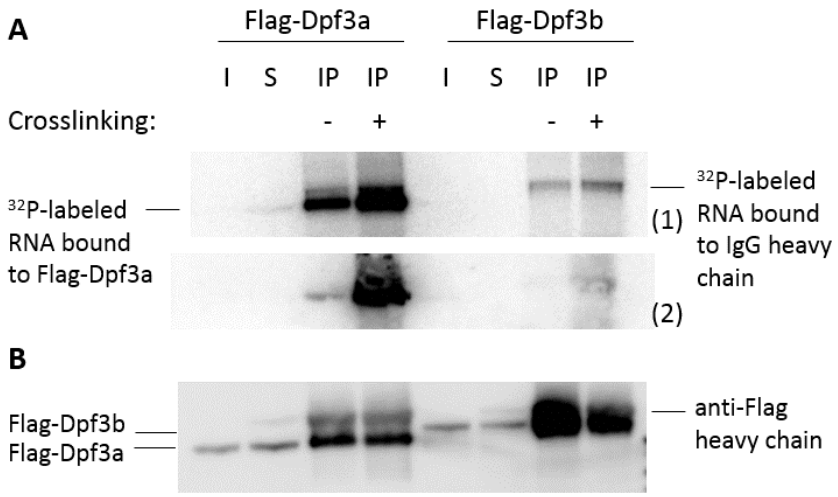

Figure 3.27: PAR-CLIP pilot experiment in HEK293T cells. A Autoradiography shows RNA bound to DPF3a but not to DPF3b; the experiment was performed in independent duplicates (1,2). **B** Immunodetection of the Flag tag at the DPF3 isoforms. The same gel shown in A (1) was used for blotting. I, input; S, supernatant; IP, immunoprecipitation.

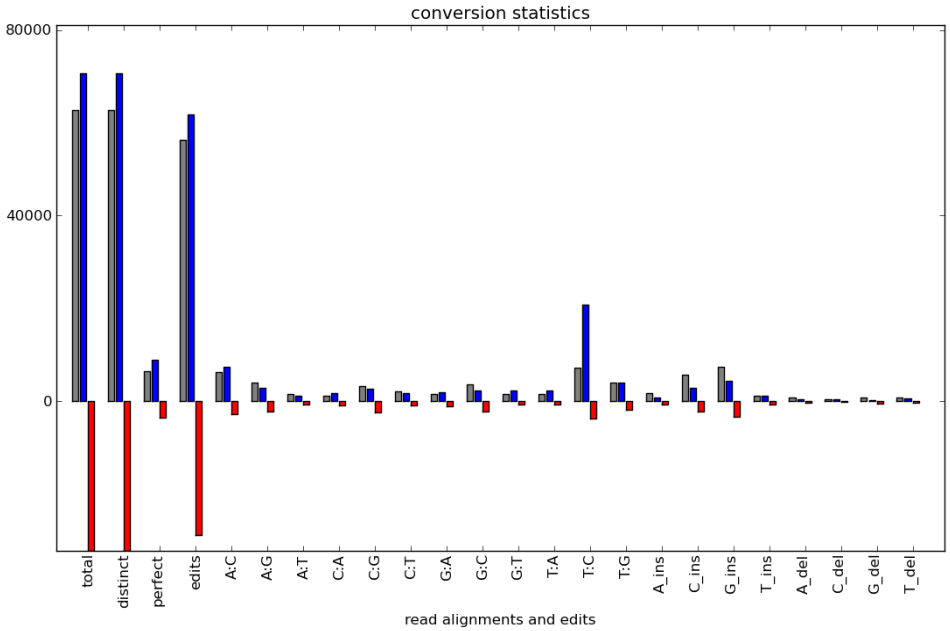

Figure 3.28: Conversion statistics for the DPF3a-RNA interaction. Bars represent the number of collapsed, mapped reads to intronic regions (gray), to the transcriptome (blue) and to decoy sequences (red). "Total" and "distinct" shows the number of all reads, "perfect" refers to reads without mutations and "edits" summarizes the reads with mutations. Point mutations are indicated, for example A:C means adenine to cytosine mutation; A, adenine; C, cytosine; T, thymine; G, guanine; ins, insertion; del, deletion;

RNA bound to Dpf3a did not reveal a binding motif assuming an unspecific interaction with newly synthesized pre-mRNA that is in close proximity to chromatin.

4 Discussion

4.1 The Dpf3 knockout mouse

To expand the knowledge about the functions of Dpf3 beyond cell culture and the zebrafish model, a Dpf3$^{-/-}$ mouse strain was generated using the cre-loxP and Flp/FRT systems. These systems are widely used tools to control tissue- or time-dependent excision of genomic regions (Bouabe and Okkenhaug 2013). The second exon of Dpf3 was targeted with loxP sites and a neomycine cassette flanked by FRT sites for clone selection in the iTL (InGenious Targeting Laboratory) IC1 embryonic stem cell line that is derived from the C57BL/6N strain. For excision of the neomycine cassette and removal of the second exon of Dpf3, Flp and Cmv-cre mice on a C57BL/6 background were choosen to maintain the isogenic status of the genetically modified strain. As cryptic loxP sites occur in the genome with a rate of one site per 1.2 megabase (Schmidt-Supprian and Rajewsky 2007), the mice were mated with wild type C57BL/6J mice to obtain the Cre-free Dpf3$^{-/-}$ strain. The inheritence of the Dpf3$^{-/-}$ allele follows the Mendelian laws and the fertility of 9 ± 2 pups per litter ($n = 23$) in heterozygous matins is comparable to C57BL/6 with 6 to 9 pups per litter (Potgieter and Wilke 1997; Eskola and Kaliste-Korhonen 1999; Blake et al. 2003). The litter size of homozygous matings (6 ± 2 pups per litter) is lower but with five matings monitored, it has to be considered preliminary.

The Cmv-cre mice express the Cre recombinase under control of a human cytomegalovirus minimal promoter in all tissues including germ cells (Schwenk, Baron, and Rajewsky 1995; De Gasperi et al. 2008). Therefore, a loss of the second exon of Dpf3 was expected in all tissues. PCRs on genomic DNA from tail and ear biopsies, qPCRs on cDNA from heart, brain and skeletal muscle samples as well as RNAseq results from heart and skeletal muscle samples confirmed the altered Dpf3 gene sequence. On protein level, an immunostaining of pDpf3a was only achieved by using signal amplification kits. Despite a high backgound staining, several nuclei in the Tibialis anterior from Dpf3$^{+/+}$ seem to be pDpf3a-positive whereas tissue samples from Dpf3$^{-/-}$ mice lack this staining pattern. Nevertheless, additional antibodies should be applied on tissue samples from Dpf3$^{-/-}$ mice and wild type littermates to confirm the specificity of the staining.

The loss of the second exon causes a frame shift and premature stop codon in the Dpf3 transcript. If a premature termination codon is positioned more than 50-55 nucleotides upstream of the last exon-exon junction, the transcript is usually targeted by nonsense-mediated decay (Lykke-Andersen and T. H. Jensen 2015). As the premature stop codon in the altered Dpf3 transcript occurs already in the third exon of the Dpf3$^{-/-}$ mRNA, a degradation of the Dpf3 mRNA by the nonsense-mediated decay mechanism was expected in the knockout mice. Surprisingly, qPCR products of primers targeting downstream exons and RNAseq reads aligning to all exons except of exon 2 were observed. The persistence of the altered Dpf3 transcript in the Dpf3$^{-/-}$ mice might be explained by an escape from NMD. Trcek et al. (2013) showed that approximately one-third of a β-globin transcript with a premature stopcodon had a normal half-life time of more than 12 hours. However, the NMD escape mechanism for these transcripts is unknown (Trcek et al. 2013). In general, the degradation by NMD can be influenced by the incorporation of selenocysteine at an UGA codon (Seyedali and Berry 2014), frame shift inducing miRNA binding (Belew et al. 2014) and programmed ribosomal frame shifting (Dinman 2012). Another explanation for the detection of altered Dpf3 transcripts by qPCR might be the putative occurence of a circular RNA (circRNA). Recently, the circRNA hsa_circ_0102543 from the DPF3 locus has been detected in human cerebellum (Rybak-Wolf et al. 2015).

To assess the impact of Dpf3 on gene expression, RNAseq in heart and skeletal muscle samples from 12 week old Dpf3$^{-/-}$ mice and wild type littermates was performed. In total, $\sim$ 300 to 600 genes show an equal to or more than 1.5-fold up- or downregulation while expressed in at least one condition. Upon the knockdown of Dpf3 in HL-1 cells, 243 genes are differentially expressed. With few exceptions, the changes in gene expression do not exceed a sixfold up- or downregulation. Moreover, the vast majority of genes (more than 75 % in all samples) show only moderate changes in expression (1.5-fold to twofold up- or downregulation) and the the genes with the strongest up- or downregulation upon the depletion of Dpf3 tend to be lowly expressed in wild type mice or HL-1 cells transfected with a scrambled siRNA. Higher expressed genes with a more than twofold up- or downregulation in Dpf3 knockout animals compared to wild type littermates include the co-chaperone and protein trafficking protein Fkbp8, the cytochrome oxidase subunit Cox5b and the putative splicing factor 2310036O22Rik (orgholog to the human splicing factor C19orf43) that are differentially expressed in both heart samples and the HL-1 cell sample. In addition, the highly expressed skeletal muscle α-Actin (Acta1) is upregulated in the left and right ventricle of Dpf3$^{-/-}$ mice whereas the cardiac α-Actin (Actc1) is upregulated in skeletal muscles from knockout animals. The pyruvate dehydrogenase kinase 4 that inhibits aerobic respiration and increases fat metabolism is more than twofold upregulated in all analyzed tissues of Dpf3 knockout mice. As the Dpf3$^{-/-}$ mice do not show an obvious phenotype at the age of

12 weeks, the observed changes in gene expression compared to Dpf3$^{+/+}$ mice seem to be compensated. Promising candidate genes that might explain the skeletal muscle phenotype in aged mice are the actin related protein 3β (Actr3b, FC = 1.6, FPKM (WT) = 2.9) and the cardiac α-actin 1 (Actc1, FC = 2.1, FPKM (WT) = 278) (see below).

As Lessard et al. (2007) describe a switch of BAF chromatin remodeling complex subunits during neural development, the expression level of the PHD finger proteins PHF10, Dpf1 and Dpf2 were analyzed in more detail. In the heart and skeletal muscle samples, the mRNA levels of Dpf2 and Phf10 did not change upon the loss of Dpf3 and the expression of the brain specific BAF complex subunit Dpf1 (Buchman et al. 1992) was not activated in heart or skeletal muscle from Dpf3$^{-/-}$ mice. Although not upregulated on mRNA level, Phf10 and Dpf2 might compensate the loss of Dpf3.

The observed muscle phenotype with centralized myonuclei in some Dpf3$^{-/-}$ mice seems to be age-dependent and restricted to fast-twitch muscles. The animal groups of one year of age showed a normal muscle morphology in the EDL, TA and soleus as assessed by HE and DAPI staining. In contrast, peripherally as well as centrally positioned myonuclei are present in the EDL and TA in animals from the group of 1.5 years old Dpf3$^{-/-}$ mice (Cre positive). In three out of eight mice, the TA and EDL show an altered myonuclei location throughout the whole cross-sectional area. In addition, a myonuclear centralization in small areas was observed in the EDL of two mice. The myonuclei in the soleus of all 1.5 years old animals are located in the periphery of the muscle fibres. The hearts of Dpf3$^{-/-}$ mice were indistiguishable from control hearts at all time points analyzed. In comparison with *dpf3* morpholino knockdowns in zebrafish (Lange et al. 2008), the Dpf3$^{-/-}$ strain shows only a mild phenotype. Lange et al. (2008) observed an altered heart structure resulting in reduced contractility and disrupted somite boundaries in the curved tails of *dpf3* zebrafish morphants. In situ hybridization analysis of the *dpf3* orthologs in zebrafish embryos revealed an expression pattern for *dpf2* that is restricted to the developing brain and spinal cord. Contrary to this, Dpf2 is ubiquitously expressed in the mouse (Gabig, Mantel, et al. 1994). The different expression patterns of Dpf2 in zebrafish and mouse further supports the hypothesis that the loss of Dpf3 in the mouse can be compensated to some extend by Dpf2 whereas in the zebrafish morphants, reduced levels of *dpf3* are not compensated by orthologous proteins.

In general, no abnormal cage activities were observed for Cre-free Dpf3$^{-/-}$ mice and the knockout animals were visually indistinguishable from wild type littermates. Regarding Dpf3$^{-/-}$ mice still expressing the Cre recombinase, some animals showed a stereotypic running behaviour to various degrees. According to the animal caretakers, this stereotypic circling also occurs sporadically in animals of the CMV-cre strain, underlying the importance of

backcrosses to obtain a Cre-free strain. Coat colour, coat condition, body size and weight are similar between Cre-free Dpf3$^{-/-}$ mice and the knockout animals at 12 weeks or one year of age. The increase in body weight whithin this time range from 24 g to 33 g matches well with body weights of C57BL/6J mice at the same time points (Ackert-Bicknell et al. 2012; Genome Dynamics (CGD) 2012)). At the age of 1.5 years, the weight of the control animals is comparable to the 1 year old wild types. A constant weight was also observed in C57BL/6J mice at the same time points by (Yuan, Rosen, and Beamer 2012). In contrast to this, the 1.5 year old Dpf3$^{-/-}$ mice with Cre recombinase expression show a wide range of body weights. Mice with a muscle phenotype in the EDL and TA are relatively light (29 g to 31.4 g body weight) compared to the other knockout animals (38.5 g to 56.9 g body weight). The latter are not only heavier compared to Dpf3$^{-/-}$ with a muscle phenotype but also in comparison with control animals. As the muscle to body weight ratios of these animals are relatively low, a high fat content might contribute to the high body weights. The relatively low body weight of two out of three mice with a muscle phenotype presented in EDL and TA coincides with stereotypic running behaviour. However, the third light mouse with the same phenotype moved normally and the heaviest mouse (56.9 g) showed a partial phenotype in the EDL and irregular circling. If the non-circling mice tended to be more active or passive was not monitored. So it remains elusive if constant physical activity or metabolic changes due to the loss of Dpf3 caused the wide range of body weights (29 g to 56.9 g body weight) observed in the knockout mice. Future analyses of 1.5 years old Cre-free Dpf3$^{-/-}$ mice including body composition measurements and voluntary wheel running or treadmill training are necessary to explain the so far inconsistent relationship between the muscle phenotype, body weight and running.

Myonuclear localization in the centre of a muscle fibre occurs during muscle development, regeneration and in the context of muscle disease (Folker and Baylies 2013). Important proteins involved in nuclear positioning include subunits of the LINC (linker of nucleoskeleton and cytoskeleton) complex (Horn 2014), components of the cyto- and nucleoskeleton and proteins involved in nuclear movement (Folker and Baylies 2013). Two cytoskeletal proteins, the cardiac α-actin 1 (Actc1, FC = 2.1) and the actin related protein 3β (Actr3b, FC = 1.6), are upregulated in skeletal muslce from 12 week old Dpf3$^{-/-}$ mice compared to samples from wild type littermates. Actc1 is expressed in embryonic skeletal muscle and belongs to a myogenic gene expression program that is activated by MyoD, a prominent regulator of skeletal myogenesis (Ordahl 1986; Di Padova et al. 2007). Moreover, the cardiac α-actin can replace skeletal muscle α-actin in respective knockout mice, leading to up to 25 % force reduction compared to skeletal muscle α-actin expressing wild tpyes (Ochala et al. 2013). ACTR3b has been found twofold upregulated in patients with X-linked myotubular myopathy that is characterized by muscle weakness, hypotonia and feeding as well as breathing difficulties

(Noguchi et al. 2005). Structural characteristics of muscle fibres from those patients include mitochondrial accumulations and centrally placed myonuclei (Noguchi et al. 2005). Further experiments comparing the gene expression in young and 1.5 years old Dpf3$^{-/-}$ are required to determine if the centralization of myonuclei results from impaired nuclear positioning or if the centralization occurs as a result of accumulated dysfunctions and subsequent muscle repair.

It is of note that centralized myonuclei were only observed in the fast-twitch muscles EDL and TA and not in the soleus (slow-twitch) of Dpf3$^{-/-}$ mice. Slow-twitch fibres are rich in myoglobin, generate energy by oxidative metabolism and are more resistant to fatigue than fast-twitch fibres (Schiaffino and Reggiani 2011). These differences are also reflected in fibre type specific gene expression. Microarray analysis of single muscle fibres from mouse soleus and EDL revealed $\sim$ 480 type 1 specific genes and $\sim$ 300 type 2b specific genes (Chemello et al. 2011). Slow-twitch fibres express MyHC I whereas MyHC IIa, IIx and IIb are found in murine fast-twitch fibres. Whole muscles usually consist of a mixture of these fibre types. In the mouse, the soleus is composed of 42 % MyHC I fibres and 58 % MyHC IIa fibres whereas the EDL contains 11 % MyHC IIa and 88 % MyHC IIb fibres and the TA 26 % MyHC IIa and 74 % MyHC IIb fibres (Augusto, Padovani, and Campos 2004). Fibre type classification according to myosin ATPase staining reveals a small proportion of type I and mixed type I/IIa fibres ($\sim$ 4 %) in the EDL (Augusto, Padovani, and Campos 2004). To assess if the centralized myonuclei are specific for fast-twitch muscle fibres, cross-sections of EDL from 1.5 years old Dpf3$^{-/-}$ were stained for slow myosins. Centralized myonculei are detected in unstained fibres (assumed to be fast-twitch) as well as fibres stained with anti-slow myosin. If these fibres are pure type I or mixed type I/IIa fibres has to be determined by ATPase stainings. As the soleus is composed of MyHC I and IIa fibres and the EDL and TA contain only a minor proportion of MyHC IIa fibres, the phenotype might MyHC IIb-dependent. Fibre typing based on myosin ATPase staining are required to elucidate the putative relationship between centralized myonuclei and type IIb fibres. In addition, single fibre sequencing in type IIb fibres from Dpf3$^{-/-}$ mice might reveal disturbances in the type IIb specific gene set described by Chemello et al. (2011).

The age-dependent occurence of the muscle phenotype in Dpf3$^{-/-}$ mice indicates a break-down of putative compensation mechanisms due to age-related changes in gene expression and muscle architecture. Bruusgaard, Liestøl, and Gundersen (2006) compared the muscle fibres in EDL and soleus of 14 month and 23 month old mice by in vivo nuclear positioning analysis. While the soleus showed only a reduction in the number of myonuclei, the EDL in the 23 month old animals contained 40 % atrophied type IIb fibres, which are characterized by still randomly but not evenly spaced nuclear positioning and a less dense microtubule network (Bruusgaard, Liestøl, and Gundersen 2006). Of note, neither Bruusgaard, Liestøl,

and Gundersen (2006) nor Barns et al. (2014) (29 month old C57BL/6J) report centralized myonuclei in aged mice exceeding a proportion of 5 %. Even in mice that experienced downhill treadmill training for 14 weeks or long-term voluntary wheel running (12 month), damaged fibres with centralized myonuclei do not exceed 3.5 % (Lynch, Fary, and Williams 1997; Wernig, Irintchev, and Weisshaupt 1990). Similar effects of running and aging on skeletal muscles in rat are reported by Caccia, Harris, and Johnson (1979) as well as M. Brown, Ross, and Holloszy (1992). These studies support the assumption that the centralization of myonuclei is dependent on the loss of Dpf3 and not a consequence of aging or excercise per se.

The phenotype of zebrafish morphants upon *dpf3* morpholino knockdown includes myofibrillar disarray and transversion of somite boundaries (Lange et al. 2008). In contrast to this, the muscle fibres in the Dpf3$^{-/-}$ mice align in an ordered manner and the sarcomeric structure seems to be intact as judged from stainings with antibodies against α-actinin, desmin, tropomyosin, phalloidin and fast myosins.

4.1.1 Conclusion

Taken together, the loss of Dpf3 in the mouse model presents in a mild skeletal muscle phenotype that seems to be dependent on age and fibre type. To confirm a causal relationship between the loss of Dpf3 and the centralization of myonuclei in EDL and TA of 1.5 years old Dpf3$^{-/-}$ mice still expressing the Cre recombinase, further analyses in Cre-free mice of the same age are required. These should include histologic examination of fast- and slow-twitch muscles, body composition analysis in combination with voluntary wheel running or treadmill training to reveal the so far inconsistent relationship between body weight, running behaviour and centralized myonuclei, in vivo nuclear position analysis to find the onset of myonuclear centralization and careful determination of fibre types with peripherally and centrally placed myonuclei. Single fibre sequencing might help to unravel the underlying molecular mechanisms leading to the phenotype. The putative compensation mechanisms especially active in the heart, might be challenged by pressure overload induced by transverse aortic constriction or administration of isoproterenol. Moreover, the Dpf3$^{tm1.1Sper}$ strain presented here should be compared with the Dpf3$^{tm1.1Grc}$/J that is available from The Jackson Laboratory. So far, no phenotype was reported for the Dpf3$^{tm1.1Grc}$/J as well as for the Dpf1$^{tm1.1Grc}$/J knockout strain (also available from The Jackson Laboratory). In addition, breeding to another genetic background or the generation of a Dpf2/Dpf3 double knockout are putative ways towards a full understanding of the various roles of Dpf3.

4.2 The impact of DPF3 on alternative splicing

Whithin this thesis, several hypotheses regarding the impact of Dpf3 on alternative splicing were tested. For this purpose, the occurence of alternatively spliced transcripts in the absence or presence of Dpf3 are an indispensible prerequisite. Indeed, several hundred differential expressed isoforms were detected in heart and skeletal muscle samples from $Dpf3^{-/-}$ mice and knockdown of Dpf3 in the murine cardiomyocyte cell line HL-1. The number of genes with an isoform proportion shift in the absence of Dpf3 compared to controls ranges from 97 to 218. These numbers are in good agreement with altered alternative splicing events upon mutation, knockout or knockdown of epigenetic factors described in the literature (Luco, Pan, et al. 2010; Pradeepa et al. 2012; R. Guo et al. 2014; Deng et al. 2010; Sanchez et al. 2010; Tyagi et al. 2009; Waldholm et al. 2011). The depletion of the H3K36me3 binder MRG15 in human mesenchymal stem cells results in 186 altered splicing events (Luco, Pan, et al. 2010) and the loss of the H3K36me3 reader Psip in mouse embryonic fibroblasts derived from mutant mice is associated with 95 alternatively spliced exons with altered inclusion levels (Pradeepa et al. 2012). The histone variant H3.3K36me3 is bound by BS69 and knockdown of this histone reader in HeLa cells is followed by ~ 300 alternative splicing events, mainly intron retentions (R. Guo et al. 2014). Intron retention in 305 transcripts (Deng et al. 2010) and 471 transcripts (Sanchez et al. 2010) was also reported in Arabidopsis thaliana upon loss of function mutation of the methyltransferase PRMT5, which modifies arginines of histone 4 and 2A. These altered splicing events are confirmed in corresponding Drosophila mutants (418 transcripts) (Sanchez et al. 2010). In drosophila, the knockdown of the core BAF complex subunit dBrm results in 15 genes with an altered abundance of alternatively spliced transcripts and the depletion of Mor (orthologous to the human BAF170 and BAF155) and Snr1 (orthologous to the human hSNF5) has similar effects (Tyagi et al. 2009; Waldholm et al. 2011). However, the authors state that the Affymetrix Drosophila Genome 2 arrays used are not particularly designed as splicing arrays and do not cover the entire transcriptome (Tyagi et al. 2009; Waldholm et al. 2011). Therefore, the impact of the BAF complex on alternatively spliced transcripts is probably underestimated in these studies.

In analogy to recent discoveries of adapter molecules that link chromatin signatures with splicing factors (Sims et al. 2007; Loomis et al. 2009; Luco, Pan, et al. 2010; Pradeepa et al. 2012; R. Guo et al. 2014), an direct interaction of Dpf3 with the spliceosome was postulated. TAP-MS in combination with mass spectrometry in C2C12 cells revealed nine splicing factors whereas only three were identified as interaction partners of DPF3 in HEK293T cells (see Table 3.7). It is of note that the Mascot scores for the splicing factors are substantially lower compared to Mascot scores for BAF complex subunits indicating a weak interaction or low

abundance of splicing factors. As TAP-MS was developed to isolate protein complexes (Puig et al. 2001), it is prone for the detection of indirect interactions. Therefore, yeast two-hybrid screens were performed for the detection of direct interaction partners. Out of 244 splicing factors, 15 are able to interact with DPF3. In most cases, these bindings are supported by interaction of two to three out of 25 DPF3 constructs that showed an evaluable colony growth in the Y2H screen.

Surprisingly, the panel of DPF3 interacting splicing factors is not homogeneous and comprises spliceosomal core proteins that are also found in yeast (e.g. hBRR2 and subunits of the SF3a/b complex), core proteins that are specific for the human spliceosome (e.g. SR140) and splicing factors with regulatory or assisting functions (e.g. LUC7L). Moreover, the splicing factors cover more than 10 spliceosomal subgroups, which are assigned to early (A complex), intermediate (B complex) and late splicing steps (C complex, disassembly). So far, an interaction of human Brg1 with with the U5 snRNP associated kinases PRP4 and PRP6 and a general association to the U1 snRNP and U5 snRNP are reported (Dellaire et al. 2002; Batsché, Moshe Yaniv, and Christian Muchardt 2006). In *C. tetans* and *D. melanogaster*, an RNA dependent association of Brm with snRNPs was shown by coimmunoprecipitations using an antibody against Sm proteins, which are part of the U1, U2, U4 and U5 snRNPs (Liautard et al. 1982), but the interaction was not further narrowed to specific snRNPs or splicing factors (Tyagi et al. 2009).

C2H2 zinc fingers are known to interact with RNA, DNA and proteins and the canonical C2H2 fold of DPF2 is similar to the protein binding zinc finger proteins Zif268 and Zif484 (Brayer and Segal 2008; W. Zhang et al. 2011). With the exception of the splicing factor CBP80, the DPF3 constructs that interact with splicing factors contain the C2H2 zinc finger domain. This domain was present in 19 Dpf3 constructs that showed evaluable colony growth in the Y2H screen. As the YH2 method might also detect protein-protein interactions that are mediated by a bridging protein, detect weak interactions without biological relevance or due to misfolded domains in truncation constructs, the interactions should be validated by another method (Brückner et al. 2009). Typical validation rates range from 50 % to 70 % (Stelzl et al. 2005; Uetz et al. 2006). To assess, if the interactions between the splicing factors and DPF3 constructs are sound or false positive, four interaction pairs were selected for validations by a LUMIER asssay. As alternative splicing is based on the competition between different splice sites and their binding factors to be choosen for the splicing reaction, the LUMIER assays were performed with early acting splicing factors that exhibit such regulatory functions: IK (RED), LUC7L, RBBM39 and SR140. IK (RED) is a poorly characterized splicing factor of the B complex, which interacts with various splicing factors of the U5, U4 and U6 snRNPS as well as RES (retention and splicing) complex subunits and Prp19 related proteins (Hegele et al. 2012). In C. elegans, the homologous splicing factor

SMU-2 regulates in combination with SMU-1 the alternative splicing of a basement membrane proteoglycan (Spartz, Herman, and Shaw 2004). An interaction between the human proteins IK (RED) and hSMU-1 was shown by Y2H screens and coimmunoprecipitation (Hegele et al. 2012). LUC7L is one of four human proteins homologous to the yeast Luc7p splicing factor, a subunit of the U1 snRNP complex that is required in 5' splice site selection (Tufarelli et al. 2001). The role of RBM39 in splice site selection was investigated in mammalian cells and Schizosaccharomyces pombe (S. pombe). Dowhan et al. (2005) show that RBM39 regulates transcription and alternative pre-mRNA splicing in an steroid hormone receptor-dependent manner and Shao et al. (2012) report that the homologous Rsd1 splicing factor (S. pombe) bridges the U1 snRNP with Prp5, an essential ATPase for the transition from E to A complex formation. At the same timepoint, SR140 is present in the U2 snRNP assembly (Will, Urlaub, et al. 2002). This splicing factor of unknown function is part of a network of A and U2 related proteins and interacts directly with SPF45, an splicing factor important for alternative splicing (Hegele et al. 2012; Corsini et al. 2007). None of these splicing factors showed an interaction with DPF3 in standard LUMIER assays. Only SR140 bound to DPF3b under high salt washing conditions. However, this finding is not consistent with the results from the Y2H screen. Therefore, these results suggest that the interactions detected in the yeast two-hybrid screen might be an incidental event based on unspecific binding of the C2H2 zinc finger. An unspecific interaction might also explain the low number of DPF3 constructs that result in colony growth. Except of the DPF3-SR140 interaction, only one to three out of 25 DPF3 constructs with evaluable colony growth interacted with splicing factors upon mating with the prey matrix. In line with this is also the DPF3a-LUC7L2 interaction from the Y2H screen using a human fetal brain library that could not be validated by GST-pulldowns and coimmunoprecipitation.

Other splicing factors from the Y2H screen include the essential splicing factors hPRP31, hBRR2, SKIP and SNRPF. hPRP31 is involved in U4/U6.U5 tri-snRNP assembly and the transition towards the activated B complex (Makarova, Makarov, S. Liu, et al. 2002). This step is impossible without the catalytic activity of hBRR2. hBRR2 is associated to the U5 snRNP and unwinds the U4/U6 RNA duplex, leading to the dissociation of the U4 snRNP (Laggerbauer, Achsel, and Lührmann 1998). SKIP is a splicing factor assigned to the catalytically active B* complex (Makarov et al. 2002) and SNRPF is part of the heptameric Sm ring that is present in U1, U2, U4 and U5 snRNPs (Chari et al. 2008). For these splicing factors, a mechanism of DPF3 dependent alternative splicing regulation is difficult to envision as they act after splice site pairing and in late spliceosomal assemblies. Of unknown or mainly other function are the splicing factors FAM50B, the cap binding protein NCBP1 and the double strand RNA binding protein ILF3. In contrast to this, the remaining splicing factors U2AF35, PHF5A, SF3b2 and SF3b3 are U2 and U2 related

proteins that are present in early spliceosomal assemblies. PHF5A, SF3b2 and SF3b3 are subunits of the SF3b complex that contacts the branch point and is released before the first catalytic reaction (Dybkov et al. 2006). U2AF35 is the minor part of the U2AF heterodimer and binds weakly to the 3' splice site (Kielkopf et al. 2001). Despite its low affinity to RNA, U2AF35 is required for the selection of some weak splice sites (Pacheco et al. 2006). Recently, Kralovicova et al. (2015) concretised the number of U2AF35 dependent exons to more than 1000 by RNAseq upon U2AF35 siRNA depletion in HEK293 cells. These findings make U2AF35 and the SF3b subunits to more promising candidates compared to the late acting splicing factors described above. However, the interaction with Dpf3 is supported by maximal three out of 19 DPF3 constructs with a C2H2 zinc finger domain. Moreover, the results for U2AF35 and PHF5 in the Y2H screen (DPF3a specific) are in conflict with non-significant TAP-MS results (DPF3b specific, Mascot scores < 50). So it is likely that these Y2H results are also false-positive.

As the results from the protein-protein interaction assays are inconsistent, the adapter model alone seems inappropriate to explain the occurence of alternatively spliced transcripts upon depletion of Dpf3. Therefore, the focus turned towards the kinetic regulation of the splicing process. The kinetic splicing model postulates that the Pol II elongation rate influences the splice site choice (Naftelberg et al. 2015). A reduced Pol II elongation rate, which can be regulated by the chromatin density, favors the usage of weak splice sites (Ip et al. 2011; Jimeno-González et al. 2015). In accordance with this model are observations that SWI/SNF chromatin remodeling complexes are not only associated with promotors but also involved in Pol II elongation (Sullivan et al. 2001; Armstrong et al. 2002; Corey et al. 2003). Moreover, SWI/SNF subunits interact with Pol II (C. J. Wilson et al. 1996; Neish et al. 1998; H. Cho et al. 1998) and 40 % of high-confidence SWI/SNF regions, derived from overlapping ChIPseq data of several SWI/SNF subunits, overlap with Pol II-rich sequences (G. M. Euskirchen et al. 2011). Therefore, the RNAseq data from Dpf3 depletion and control samples were analyzed in respect of a potential role of Dpf3 as recruiting factor for the BAF complex that enables a fast Pol II elongation. The genes with isoform proportion shifts upon the depletion of Dpf3 are represented by $\sim$ 500 to 1100 transcripts. If Dpf3 and the BAF complex act as described above, the depletion of Dpf3 would cause a slow Pol II rate that favors the inclusion of weak exons. One quarter to one third of the transcripts is characterized by enhanced exon inclusion in the Dpf3 knockdown and knockout conditions, whereby weak and strong splice sites are balanced. To examine if splicing of the exons with weak splice sites is regulated by Dpf3, the abundance of histones carrying modifications that can be recognized by Dpf3 was determined by overlapping self-generated and publicly available ChIPseq data (see Table 3.11) with the exon sequences of interest. A significantly higher overlap is observed for exons with weak splice sites. However, the abundance of exons

with such histones does not exceed 34 %. The higher abundance of Dpf3 binding histones on weak exons either supports the hypothesis that Dpf3 regulates the splicing outcome or it might be explained by the general higher nucleosome occupancy at exons with weak splice sites (Tilgner et al. 2009). For clarification, publicly available ChIPseq data were mined for SWI/SNF complex subunits. A poor overlap of Brg1 ChIPseq peaks with exons characterized by selected histone modifications does not support a relevant role of Dpf3 as recruitment factor of the SWI/SNF complex that subsequently enhances the Pol II rate.

An opposite role of the SWI/SNF complexes on splicing by slowing down the elongation rate of Pol II is described by Batsché, Moshe Yaniv, and Christian Muchardt (2006) and Zraly and Dingwall (2012). On the CD44 gene, the inclusion of variant exons is regulated by BRM as part of the SWI/SNF complex via a reduction of the Pol II elongation rate and depletion of BRM results in exon skipping (Batsché, Moshe Yaniv, and Christian Muchardt 2006). This regulation is independent from the ATPase activity of BRM and involves Ser-5 phosphorylation of Pol II. An increase in Ser-5 phosphorylation was also observed in hormone dependent Eig genes of Drosophila and accompanied by SWI/SNF binding and intron retention (Zraly and Dingwall 2012). In the absense of the SWI/SNF complex, Ser-2 Pol II is the predominant form and the Eig genes are properly spliced. This alternative splicing events did not depend on a reduced Pol II elongation rate but on the ability of Ser-2 Pol II to recruit splicing factors whereas Ser-5 Pol II produces unprocessed transcripts (Zraly and Dingwall 2012; Hargreaves, Horng, and Medzhitov 2009). It is assumed that the Snr subunit inhibits the the dBRM chromatin remodeling activity until a hormone induced signal is strong enough to stopp the dBRM inhibition resulting in the release of Ser-5 Pol II (Zraly and Dingwall 2012). To analyze if Dpf3 is involved in the formation of such SWI/SNF barriers and Pol Ser-5 phosphorylation, additional experiments aiming to determine the distribution of Ser-2 and Ser-5 Pol II are required.

A recent study in S. pombe with mutants overexpressing SF3 complex splicing factors and depletion of SWI/SNF subunits orthologous to hSNF5 and ARID reveals a lower nucleosome occupancy at intron-containing genes and a reduced level of cdc28, an orthologous ATPase to hPRP2 that is required for the formation of the catalytically active B complex (Patrick et al. 2015). The authors assume that the SWI/SNF complex is required to assemble histones as speed bumps for the Pol II. To analyze if these mechanisms apply for DPF3 and its role in splicing regulation, the requirement of DPF3 in the SWI/SNF complexes for histone assembly has to be tested experimentally.

In addition, the possible implications of the SWI/SNF complex in alternative splicing regulation might also be based on RNA binding as shown by Tyagi et al. (2009) in Chironomus tetans and Drosophila melanogaster. Depletion of several SWI/SNF subunits results in

alternative splicing events with favored distal as well as proximal splice sites, suggesting an additional regulation mechanism independent from Pol II elongation (Tyagi et al. 2009; Waldholm et al. 2011). Analysis of gold-labeled ctBrm in C. tetans polytene chromosomes revealed a fraction of ctBrm that is associated to pre-mRNA and distant to chromatin (Tyagi et al. 2009). Moreover, Brm is associated with snRNPs in an RNA dependent manner (Tyagi et al. 2009). To analyze if DPF3 mediates an interaction of the SWI/SNF complex to RNA, PAR-CLIP experiments were performed. Although DPF3a is a moderate RNA binding molecule, a binding motif was not found suggesting an unspecific interaction between maturing transcripts and DPF3a.

4.2.1 Conclusion

The depletion of Dpf3 causes not only differentially expressed genes but also alternatively spliced exons that cause low to moderate isoform proportion shifts in up to $\sim$ 200 genes. The underlying mechanisms are still obscure. However, the experiments performed within this thesis exclude several possible explanations. An direct interaction of Dpf3 with splicing factors according to the adapter model is unlikely. Several splicing factors detected by TAP-MS in C2C12 cells and HEK293T cells are at the lower range of peptide abundance, indicating a weak or unspecific binding. Moreover, direct protein-protein interactions detected by a Y2H screen are supported by only one to three out of 25 non-autoactive DPF3 vectors except of the interaction with SR140 (six DPF3 vectors). In addition, the validation experiments focusing on regulatory splicing factors are negative or inconsistent with the results from the Y2H screen. However, further LUMIER assays including the U2 and U2 related proteins U2AF35, SF3b2, SF3b3 and PHF5A might confirm the interaction in the Y2H screen. In a recent study in S. pombe, several splicing defects were observed in double mutants of the SWI/SNF and SF3 complex (Patrick et al. 2015).

A putative role of Dpf3 in kinetic splicing regulation by acceleration of the Pol II elongation rate was analyzed in respect of the chromatin remodeling activity of the SWI/SNF complex during Pol II elongation. A poor overlap of ChIPseq data for histone modifications that are recognized by Dpf3 as well as ChIPseq data for Brg1 as representative for the BAF complex cannot explain the alternative splicing events. For the analysis of a possible role of Dpf3 as recruitment factor for the SWI/SNF complex as a barrier for Pol II elongation and subsequent Pol II Ser-5 phosphorylation, an inverse analysis of the RNAseq data (assuming $>$ 10 % more read counts in wild type instead of knockout samples, see Figure 3.23) and additional ChIPseq experiments including antibodies against additional SWI/SNF subunits and Pol II Ser-2 as well as Ser-5 phosphorylation are required.

Finally, a splicing regulation based on RNA binding is rouled out by PAR-CLIP experiments. Although a moderate interaction of DPF3a with RNA was observed, no overrepresented binding motifs were found in the sequencing data.

As the $\Delta\Psi$ values in the genes with isoform proportion shifts are relatively low, it is reasonable that the impact of Dpf3 on alternative splicing is compensated in the analyzed matarial from 12 week old animals. Future analyses on material from 1.5 years old $Dpf3^{-/-}$ with a phenotype or from Dpf2/Dpf3 double knockouts and respective controls might facilitate the search for the underlying molecular mechanisms that can explain the impact of Dpf3 on alternative splicing.

5 Summary

The epigenetic transcription factor DPF3 belongs to the d4 gene family with its additional members DPF1 and DPF2. The biological functions of DPF3 are related to chromatin remodeling and are best described in the context of heart and skeletal muscle development and disease. Previous studies in the zebrafish model revealed a severe phenotype in the heart and somites.

To elucidate if Dpf3 has similar functions in the mammalian system, a knockout mouse strain was generated by mating animals carrying loxP sites at the second exon of Dpf3 with mice expressing the Cre recombinase. Animals of the $Dpf3^{-/-}$ strain are viable, fertile, the distribution of female and male offspring is balanced and the inheritance of the knockout allele follows the Mendelian laws. The expression of related proteins (Dpf1, Dpf2, Phf10) is not altered by the loss of Dpf3. In 12 weeks old $Dpf3^{-/-}$ mice, $\sim$ 300 to 600 genes show an equal to or more than 1.5-fold up- or downregulation in striated muscles. Cre-free knockout animals and wild type littermates were physically and histologically examined up to the age of one year with similar results for both animal groups. However, in 1.5 years old knockout animals still expressing the Cre recombinase, a phenotype with incomplete penetrance was observed. In three out of eight $Dpf3^{-/-}$ mice, myonuclear centralizations were observed in the whole cross-sectional area of the extensor digitorum longus (EDL) and tibialis anterior (TA). In addition, misplaced myonuclei were detected at some spots in the EDL of two other knockout mice. As the myonuclear positioning was normal in the soleus (slow-twitch muscle), the phenotype seems to be fibre type dependent and restricted to fast-twitch muscles. The inner muscle architecture was examined by immunostainings of several sarcomeric proteins and the striated patterns are regular irrespective of the myonuclear positioning.

A second project aimed to investigate the role of DPF3 in the regulation of alternative splicing in respect of a function as an adapter molecule between chromatin and the spliceosome, in regard to a function as an indirect splicing regulator that modulates the elongation rate of the RNA polymerase II (kinetic model) or a splicing modulator that binds to pre-mRNA. Protein-protein interaction methods including a Yeast 2-hybrid screen and co-precipitation methods gave inconsistent results. The kinetic model assuming an acceleration of the Pol II elongation rate by chromatin remodeling was not supported by experimental data whereas

the opposite assumption (slow-down of Pol II) is not analyzed so far. The binding of DPF3a to mRNA is moderate but not supported by a binding motif. Thus, future experiments for example in aged Dpf3$^{-/-}$ mice will further elucidate the underlying molecular mechanisms that lead to isoform proportion shifts in up to $\sim$ 200 genes.

6 Zusammenfassung

Der epigenetische Transkriptionsfaktor DPF3 gehört zur d4 Genfamilie, die als weitere Mitglieder DPF1 und DPF2 enthält. Die biologischen Funktionen von DPF3 stehen im Zusammenhang mit Chromatin-Remodeling und sind am besten in Hinblick auf die Entwicklung von Herz- und Skelettmuskulatur sowie im Kontext angeborener Herzerkrankungen untersucht. Ein Knockdown von dpf3 im Zebrabärbling führt zu einem ausgeprägten Phänotyp im Herzen und in den Somiten.

Um diese Forschung im Säugetier-Modell fortzuführen, wurde ein Dpf3-Knockout Mausstamm generiert. Hierfür wurden Tiere, dessen zweites Exon von Dpf3 von loxP-Rekombinationssequenzen flankiert war, mit Mäusen, die die Cre recombinase exprimieren, gekreuzt. Resultierene $Dpf3^{-/-}$-Mäuse sind fertil, das Verhältnis von männlichen und weiblichen Nachkommen ist ausgeglichen und die Vererbung des $Dpf3^{-/-}$-Allels erfolgt gemäß den Mendelschen Regeln. Die Expression von Dpf3-ähnlichen Proteinen (Dpf1, Dpf2, ,Phf10) wird nicht durch den Verlust von Dpf3 beeinflusst. In 12 Wochen alten Knockout-Tieren zeigen $\sim$ 300 bis 600 Gene der Herz- und Skelettmuskulatur ein um mindestens 1.5-fach verändertes Expressionsniveau. Das äußere Erscheinungsbild sowie histologische Untersuchungen von Gewebe aus Cre-freien $Dpf3^{-/-}$-Mäusen bis zu einem Alter von einem Jahr ähnelt entsprechenden Wildtypkontrollen. Im Gegensatz dazu zeigen 1.5 Jahre alte Knockout-Tiere, die noch die Cre recombinase exprimieren, einen Phänotyp mit unvollständiger Penetranz. Der gesamte Muskelquerschnitt des Tibialis anterior (TA) und Extensor digitorum longus (EDL) weist in drei von acht Knockout-Mäusen zentralisierte Zellkerne auf. Darüberhinaus sind mittig platzierte Zellkerne in begrenzten Arealen des EDL in zwei weiteren $Dpf3^{-/-}$-Tieren beobachtet worden. Da die räumliche Verteilung der Zellkerne im Soleus (slow-twitch Muskel) normal ist, scheint der Phänotyp spezifisch für Muskulatur mit einem hohen Anteil an fast-twitch-Fasern zu sein. Die innere Muskelarchitektur wurde durch Immunfärbungen von Sarkomerproteinen untersucht und ist unauffällig.

In einem zweiten Projekt wurde eine mögliche Rolle von DPF3 in der Regulation des alternativen Spleißens untersucht. Eine mögliche Funktion als Adapter-Molekül, das die Chromatinstruktur mit dem Spliceosome verbindet, wurde in einem Hefe-2-Hybrid-System sowie Co-Präzipitationen untersucht, die widersprüchliche Ergebnisse aufweisen. Eine indirekte

Funktion als regulatorisches Element der Elongationsgeschwindigkeit der RNA Polymerase II konnte in Hinblick auf eine beschleunigende Wirkung durch Chromatin-Remodeling nicht bestätigt werden. Die gegenteilige Annahme (Chromatin-Remodeling bremst die RNA Polymerase II) wurde nicht weiter untersucht. Eine dritte Möglichkeit, eine regulatorische Wirkung von DPF3 durch das Binden an pre-mRNA, wurde aufgrund eines fehlenden Bindemotivs ebenfalls nicht bestätigt, sodass die molekularen Mechanismen, die eine veränderte Isoformenverteilung in Abwesenheit von Dpf3 in bis zu $\sim$ 200 Genen erklären könnten, in zukünftigen Experimenten zum Beispiel in gealterten Dpf3-Knockoutmäusen weiter untersucht werden.

7 Scientific contributions

Characterization of the Dpf3 knockout mouse

Supervision	Silke Rickert-Sperling
Generation of $Dpf3^{tm1Sper}$ (DIPF) mice	inGenious Targeting Laboratory, Inc. (iTL)
CMV-cre mice	provided by Heinrich Schrewe (MPIMG)
Generation of $Dpf3^{-/-}$ mice, Cre positive	Jenny Schlesinger, **Katherina Bellmann**
Generation of Cre-free $Dpf3^{-/-}$	**Katherina Bellmann**
Animal care	Mirjam Peetz (animal facility, MPIMG), Birgit Frenzel (animal facility, MDC)
Genotyping	Jenny Schlesinger, Ilona Dunkel, **Katherina Bellmann**, Huanhuan Cui, Kerstin Schulz
Sanger sequencing	Huanhuan Cui, Kerstin Schulz
qPCR (Dpf3 and orthologs)	**Katherina Bellmann**, Huanhuan Cui, Sandra Schmitz
Calculations (allele inheritance, fertility)	**Katherina Bellmann**
Weight recordings	**Katherina Bellmann**, Huanhuan Cui
RNA isolation	**Katherina Bellmann**, Huanhuan Cui
Library preparation for RNAseq	Kerstin Schulz
Sequencing	Ilona Dunkel (MPIMG)
Computational analysis	Vikas Bansal
Validation by qPCR	**Katherina Bellmann**
Histology	**Katherina Bellmann**

The impact of Dpf3 on alternative splicing

Supervision	Silke Rickert-Sperling
RNA isolation	see above
Library preparation	see above

Sequencing	see above
Computational analysis	Sandra Appelt, Marcel Grunert

The interation of DPF3 with the spliceosome

Supervision	Silke Rickert-Sperling, Ulrich Stelzl (MPIMG)
TAP-MS	Martin Lange
Y2H screen (fetal brain library)	Martin Lange
Validation (DPF3-LUC7L2)	**Katherina Bellmann**
Y2H (spliceosomal matrix)	**Katherina Bellmann**
LUMIER assays	**Katherina Bellmann**

The role of Dpf3 in the kinetic splicing model

Supervision	Silke Rickert-Sperling
RNA isolation	see above
Library preparation	see above
Sequencing	see above
Computational analysis	Sandra Appelt, Marcel Grunert
ChIP (H3K4me1, H4K16ac)	**Katherina Bellmann**
ChIP library preparation	Kerstin Schulz
Sequencing	Mirjam Feldkamp (BIMSB)
Computational analysis	Vikas Bansal

The interaction of Dpf3 with RNA

Supervision	Silke Rickert-Sperling, Markus Landthaler (BIMSB)
Stable transfection of HEK293 cells	Miha Milek (BIMSB)
PAR-CLIP (transient transfection)	**Katherina Bellmann**
Library preparation	**Katherina Bellmann**
Sequencing	Mirjam Feldkamp (BIMSB)
Computational analysis	Miha Milek (BIMSB), Vikas Bansal

Funding

This work was supported by the EU FP7 IP CardioNet #289600, the German Research Foundation and the Sonnenfeld-Stiftung.

Bibliography

Ackert-Bicknell, C et al. (2012) *Aging study: Bone mineral density and body composition of 32 inbred strains of mice. MPD:Ackert1*. Mouse Phenome Database web site, The Jackson Laboratory, Bar Harbor, Maine USA. URL: `http://phenome.jax.org` (visited on 11/09/2015).

Allan, James et al. (1986) Roles of H1 domains in determining higher order chromatin structure and H1 location. *Journal of molecular biology* 187(4), pp. 591–601.

Allen, Benjamin L and Dylan J Taatjes (2015) The Mediator complex: a central integrator of transcription. *Nature Reviews Molecular Cell Biology* 16(3), pp. 155–166.

Amit, Maayan et al. (2012) Differential GC content between exons and introns establishes distinct strategies of splice-site recognition. *Cell reports* 1(5), pp. 543–556.

Anokhina, Maria et al. (2013) RNA structure analysis of human spliceosomes reveals a compact 3D arrangement of snRNAs at the catalytic core. *The EMBO journal* 32(21), pp. 2804–2818.

Armstrong, Jennifer A et al. (2002) The Drosophila BRM complex facilitates global transcription by RNA polymerase II. *The EMBO journal* 21(19), pp. 5245–5254.

Ascano, Manuel et al. (2012) Identification of RNA–protein interaction networks using PAR-CLIP. *Wiley Interdisciplinary Reviews: RNA* 3(2), pp. 159–177.

Ast, Gil (2004) How did alternative splicing evolve? *Nature Reviews Genetics* 5(10), pp. 773–782.

Augusto, Valéria, Carlos Roberto Padovani, and GE Rocha Campos (2004) Skeletal muscle fiber types in C57BL6J mice. *Braz J Morphol Sci* 21(2), pp. 89–94.

Bannister, Andrew J and Tony Kouzarides (2011) Regulation of chromatin by histone modifications. *Cell research* 21(3), pp. 381–395.

Barnes, Christopher O. et al. (2015) Crystal Structure of a Transcribing RNA Polymerase II Complex Reveals a Complete Transcription Bubble. *Molecular Cell* 59(2), pp. 258–269.

Barns, Mitchell et al. (2014) Molecular analyses provide insight into mechanisms underlying sarcopenia and myofibre denervation in old skeletal muscles of mice. *The international journal of biochemistry & cell biology* 53, pp. 174–185.

Barrios-Rodiles, Miriam et al. (2005) High-throughput mapping of a dynamic signaling network in mammalian cells. *Science* 307(5715), pp. 1621–1625.

Barski, Artem et al. (2007) High-resolution profiling of histone methylations in the human genome. *Cell* 129(4), pp. 823–837.

Batsché, Eric, Moshe Yaniv, and Christian Muchardt (2006) The human SWI/SNF subunit Brm is a regulator of alternative splicing. *Nature structural & molecular biology* 13(1), pp. 22–29.

Belew, Ashton Trey et al. (2014) Ribosomal frameshifting in the CCR5 mRNA is regulated by miRNAs and the NMD pathway. *Nature* 512(7514), pp. 265–269.

Beltrao, Pedro et al. (2013) Evolution and functional cross-talk of protein post-translational modifications. *Molecular systems biology* 9(1), p. 714.

Bentley, David L (2014) Coupling mRNA processing with transcription in time and space. *Nature Reviews Genetics* 15(3), pp. 163–175.

Berget, Susan M (1995) Exon recognition in vertebrate splicing. *Journal of biological Chemistry* 270(6), pp. 2411–2414.

Blake, Judith A et al. (2003) MGD: the mouse genome database. *Nucleic acids research* 31(1), pp. 193–195.

Bouabe, Hicham and Klaus Okkenhaug (2013) Gene targeting in mice: a review. In: *Virus-Host Interactions*. Springer, pp. 315–336.

Brayer, Kathryn J and David J Segal (2008) Keep your fingers off my DNA: protein–protein interactions mediated by C2H2 zinc finger domains. *Cell biochemistry and biophysics* 50(3), pp. 111–131.

Brown, M, TP Ross, and JO Holloszy (1992) Effects of ageing and exercise on soleus and extensor digitorum longus muscles of female rats. *Mechanisms of ageing and development* 63(1), pp. 69–77.

Brückner, Anna et al. (2009) Yeast two-hybrid, a powerful tool for systems biology. *International journal of molecular sciences* 10(6), pp. 2763–2788.

Brugiolo, Mattia, Lydia Herzel, and Karla M Neugebauer (2013) Counting on co-transcriptional splicing. *F1000prime reports* 5.

Bruusgaard, JC, K Liestøl, and K Gundersen (2006) Distribution of myonuclei and microtubules in live muscle fibers of young, middle-aged, and old mice. *Journal of applied physiology* 100(6), pp. 2024–2030.

Buchman, Vladimir L et al. (1992) Differential splicing creates a diversity of transcripts from a neurospecific developmentally regulated gene encoding a protein with new zinc-finger motifs. *Nucleic acids research* 20(21), pp. 5579–5585.

Busch, Anke and Klemens J Hertel (2012) Evolution of SR protein and hnRNP splicing regulatory factors. *Wiley Interdisciplinary Reviews: RNA* 3(1), pp. 1–12.

Caccia, Mario R, John B Harris, and Margaret A Johnson (1979) Morphology and physiology of skeletal muscle in aging rodents. *Muscle & nerve* 2(3), pp. 202–212.

Cevher, Murat A et al. (2014) Reconstitution of active human core Mediator complex reveals a critical role of the MED14 subunit. *Nature structural & molecular biology* 21(12), pp. 1028–1034.

Chan, Shih-Peng et al. (2003) The Prp19p-associated complex in spliceosome activation. *Science* 302(5643), pp. 279–282.

Chari, Ashwin et al. (2008) An assembly chaperone collaborates with the SMN complex to generate spliceosomal SnRNPs. *Cell* 135(3), pp. 497–509.

Chemello, Francesco et al. (2011) Microgenomic analysis in skeletal muscle: expression signatures of individual fast and slow myofibers. *PLoS One* 6(2), e16807.

Chen, Ginny I and Anne-Claude Gingras (2007) Affinity-purification mass spectrometry (AP-MS) of serine/threonine phosphatases. *Methods* 42(3), pp. 298–305.

Chen, Wei et al. (2014) Exon skipping event prediction based on histone modifications. *Interdisciplinary Sciences: Computational Life Sciences* 6(3), pp. 241–249.

Chestkov, Alexander V et al. (1996) The d4 gene family in the human genome. *Genomics* 36(1), pp. 174–177.

Cho, Helen et al. (1998) A human RNA polymerase II complex containing factors that modify chromatin structure. *Molecular and cellular biology* 18(9), pp. 5355–5363.

Cho, Suhyung et al. (2011) Interaction between the RNA binding domains of Ser-Arg splicing factor 1 and U1-70K snRNP protein determines early spliceosome assembly. *Proceedings of the National Academy of Sciences* 108(20), pp. 8233–8238.

Clapier, Cedric R and Bradley R Cairns (2009) The biology of chromatin remodeling complexes. *Annual review of biochemistry* 78, pp. 273–304.

Claycomb, William C et al. (1998) HL-1 cells: a cardiac muscle cell line that contracts and retains phenotypic characteristics of the adult cardiomyocyte. *Proceedings of the National Academy of Sciences* 95(6), pp. 2979–2984.

Cordin, Olivier and Jean D Beggs (2013) RNA helicases in splicing. *RNA biology* 10(1), pp. 83–95.

Corey, Laura L et al. (2003) Localized recruitment of a chromatin-remodeling activity by an activator in vivo drives transcriptional elongation. *Genes & development* 17(11), pp. 1392–1401.

Corsini, Lorenzo et al. (2007) U2AF-homology motif interactions are required for alternative splicing regulation by SPF45. *Nature structural & molecular biology* 14(7), pp. 620–629.

Corvelo, André et al. (2010) Genome-wide association between branch point properties and alternative splicing. *PLoS Comput Biol* 6(11), e1001016.

Cramer, Patrick (2002) Multisubunit RNA polymerases. *Current opinion in structural biology* 12(1), pp. 89–97.

Cui, Huanhuan et al. (2015) Phosphorylation of the chromatin remodeling factor DPF3a induces cardiac hypertrophy through releasing HEY repressors from DNA. *Nucleic Acids Research*, gkv1244.

Cutter, Amber R and Jeffrey J Hayes (2015) A brief review of nucleosome structure. *FEBS letters* 589(20PartA), pp. 2914–2922.

David, Charles J et al. (2011) The RNA polymerase II C-terminal domain promotes splicing activation through recruitment of a U2AF65–Prp19 complex. *Genes & development* 25(9), pp. 972–983.

De Conti, Laura, Marco Baralle, and Emanuele Buratti (2013) Exon and intron definition in pre-mRNA splicing. *Wiley Interdisciplinary Reviews: RNA* 4(1), pp. 49–60.

De Gasperi, Rita et al. (2008) The IRG mouse: a two-color fluorescent reporter for assessing Cre-mediated recombination and imaging complex cellular relationships in situ. *Genesis (New York, NY: 2000)* 46(6), pp. 308–317.

Dellaire, Graham et al. (2002) Mammalian PRP4 kinase copurifies and interacts with components of both the U5 snRNP and the N-CoR deacetylase complexes. *Molecular and cellular biology* 22(14), pp. 5141–5156.

Deng, Xian et al. (2010) Arginine methylation mediated by the Arabidopsis homolog of PRMT5 is essential for proper pre-mRNA splicing. *Proceedings of the National Academy of Sciences* 107(44), pp. 19114–19119.

Di Padova, Monica et al. (2007) MyoD acetylation influences temporal patterns of skeletal muscle gene expression. *Journal of Biological Chemistry* 282(52), pp. 37650–37659.

Dinman, Jonathan D (2012) Mechanisms and implications of programmed translational frameshifting. *Wiley Interdisciplinary Reviews: RNA* 3(5), pp. 661–673.

Dobin, Alexander et al. (2013) STAR: ultrafast universal RNA-seq aligner. *Bioinformatics* 29(1), pp. 15–21.

Dobrzynski, Halina et al. (2013) Structure, function and clinical relevance of the cardiac conduction system, including the atrioventricular ring and outflow tract tissues. *Pharmacology & therapeutics* 139(2), pp. 260–288.

Dowhan, Dennis H et al. (2005) Steroid hormone receptor coactivation and alternative RNA splicing by U2AF 65-related proteins CAPERα and CAPERβ. *Molecular cell* 17(3), pp. 429–439.

Dybkov, Olexandr et al. (2006) U2 snRNA-protein contacts in purified human 17S U2 snRNPs and in spliceosomal A and B complexes. *Molecular and cellular biology* 26(7), pp. 2803–2816.

Eick, Dirk and Matthias Geyer (2013) The RNA polymerase II carboxy-terminal domain (CTD) code. *Chemical reviews* 113(11), pp. 8456–8490.

Emili, Andrew et al. (2002) Splicing and transcription-associated proteins PSF and p54nrb/nonO bind to the RNA polymerase II CTD. *Rna* 8(9), pp. 1102–1111.

Enroth, Stefan et al. (2012) Combinations of histone modifications mark exon inclusion levels. *PLoS One* 7(1), e29911.

Erkelenz, Steffen et al. (2013) Position-dependent splicing activation and repression by SR and hnRNP proteins rely on common mechanisms. *RNA* 19(1), pp. 96–102.

Eskola, Satu and Eila Kaliste-Korhonen (1999) Nesting material and number of females per cage: effects on mouse productivity in BALB/c, C57BL/6J, DBA/2 and NIH/S mice. *Laboratory animals* 33(2), pp. 122–128.

Euskirchen, Ghia M et al. (2011) Diverse roles and interactions of the SWI/SNF chromatin remodeling complex revealed using global approaches. *PLoS Genet* 7(3), e1002008–e1002008.

Euskirchen, Ghia, Raymond K Auerbach, and Michael Snyder (2012) SWI/SNF chromatin-remodeling factors: multiscale analyses and diverse functions. *Journal of Biological Chemistry* 287(37), pp. 30897–30905.

Fearnley, Claire J, H Llewelyn Roderick, and Martin D Bootman (2011) Calcium signaling in cardiac myocytes. *Cold Spring Harbor perspectives in biology* 3(11), a004242.

Feltz, Clarisse van der et al. (2012) Architecture of the spliceosome. *Biochemistry* 51(16), pp. 3321–3333.

Flores-Alcantar, Angel et al. (2011) Dynamics of expression of ARID1A and ARID1B subunits in mouse embryos and in cells during the cell cycle. *Cell and tissue research* 345(1), pp. 137–148.

Folker, Eric S and Mary K Baylies (2013) Nuclear positioning in muscle development and disease. *Frontiers in physiology* 4, article 363.

Gabig, Theodore G, Colin D Crean, et al. (1998) Expression and chromosomal localization of the Requiem gene. *Mammalian genome* 9(8), pp. 660–665.

Gabig, Theodore G, Patricia L Mantel, et al. (1994) Requiem: a novel zinc finger gene essential for apoptosis in myeloid cells. *Journal of Biological Chemistry* 269(47), pp. 29515–29519.

Gao, Kaiping et al. (2008) Human branch point consensus sequence is yUnAy. *Nucleic acids research* 36(7), pp. 2257–2267.

Geeves, Michael A and Kenneth C Holmes (2005) The molecular mechanism of muscle contraction. *Advances in protein chemistry* 71, pp. 161–193.

Genome Dynamics (CGD), Center for (2012) *Multi-system survey of mouse physiology in 72 inbred strains of mice (ANOVA-adjusted methodology). MPD:CGDpheno1.* Mouse Phenome Database web site, The Jackson Laboratory, Bar Harbor, Maine USA. URL: `http://phenome.jax.org` (visited on 11/09/2015).

Gingras, Anne-Claude et al. (2005) A novel, evolutionarily conserved protein phosphatase complex involved in cisplatin sensitivity. *Molecular & cellular proteomics* 4(11), pp. 1725–1740.

Goehler, Heike et al. (2004) A protein interaction network links GIT1, an enhancer of huntingtin aggregation, to Huntington's disease. *Molecular cell* 15(6), pp. 853–865.

Guo, Rui et al. (2014) BS69/ZMYND11 reads and connects histone H3. 3 lysine 36 trimethylation-decorated chromatin to regulated pre-mRNA processing. *Molecular cell* 56(2), pp. 298–310.

Guo, Wei et al. (2012) RBM20, a gene for hereditary cardiomyopathy, regulates titin splicing. *Nature medicine* 18(5), pp. 766–773.

Hafner, Markus et al. (2010) PAR-CliP-a method to identify transcriptome-wide the binding sites of RNA binding proteins. *Journal of visualized experiments: JoVE* (41), e2034.

Hargreaves, Diana C, Tiffany Horng, and Ruslan Medzhitov (2009) Control of inducible gene expression by signal-dependent transcriptional elongation. *Cell* 138(1), pp. 129–145.

Hegele, Anna et al. (2012) Dynamic protein-protein interaction wiring of the human spliceosome. *Molecular cell* 45(4), pp. 567–580.

Helmes, Michiel, Henk Granzier, et al. (1996) Titin develops restoring force in rat cardiac myocytes. *Circulation Research* 79(3), pp. 619–626.

Hertel, Klemens J (2008) Combinatorial control of exon recognition. *Journal of Biological Chemistry* 283(3), pp. 1211–1215.

Hirschhorn, Joel N et al. (1992) Evidence that SNF2/SWI2 and SNF5 activate transcription in yeast by altering chromatin structure. *Genes & development* 6(12a), pp. 2288–2298.

Hnilicová, Jarmila et al. (2011) Histone deacetylase activity modulates alternative splicing. *PloS one* 6(2), e16727.

Ho, C Kiong and Stewart Shuman (1999) Distinct roles for CTD Ser-2 and Ser-5 phosphorylation in the recruitment and allosteric activation of mammalian mRNA capping enzyme. *Molecular cell* 3(3), pp. 405–411.

Ho, Lena et al. (2009) An embryonic stem cell chromatin remodeling complex, esBAF, is essential for embryonic stem cell self-renewal and pluripotency. *Proceedings of the National Academy of Sciences* 106(13), pp. 5181–5186.

Hodson, Mark J et al. (2012) The transition in spliceosome assembly from complex E to complex A purges surplus U1 snRNPs from alternative splice sites. *Nucleic acids research*, gks322.

Horn, Henning F (2014) LINC Complex Proteins in Development and Disease. *Curt Top Dev Biol* 109, pp. 287–321.

Horowitz, David S (2012) The mechanism of the second step of pre-mRNA splicing. *Wiley Interdisciplinary Reviews: RNA* 3(3), pp. 331–350.

Hoyal, Carolyn R et al. (2005) Genetic polymorphisms in DPF3 associated with risk of breast cancer and lymph node metastases. *Journal of carcinogenesis* 4(1). DOI: 10.1186/1477-3163-4-13.

Hsin, Jing-Ping and James L Manley (2012) The RNA polymerase II CTD coordinates transcription and RNA processing. *Genes & development* 26(19), pp. 2119–2137.

Huang, Huan et al. (2012) Nucleosome organization in sequences of alternative events in human genome. *Biosystems* 109(2), pp. 214–219.

Ip, Joanna Y et al. (2011) Global impact of RNA polymerase II elongation inhibition on alternative splicing regulation. *Genome research* 21(3), pp. 390–401.

Ishizaka, Aya et al. (2012) Double plant homeodomain (PHD) finger proteins DPF3a and-3b are required as transcriptional co-activators in SWI/SNF complex-dependent activation of NF-κB RelA/p50 heterodimer. *Journal of Biological Chemistry* 287(15), pp. 11924–11933.

Jasnovidova, Olga and Richard Stefl (2013) The CTD code of RNA polymerase II: a structural view. *Wiley Interdisciplinary Reviews: RNA* 4(1), pp. 1–16.

Jimeno-González, Silvia et al. (2015) Defective histone supply causes changes in RNA polymerase II elongation rate and cotranscriptional pre-mRNA splicing. *Proceedings of the National Academy of Sciences* 12(48), pp. 14840–14845.

Jonkers, Iris and John T Lis (2015) Getting up to speed with transcription elongation by RNA polymerase II. *Nature Reviews Molecular Cell Biology* 16, pp. 167–177.

Kaeser, Matthias D et al. (2008) BRD7, a novel PBAF-specific SWI/SNF subunit, is required for target gene activation and repression in embryonic stem cells. *Journal of Biological Chemistry* 283(47), pp. 32254–32263.

Karlić, Rosa et al. (2010) Histone modification levels are predictive for gene expression. *Proceedings of the National Academy of Sciences* 107(7), pp. 2926–2931.

Katz, Yarden et al. (2010) Analysis and design of RNA sequencing experiments for identifying isoform regulation. *Nature methods* 7(12), pp. 1009–1015.

Kaynak, Bogac et al. (2003) Genome-wide array analysis of normal and malformed human hearts. *Circulation* 107(19), pp. 2467–2474.

Keren, Hadas, Galit Lev-Maor, and Gil Ast (2010) Alternative splicing and evolution: diversification, exon definition and function. *Nature Reviews Genetics* 11(5), pp. 345–355.

Kielkopf, Clara L et al. (2001) A novel peptide recognition mode revealed by the X-ray structure of a core U2AF 35/U2AF 65 heterodimer. *Cell* 106(5), pp. 595–605.

Kim, Daehwan et al. (2013) TopHat2: accurate alignment of transcriptomes in the presence of insertions, deletions and gene fusions. *Genome Biol* 14(4), R36.

Kireeva, Natashe et al. (2004) Visualization of early chromosome condensation a hierarchical folding, axial glue model of chromosome structure. *The Journal of cell biology* 166(6), pp. 775–785.

Knöll, Ralph, Byambajav Buyandelger, et al. (2011) The sarcomeric Z-disc and Z-discopathies. *BioMed Research International* 2011, Article ID 569628.

Kobirumaki-Shimozawa, Fuyu et al. (2012) Sarcomere imaging by quantum dots for the study of cardiac muscle physiology. *BioMed Research International* 2012, Article ID 313814.

Kolasinska-Zwierz, Paulina et al. (2009) Differential chromatin marking of introns and expressed exons by H3K36me3. *Nature genetics* 41(3), pp. 376–381.

König, Harald et al. (2007) Splicing segregation: the minor spliceosome acts outside the nucleus and controls cell proliferation. *Cell* 131(4), pp. 718–729.

Kornblihtt, Alberto R et al. (2009) When chromatin meets splicing. *Nature structural & molecular biology* 16(9), pp. 902–903.

Kralovicova, Jana et al. (2015) Identification of U2AF (35)-dependent exons by RNA-Seq reveals a link between 3' splice-site organization and activity of U2AF-related proteins. *Nucleic acids research* 43(7), pp. 3747–3763.

Laggerbauer, Bernhard, Tilmann Achsel, and Reinhard Lührmann (1998) The human U5-200kD DEXH-box protein unwinds U4/U6 RNA duplices in vitro. *Proceedings of the National Academy of Sciences* 95(8), pp. 4188–4192.

Lange, Martin et al. (2008) Regulation of muscle development by DPF3, a novel histone acetylation and methylation reader of the BAF chromatin remodeling complex. *Genes & development* 22(17), pp. 2370–2384.

Lardelli, Rea M et al. (2010) Release of SF3 from the intron branchpoint activates the first step of pre-mRNA splicing. *Rna* 16(3), pp. 516–528.

Lehman, William et al. (2009) Structural basis for the activation of muscle contraction by troponin and tropomyosin. *Journal of molecular biology* 388(4), pp. 673–681.

Lessard, Julie et al. (2007) An essential switch in subunit composition of a chromatin remodeling complex during neural development. *Neuron* 55(2), pp. 201–215.

Liautard, Jean-Pierre et al. (1982) Structural organization of ribonucleoproteins containing small nuclear RNAs from HeLa cells: Proteins interact closely with a similar structural domain of U1, U2, U4 and U5 small nuclear RNAs. *Journal of molecular biology* 162(3), pp. 623–643.

Lim, Sharlene R and Klemens J Hertel (2004) Commitment to splice site pairing coincides with A complex formation. *Molecular cell* 15(3), pp. 477–483.

Linke, Wolfgang A and Nazha Hamdani (2014) Gigantic Business Titin Properties and Function Through Thick and Thin. *Circulation research* 114(6), pp. 1052–1068.

Liu, Hang et al. (2014) Expression profiles of HA117 and its neighboring gene DPF3 in different colon segments of Hirschsprung's disease. *International journal of clinical and experimental pathology* 7(7), pp. 3966–3974.

Liu, Yen-Chi and Soo-Chen Cheng (2015) Functional roles of DExD/H-box RNA helicases in Pre-mRNA splicing. *Journal of biomedical science* 22(1), pp. 1–9.

Loomis, Rebecca J et al. (2009) Chromatin binding of SRp20 and ASF/SF2 and dissociation from mitotic chromosomes is modulated by histone H3 serine 10 phosphorylation. *Molecular cell* 33(4), pp. 450–461.

Luco, Reini F, Mariano Allo, et al. (2011) Epigenetics in alternative pre-mRNA splicing. *Cell* 144(1), pp. 16–26.

Luco, Reini F, Qun Pan, et al. (2010) Regulation of alternative splicing by histone modifications. *Science* 327(5968), pp. 996–1000.

Lykke-Andersen, Søren and Torben Heick Jensen (2015) Nonsense-mediated mRNA decay: an intricate machinery that shapes transcriptomes. *Nature Reviews Molecular Cell Biology*.

Lynch, Gordon S, Camdon J Fary, and David A Williams (1997) Quantitative measurement of resting skeletal muscle [Ca 2+] i following acute and long-term downhill running exercise in mice. *Cell calcium* 22(5), pp. 373–383.

Makarov, Evgeny M et al. (2002) Small nuclear ribonucleoprotein remodeling during catalytic activation of the spliceosome. *Science* 298(5601), pp. 2205–2208.

Makarova, Olga V, Evgeny M Makarov, Sunbin Liu, et al. (2002) Protein 61K, encoded by a gene (PRPF31) linked to autosomal dominant retinitis pigmentosa, is required for U4/U6· U5 tri-snRNP formation and pre-mRNA splicing. *The EMBO journal* 21(5), pp. 1148–1157.

Makarova, Olga V, Evgeny M Makarov, Henning Urlaub, et al. (2004) A subset of human 35S U5 proteins, including Prp19, function prior to catalytic step 1 of splicing. *The EMBO journal* 23(12), pp. 2381–2391.

Maor, Galit Lev, Ahuvi Yearim, and Gil Ast (2015) The alternative role of DNA methylation in splicing regulation. *Trends in Genetics* 31(5), pp. 274–280.

Mata, Manuel de la and Alberto R Kornblihtt (2006) RNA polymerase II C-terminal domain mediates regulation of alternative splicing by SRp20. *Nature structural & molecular biology* 13(11), pp. 973–980.

Mathew, Rebecca et al. (2008) Phosphorylation of human PRP28 by SRPK2 is required for integration of the U4/U6-U5 tri-snRNP into the spliceosome. *Nature structural & molecular biology* 15(5), pp. 435–443.

Maunakea, Alika K et al. (2013) Intragenic DNA methylation modulates alternative splicing by recruiting MeCP2 to promote exon recognition. *Cell research* 23(11), pp. 1256–1269.

Mefford, Melissa A and Jonathan P Staley (2009) Evidence that U2/U6 helix I promotes both catalytic steps of pre-mRNA splicing and rearranges in between these steps. *Rna* 15(7), pp. 1386–1397.

Meijler, FL and TD Meijler (2011) Archetype, adaptation and the mammalian heart. *Netherlands Heart Journal* 19(3), pp. 142–148.

Morris, Daniel P and Arno L Greenleaf (2000) The splicing factor, Prp40, binds the phosphorylated carboxyl-terminal domain of RNA polymerase II. *Journal of Biological Chemistry* 275(51), pp. 39935–39943.

Murakami, Kenji et al. (2013) Architecture of an RNA polymerase II transcription preinitiation complex. *Science* 342(6159),

Naftelberg, Shiran et al. (2015) Regulation of alternative splicing through coupling with transcription and chromatin structure. *Annual review of biochemistry* 84, pp. 165–198.

Napolitano, Giuliana, Luigi Lania, and Barbara Majello (2014) RNA polymerase II CTD modifications: How many tales from a single tail. *Journal of cellular physiology* 229(5), pp. 538–544.

Naya, Francisco J et al. (2002) Mitochondrial deficiency and cardiac sudden death in mice lacking the MEF2A transcription factor. *Nature medicine* 8(11), pp. 1303–1309.

Neigeborn, Lenore and Marian Carlson (1984) Genes affecting the regulation of SUC2 gene expression by glucose repression in Saccharomyces cerevisiae. *Genetics* 108(4), pp. 845–858.

Neish, Andrew S et al. (1998) Factors associated with the mammalian RNA polymerase II holoenzyme. *Nucleic acids research* 26(3), pp. 847–853.

Ninkina, Natalia N et al. (2001) Cerd4, third member of the d4 gene family: expression and organization of genomic locus. *Mammalian Genome* 12(11), pp. 862–866.

Noguchi, S et al. (2005) Gene expression analyses in X-linked myotubular myopathy. *Neurology* 65(5), pp. 732–737.

Oberstrass, Florian C et al. (2005) Structure of PTB bound to RNA: specific binding and implications for splicing regulation. *Science* 309(5743), pp. 2054–2057.

Ochala, Julien et al. (2013) Skeletal and cardiac α-actin isoforms differently modulate myosin cross-bridge formation and myofibre force production. *Human molecular genetics* 22(21), pp. 4398–4404.

Olivetti, Giorgio et al. (1996) Aging, cardiac hypertrophy and ischemic cardiomyopathy do not affect the proportion of mononucleated and multinucleated myocytes in the human heart. *Journal of molecular and cellular cardiology* 28(7), pp. 1463–1477.

Ordahl, Charles P (1986) The skeletal and cardiac α-action genes are coexpressed in early embryonic striated muscle. *Developmental biology* 117(2), pp. 488–492.

Ottenheijm, Coen AC and Henk Granzier (2010) New insights into the structural roles of nebulin in skeletal muscle. *BioMed Research International* 2010, Article ID 968139.

Pacheco, Teresa R et al. (2006) In vivo requirement of the small subunit of U2AF for recognition of a weak 3' splice site. *Molecular and cellular biology* 26(21), pp. 8183–8190.

Pan, Qun et al. (2008) Deep surveying of alternative splicing complexity in the human transcriptome by high-throughput sequencing. *Nature genetics* 40(12), pp. 1413–1415.

Patrick, Kristin L et al. (2015) Genetic Interaction Mapping Reveals a Role for the SWI/SNF Nucleosome Remodeler in Spliceosome Activation in Fission Yeast. *PLoS genetics* 11(3), e1005074.

Perriman, Rhonda et al. (2003) ATP requirement for Prp5p function is determined by Cus2p and the structure of U2 small nuclear RNA. *Proceedings of the National Academy of Sciences* 100(24), pp. 13857–13862.

Porrua, Odil and Domenico Libri (2015) Transcription termination and the control of the transcriptome: why, where and how to stop. *Nature Reviews Molecular Cell Biology* 16, pp. 190–202.

Potgieter, FJ and PI Wilke (1997) Effect of different bedding materials on the reproductive performance of mice. *Journal of the South African Veterinary Association* 68(1), pp. 8–15.

Pradeepa, Madapura M et al. (2012) Psip1/Ledgf p52 binds methylated histone H3K36 and splicing factors and contributes to the regulation of alternative splicing. *PLoS Genet* 8(5), e1002717.

Puig, Oscar et al. (2001) The tandem affinity purification (TAP) method: a general procedure of protein complex purification. *Methods* 24(3), pp. 218–229.

Rayment, Ivan et al. (1993) Three-dimensional structure of myosin subfragment-1: a molecular motor. *Science* 261(5117), pp. 50–58.

Rhode, Britta M et al. (2006) Proximity of conserved U6 and U2 snRNA elements to the 5' splice site region in activated spliceosomes. *The EMBO journal* 25(11), pp. 2475–2486.

Rosano, Germán L and Eduardo A Ceccarelli (2014) Recombinant protein expression in Escherichia coli: advances and challenges. *Frontiers in microbiology* 5, pp. 172.1–172.17.

Rothbart, Scott B and Brian D Strahl (2014) Interpreting the language of histone and DNA modifications. *Biochimica et Biophysica Acta (BBA)-Gene Regulatory Mechanisms* 1839(8), pp. 627–643.

Rybak-Wolf, Agnieszka et al. (2015) Circular RNAs in the mammalian brain are highly abundant, conserved, and dynamically expressed. *Molecular cell* 58(5), pp. 870–885.

Sainsbury, Sarah, Carrie Bernecky, and Patrick Cramer (2015) Structural basis of transcription initiation by RNA polymerase II. *Nature Reviews Molecular Cell Biology* 16(3), pp. 129–143.

Sanchez, Sabrina E et al. (2010) A methyl transferase links the circadian clock to the regulation of alternative splicing. *Nature* 468(7320), pp. 112–116.

Schiaffino, Stefano and Carlo Reggiani (2011) Fiber types in mammalian skeletal muscles. *Physiological reviews* 91(4), pp. 1447–1531.

Schmidt-Supprian, Marc and Klaus Rajewsky (2007) Vagaries of conditional gene targeting. *Nature immunology* 8(7), pp. 665–668.

Schwartz, Schraga, Eran Meshorer, and Gil Ast (2009) Chromatin organization marks exon-intron structure. *Nature structural & molecular biology* 16(9), pp. 990–995.

Schwenk, Frieder, Udo Baron, and Klaus Rajewsky (1995) A cre-transgenic mouse strain for the ubiquitous deletion of loxP-flanked gene segments including deletion in germ cells. *Nucleic acids research* 23(24), p. 5080.

Schwer, Beate (2008) A conformational rearrangement in the spliceosome sets the stage for Prp22-dependent mRNA release. *Molecular cell* 30(6), pp. 743–754.

Schwer, Beate and Christine Guthrie (1992) A conformational rearrangement in the spliceosome is dependent on PRP16 and ATP hydrolysis. *The EMBO journal* 11(13), pp. 5033–5039.

Scott, Wayne, Jennifer Stevens, and Stuart A Binder–Macleod (2001) Human skeletal muscle fiber type classifications. *Physical therapy* 81(11), pp. 1810–1816.

Selenko, Philipp et al. (2003) Structural basis for the molecular recognition between human splicing factors U2AF 65 and SF1/mBBP. *Molecular cell* 11(4), pp. 965–976.

Seyedali, Ali and Marla J Berry (2014) Nonsense-mediated decay factors are involved in the regulation of selenoprotein mRNA levels during selenium deficiency. *rna*.

Shao, Wei et al. (2012) A U1-U2 snRNP interaction network during intron definition. *Molecular and cellular biology* 32(2), pp. 470–478.

Shen, Haihong et al. (2008) Distinct activities of the DExD/H-box splicing factor hUAP56 facilitate stepwise assembly of the spliceosome. *Genes & development* 22(13), pp. 1796–1803.

Shepard, Peter J et al. (2011) Efficient internal exon recognition depends on near equal contributions from the 3' and 5' splice sites. *Nucleic acids research*, gkr481.

Shindo, Yuki et al. (2013) Computational analysis of associations between alternative splicing and histone modifications. *FEBS letters* 587(5), pp. 516–521.

Shukla, Sanjeev et al. (2011) CTCF-promoted RNA polymerase II pausing links DNA methylation to splicing. *Nature* 479(7371), pp. 74–79.

Sims, Robert J et al. (2007) Recognition of trimethylated histone H3 lysine 4 facilitates the recruitment of transcription postinitiation factors and pre-mRNA splicing. *Molecular cell* 28(4), pp. 665–676.

Spartz, Angela K, Robert K Herman, and Jocelyn E Shaw (2004) SMU-2 and SMU-1, Caenorhabditis elegans homologs of mammalian spliceosome-associated proteins RED and fSAP57, work together to affect splice site choice. *Molecular and cellular biology* 24(15), pp. 6811–6823.

Spitzer, Jessica et al. (2014) PAR-CLIP (Photoactivatable Ribonucleoside-Enhanced Crosslinking and Immunoprecipitation): a step-by-step protocol to the transcriptome-wide identification of binding sites of RNA-binding proteins. *Methods in enzymology* 539, pp. 113–161.

Spudich, James A and Susan Watt (1971) The regulation of rabbit skeletal muscle contraction I. Biochemical studies of the interaction of the tropomyosin-troponin complex with actin and the proteolytic fragments of myosin. *Journal of Biological Chemistry* 246(15), pp. 4866–4871.

Staknis, David and Robin Reed (1994) SR proteins promote the first specific recognition of Pre-mRNA and are present together with the U1 small nuclear ribonucleoprotein particle in a general splicing enhancer complex. *Molecular and Cellular Biology* 14(11), pp. 7670–7682.

Staley, Jonathan P and Christine Guthrie (1999) An RNA switch at the 5' splice site requires ATP and the DEAD box protein Prp28p. *Molecular cell* 3(1), pp. 55–64.

Stelzl, Ulrich et al. (2005) A human protein-protein interaction network: a resource for annotating the proteome. *Cell* 122(6), pp. 957–968.

Stern, Michael, Robert Jensen, and Ira Herskowitz (1984) Five SWI genes are required for expression of the HO gene in yeast. *Journal of molecular biology* 178(4), pp. 853–868.

Sullivan, E Kelly et al. (2001) Transcriptional activation domains of human heat shock factor 1 recruit human SWI/SNF. *Molecular and cellular biology* 21(17), pp. 5826–5837.

Tando, Toshio et al. (2010) Requiem protein links RelB/p52 and the Brm-type SWI/SNF complex in a noncanonical NF-κB pathway. *Journal of Biological Chemistry* 285(29), pp. 21951–21960.

Theodorou, Marina et al. (2013) Identification of a STAT5 target gene, Dpf3, provides novel insights in chronic lymphocytic leukemia. *PloS one* 8(10), e76155.

Tilgner, Hagen et al. (2009) Nucleosome positioning as a determinant of exon recognition. *Nature structural & molecular biology* 16(9), pp. 996–1001.

Trapnell, Cole et al. (2010) Transcript assembly and quantification by RNA-Seq reveals unannotated transcripts and isoform switching during cell differentiation. *Nature biotechnology* 28(5), pp. 511–515.

Trcek, Tatjana et al. (2013) Temporal and spatial characterization of nonsense-mediated mRNA decay. *Genes & development* 27(5), pp. 541–551.

Tsai, Rong-Tzong et al. (2005) Spliceosome disassembly catalyzed by Prp43 and its associated components Ntr1 and Ntr2. *Genes & development* 19(24), pp. 2991–3003.

Tufarelli, Cristina et al. (2001) Characterization of a widely expressed gene (LUC7-LIKE; LUC7L) defining the centromeric boundary of the human α-globin domain. *Genomics* 71(3), pp. 307–314.

Tyagi, Anu et al. (2009) SWI/SNF associates with nascent pre-mRNPs and regulates alternative pre-mRNA processing. *PLoS Genet* 5(5), e1000470.

Uetz, Peter et al. (2006) Herpesviral protein networks and their interaction with the human proteome. *Science* 311(5758), pp. 239–242.

Venkatesh, Swaminathan and Jerry L Workman (2015) Histone exchange, chromatin structure and the regulation of transcription. *Nature Reviews Molecular Cell Biology* 16, pp. 178–189.

Vieira, Alexandre R et al. (2008) Candidate gene/loci studies in cleft lip/palate and dental anomalies finds novel susceptibility genes for clefts. *Genetics in Medicine* 10(9), pp. 668–674.

Wahl, Markus C, Cindy L Will, and Reinhard Lührmann (2009) The spliceosome: design principles of a dynamic RNP machine. *Cell* 136(4), pp. 701–718.

Waldholm, Johan et al. (2011) SWI/SNF regulates the alternative processing of a specific subset of pre-mRNAs in Drosophila melanogaster. *BMC molecular biology* 12(1), article 46.

Wang, Eric T et al. (2008) Alternative isoform regulation in human tissue transcriptomes. *Nature* 456(7221), pp. 470–476.

Wang, Magnus and Antonio Marín (2006) Characterization and prediction of alternative splice sites. *Gene* 366(2), pp. 219–227.

Wang, W et al. (1996) Purification and biochemical heterogeneity of the mammalian SWI-SNF complex. *The EMBO journal* 15(19), pp. 5370–5382.

Wang, Yue-Xiang et al. (2005) Requirements of myocyte-specific enhancer factor 2A in zebrafish cardiac contractility. *FEBS letters* 579(21), pp. 4843–4850.

Warkocki, Zbigniew et al. (2009) Reconstitution of both steps of Saccharomyces cerevisiae splicing with purified spliceosomal components. *Nature structural & molecular biology* 16(12), pp. 1237–1243.

Wernig, A, A Irintchev, and P Weisshaupt (1990) Muscle injury, cross-sectional area and fibre type distribution in mouse soleus after intermittent wheel-running. *The Journal of physiology* 428(1), pp. 639–652.

Will, Cindy L and Reinhard Lührmann (2011) Spliceosome structure and function. *Cold Spring Harbor perspectives in biology* 3(7), a003707.

Will, Cindy L, Henning Urlaub, et al. (2002) Characterization of novel SF3b and 17S U2 snRNP proteins, including a human Prp5p homologue and an SF3b DEAD-box protein. *The EMBO journal* 21(18), pp. 4978–4988.

Wilson, Christopher J et al. (1996) RNA polymerase II holoenzyme contains SWI/SNF regulators involved in chromatin remodeling. *Cell* 84(2), pp. 235–244.

Wilson, Don E and DeeAnn M Reeder (2005) *Mammal species of the world: a taxonomic and geographic reference*. Vol. 12. JHU Press.

Wlodaver, Alissa M and Jonathan P Staley (2014) The DExD/H-box ATPase Prp2p destabilizes and proofreads the catalytic RNA core of the spliceosome. *RNA* 20(3), pp. 282–294.

Wood, Lauren K et al. (2014) Intrinsic stiffness of extracellular matrix increases with age in skeletal muscles of mice. *Journal of Applied Physiology* 117(4), pp. 363–369.

Worseck, Josephine M et al. (2012) A Stringent Yeast Two-Hybrid Matrix Screening Approach for Protein–Protein Interaction Discovery. In: *Two Hybrid Technologies*. Springer, pp. 63–87.

Wyatt, JR, EJ Sontheimer, and JA Steitz (1992) Site-specific cross-linking of mammalian U5 snRNP to the 5'splice site before the first step of pre-mRNA splicing. *Genes & Development* 6(12b), pp. 2542–2553.

Yearim, Ahuvi et al. (2015) HP1 is involved in regulating the global impact of DNA methylation on alternative splicing. *Cell reports* 10(7), pp. 1122–1134.

Yeo, Gene and Christopher B Burge (2004) Maximum entropy modeling of short sequence motifs with applications to RNA splicing signals. *Journal of Computational Biology* 11(2-3), pp. 377–394.

Yuan, R, CJ Rosen, and WG Beamer (2012) *Aging study: IGF-1 and body weight for 33 inbred strains of mice. MPD:Yuan1*. Mouse Phenome Database web site, The Jackson Laboratory, Bar Harbor, Maine USA. URL: `http://phenome.jax.org` (visited on 11/10/2015).

Zeng, Lei et al. (2010) Mechanism and regulation of acetylated histone binding by the tandem PHD finger of DPF3b. *Nature* 466(7303), pp. 258–262.

Zhang, Wei et al. (2011) Crystal structure of the Cys2His2-type zinc finger domain of human DPF2. *Biochemical and biophysical research communications* 413(1), pp. 58–61.

Zhou, Hua-Lin et al. (2014) Regulation of alternative splicing by local histone modifications: potential roles for RNA-guided mechanisms. *Nucleic acids research* 42(2), pp. 701–713.

Zhu, Shijia et al. (2013) Modeling exon expression using histone modifications. *PloS one* 8(6), e67448.

Zraly, Claudia B and Andrew K Dingwall (2012) The chromatin remodeling and mRNA splicing functions of the Brahma (SWI/SNF) complex are mediated by the SNR1/SNF5 regulatory subunit. *Nucleic acids research* 40(13), pp. 5975–5987.

8 Curriculum vitae

For reasons of data protection, the Curriculum vitae is not published in the online version.

9 Appendix

9.1 Names of differentially expressed genes

Fold changes (FC) for protein coding genes were filtered for an FPKM value equal or larger than one in at least one condition. Genes with a fold change 1.5≤FC or FC ≤0.67 are listed in the following.

Downregulated genes in the left ventricle of Dpf3 knockout mice

1190002N15Rik, 2610305D13Rik, 3632451O06Rik, 3830403N18Rik, 4930430F08Rik, 49305-78C19Rik, 5730507C01Rik, 8030462N17Rik, 9030025P20Rik, Abcb1a, Abcb7, Abcd2, Acer3, Acsl4, Acta2, Agmo, Ahr, Akr1b8, Aldh1l2, Alg10b, Ammecr1, Ankrd45, Ap1s2, Ap3m1, Aph1b, Aqp11, Aqp4, Arl5a, Aspn, Atp11c, Atp6v0d2, Avl9, AW549877, B230219D22Rik, B3galt2, Bche, Bmpr1a, C1galt1, C3ar1, Cacna2d1, Calcrl, Casp1, Casp12, Cav2, Ccbe1, Ccdc126, Ccdc68, Ccl11, Ccnyl1, Ccr5, Cd180, Cd300ld, Cd36, Cd52, Cd53, Cd72, Cdc14a, Cdc27, Cenpp, Cetn3, Cfp, Chm, Chml, Clec12a, Clec4a1, Clec4a3, Clec7a, Cmah, Cnot6, Cog5, Col14a1, Crip1, Ctbs, Ctdspl2, Ctsc, Dcun1d1, Ddx26b, Ddx5, Dimt1, Dmxl1, Dock5, Dock7, Dpf3, Dpy19l1, E130311K13Rik, Ebi3, Emr1, Eny2, Eogt, Erp44, Evi2a, Fads2, Fam122b, Fam13b, Fam151a, Fam188a, Fam198b, Fam45a, Fam69a, Fam81a, Fcrls, Foxn2, Fv1, Galnt4, Gatm, Gbe1, Gca, Gch1, Gcnt1, Gda, Ggt5, Gm11837, Gm12657, Gm13157, Gm13212, Gm13251, Gm3646, Gm5113, Gm527, Gm5803, Gm7120, Gnai1, Gnpda2, Gpcpd1, Gpm6a, Gpr155, Gstm6, Gulp1, Haus2, Hecw2, Hils1, Hist1h2bj, Hpgd, Hpgds, Hs3st5, Hsd17b7, Ifi203, Ifi204, Ifit1, Ifit2, Igip, Il33, Inpp4b, Itgam, Itgb2, Kbtbd3, Kcne1, Kctd11, Kctd12, Kctd12b, Klhl28, Klhl6, Krt222, Lactb2, Lcp1, Lims1, Lin54, Lpar6, Lrrc17, Lrrcc1, Lst1, Lyve1, Man2a1, Manea, Maob, Map2k6, Mbnl2, Mboat2, Mettl4, Mfap3l, Micu3, Mme, Mmgt2, Mmp12, Mtx3, Myct1, Mylk4, Myo1e, NA, Naalad2, Nckap1l, Nebl, Nfkbiz, Nme5, Npat, Nxt2, Oas2, Ogn, OTTMUSG00000016609, OTTMUSG00000016609, P2ry14, Pde3b, Pde7a, Pde7b, Pdk3, Pfkfb1, Pggt1b, Pign, Pkd2l2, Plek, Plk2, Pln, Polk, Pp2d1, Ppbp, Ppm1e, Prex2, Prkaa1, Prrg1, Pter, Ptplad2, Ptpn6, Ptprj, Pycard, Rab8b, Ramp1, Rapgef5, Rasgrp3, Rassf9, Raver2, Rbm26, Rgs5, Rgs7bp,

Rhobtb3, Rnf170, Rp2h, Rpa3, Rps6ka3, Runx1t1, S100a8, Sacm1l, Samd9l, Scai, Scyl2, Sema3c, Sh3bgrl, Slamf9, Slc16a7, Slc25a36, Slc25a40, Slc2a12, Slc35a3, Slc36a4, Slc39a10, Slc4a7, Sp3, Sp4, St6gal1, St8sia4, Stt3a, Stxbp6, Sycp3, Tbl1x, Tfrc, Tgif1, Tirap, Tlr4, Tmem176a, Tmem29, Tmem35, Tmem47, Tmx3, Trappc8, Tslp, Tspan12, Tspan6, Ttc14, Ube2w, Uhmk1, Upk3b, Vcan, Vcpip1, Vma21, Vps26a, Wif1, Xirp2, Zbtb33, Zfp101, Zfp217, Zfp35, Zfp518a, Zfp644, Zfp72, Zfp759, Zfp800, Zfp868, Zfp931, Zfp946, Zfp947, Zfp951, Zfp958

Upregulated genes in the left ventricle of Dpf3 knockout mice

1700020L24Rik, 1700056E22Rik, 1810043H04Rik, 2200002D01Rik, 2310030G06Rik, 23100-33P09Rik, 2310036O22Rik, 2310039H08Rik, 2810428I15Rik, 3110040N11Rik, 6030419C18-Rik, 8430408G22Rik, Abhd1, Ablim3, Acbd6, Acsm5, Acta1, Adamtsl2, Adck4, AI413582, Akap5, Amdhd2, Anapc13, Anxa13, Arhgap9, Armc5, Aspscr1, Atf5, Aurkaip1, B3gat3, B4galt3, B930041F14Rik, Bad, Bbc3, Bcl7c, Bdh1, Bmyc, Bola1, Bola2, Bri3, Cacna1g, Cacna1h, Cadm4, Casq1, Ccdc107, Ccdc124, Ccdc86, Ccl27a, Ccl5, Cdc42ep5, Cdh4, Cebpd, Cfd, Chpf, Cited4, Cks1b, Cnksr1, Cntfr, Col7a1, Cox17, Cox5b, Cpxm2, Crocc, Csrnp1, Cyb561d2, Dalrd3, Dcxr, Ddit4, Ddrgk1, Defb8, Dnajb1, Drap1, Dusp12, Enho, Ephb3, Epn1, Epn3, Epor, Erf, Exosc6, F830016B08Rik, Fam129b, Fam132a, Fam98c, Fbrsl1, Fbxw9, Fgfrl1, Fhl3, Fkbp8, Fscn1, Fxyd2, G0s2, Gadd45g, Gbp10, Gbp6, Glrx5, Gm13889, Gm14378, Gm1673, Gm3776, Gm4841, Gnb3, Gnmt, Gpx1, Grcc10, Gsg1l, Gsk3a, Gsta1, Gtf2ird2, Gtpbp6, H2-K1, H2-Q4, H2-Q7, H2-Q8, H2afx, Hamp, Hcfc1r1, Helt, Hgs, Higd2a, Hist1h2ao, Hist1h2ao, Hist2h2aa2, Hist2h2aa2, Hist2h3c2, Hspb2, Id3, Ier2, Ift27, Igfals, Igsf23, Igtp, Il17rc, Inha, Ino80e, Isyna1, Jak3, Klf2, Klhl36, Lad1, Lamb3, Lamtor4, Lars2, Lcn2, Llgl2, Lmna, Lrrc4b, Lrrc52, Lrrc71, Lsm2, Mafg, Marcksl1, Mea1, Med11, Med22, Metrn, Mettl22, Mfsd12, Mgmt, Mib2, Mien1, Mrpl14, Mrpl52, Mrpl54, Mrpl55, Mt1, Mt2, Mybphl, Myeov2, Myl7, Nabp2, Ndufa13, Ndufb10, Ndufb2, Ndufs6, Nfkbil1, Nkx2-5, Nme3, Nppa, Nr2f6, Nr4a1, Nudt14, Nudt9, Numbl, Obsl1, Ocel1, Otud1, Pacsin3, Pagr1a, Pcbd1, Pdk4, Pelo, Per1, Pgls, Pgp, Phlda1, Pigv, Pih1d1, Pkdcc, Plac9b, Plac9b, Plac9b, Ppan, Ppp1r13l, Ppp1r14a, Ppp1r1b, Prmt2, Psmb8, Ptms, Ptov1, Ptrh1, Pura, Pvrl2, Pycr2, Rab40b, Rasd1, Rccd1, Rhbdd3, Rhbdl1, Rhebl1, Rhod, Rhpn2, Rnaseh2c, Rom1, Rpl31-ps12, Rpl36al, Rplp1, Rpp25l, Rps15, Rps5, Rtn4r, Sac3d1, Sap30, Sbk3, Sbsn, Scand1, Scd4, Scgb1c1, Scn1b, Scn4b, Scx, Sec61b, Selm, Sema6c, Sh3rf2, Shfm1, Sik1, Slc12a9, Slc17a7, Slc25a22, Slc2a1, Sln, Smagp, Smim12, Snai1, Snrnp35, Spsb2, Stap2, Stard10, Tap1, Tbcb, Tesc, Tfeb, Tfpt, Thap3, Tmem116, Tmem132a, Tmem160, Tmem191c, Tmem200b, Tmem238, Tmem9, Tmsb10, Tmub1, Tnnt1, Tnrc6b, Tomm6, Tpm2, Tradd, Trappc6a, Trim8, Trp53i13, Trpv4, Tsen54, Tsfm, Tsr3, Tysnd1, Ube2t,

Ubxn10, Ucp2, Unc119, Uqcr11, Ush1c, Vmn2r55, Wdr6, Wrap53, Xcr1, Yif1b, Zbtb12, Zfp36, Zfp428, Zfp707, Zfp771, Znhit2

Downregulated genes in the right ventricle of Dpf3 knockout mice

1600002H07Rik, 3830403N18Rik, 4930503L19Rik, Adam8, Agmo, Ahr, Alox5ap, Ammecr1, Ankrd63, Anpep, Aoah, Apobec1, Arhgap19, Aspa, Atp6v0d2, Atpif1, B4galnt1, BC028528, Bcl2a1b, Blnk, Bmp2k, C3, C3ar1, C4b, Cadm1, Ccl11, Ccl5, Ccne2, Cd180, Cd300ld, Cd300lh, Cd33, Cd37, Cd4, Cd44, Cd48, Cd52, Cd53, Cd68, Cd72, Cd83, Cd84, Chst4, Clec12a, Clec4a1, Clec7a, Crip1, Ctss, Cybb, Cyth4, Ddx5, Derl2, Dpf3, Dse, Ece2, Emr1, Enpp1, Evi2a, F8a, Fabp5, Fam111a, Fam65a, Fam65b, Fam81a, Fbxo36, Fcgr3, Fcgr4, Fcrls, Gcnt1, Glipr1, Gm11710, Gm11711, Gm12657, Gm13212, Gm14548, Gm20594, Gm-527, Gm5803, Gm684, Gng2, Gp49a, Gpm6b, Gpnmb, Gpr137b, Gpr34, H3f3a, Hbb-bt, Hecw2, Hexb, Hist1h2bj, Hist1h4h, Hpgds, Hpse, Hsd17b7, Ifi204, Itgam, Itgb2, Kctd12b, Lacc1, Laptm5, Lcp1, Lgi2, Lilra5, Lilrb4, Lpar6, Lypd2, Lyz2, Map1lc3a, Mcpt4, Mdk, Mertk, Mmp12, Mpeg1, Ms4a7, Nckap1l, Nhlrc3, Nmb, Nrros, Olfr613, P2ry14, Pde7a, Pfkfb1, Pianp, Pid1, Pirb, Plek, Plxnc1, Pnp2, Pp2d1, Prex1, Ptafr, Ptprc, Qpct, Retnla, Rgs7, Riiad1, Rpl22l1, Rps17, Rps3, Runx1t1, S100a8, S1pr2, Sco2, Slc10a7, Slc2a12, Slc37a2, Slc7a2, Slc9a9, Soat1, Spp1, Stt3a, Taf6l, Tctn1, Tfrc, Themis2, Tlr13, Tlr2, Tlr7, Tm6sf1, Tmem231, Tnfrsf1b, Tslp, Tyrobp, Uap1l1, Ugt1a2, Upk1b, Wfdc17, Wif1, Xlr, Zbtb16, Zeb2os, Zfp938

Upregulated genes in the right ventricle of Dpf3 knockout mice

1700020L24Rik, 1810043H04Rik, 2010015L04Rik, 2210407C18Rik, 2310007L24Rik, 231000-9B15Rik, 2310030G06Rik, 2310036O22Rik, 2410004B18Rik, 3110040N11Rik, 3110082I17-Rik, Abra, Acsm5, Acta1, Adamtsl2, Akap5, Aldh16a1, Alyref2, Bcl7c, Bdh1, Bex4, Bloc1s3, C1qtnf4, Cacna1g, Cacna1h, Cadm4, Camk2b, Car15, Casq1, Ccdc86, Cd59b, Cdc34, Cdkl3, Cenpv, Cib1, Cideb, Clic3, Commd4, Cox5b, Cox8a, Cpxm2, Csrnp1, Cyfip2, Ddit4, Defb8, Deptor, Dhrs13, Drap1, Dusp5, Enkur, Ephb3, Epn3, Fam131a, Fbxl6, Fbxw9, Fgf16, Fgf2, Fhl3, Fkbp8, G0s2, Gbp6, Gck, Gemin6, Glrx5, Gltpd1, Gm11127, Gm3264, Gm4841, Gpam, Gpr27, Gsg1l, Gsta1, Gzmm, H2-Q8, Hipk2, Hist2h3c2, Hmgn5, Id1, Ier5l, Il17rc, Kazald1, Lad1, Lamtor4, Leng9, Lnx1, Lrrc4b, Lrrc51, Lrrc52, Lrrc71, Maff, Mlana, Mrps11, Mt2, Ndnl2, Ndufs6, Nfkbia, Nppb, Nr4a1, Ntn1, Otud1, Pcbd1, Pdk4, Penk, Pgp, Phlda1, Pkdcc, Pkn3, Plac9b, Plac9b, Plac9b, Plekha7, Ppan, Ppp1r1b, Prkcdbp, Prkcq, Prune2, Psph, Ptgds, Pygo1, Rab11fip5, Rab40b, Rasd1, Rdm1, Rhbdl1, Rhd, Rnaseh2c, Rnd2, Rom1, Rplp1, Rpp25l, Rtn1, Rtn4r, Scn1b, Scn4a, Scn4b, Serf1, Sfrp5,

Sh3rf2, Sik1, Slc16a13, Slc17a7, Slc25a25, Slc37a1, Smoc1, Spsb2, Stap2, Stk19, Tmem101, Tmem238, Tmem254a, Tmem254a, Tmem254a, Tnfrsf18, Tpgs1, Tpm2, Trappc6a, Tsen54, Tusc1, Ube2c, Ube2o, Ubxn10, Uchl4, Ush1c, Vrk3, Wtip, Zfp771, Zfp772

Downregulated genes in the skeletal muscle of Dpf3 knockout mice

1700037H04Rik, A530016L24Rik, Abhd14b, Acad12, Acat2, Acly, Adamtsl4, Alkbh4, Angptl7, Ankrd2, Aqp4, Arpp21, Atf5, Atp1b1, Atp2a3, Basp1, Bcl2, Casp2, Ccdc3, Ccnj, Cd163, Cd1d1, Cd52, Cd79a, Cdh4, Cdo1, Chst1, Cnn2, Csrp3, Ctsk, Cyp2f2, Darc, Dgat2, Dmkn, Dpf3, Dusp14, E130012A19Rik, Egln3, Elovl6, Emid1, Esrrb, Fads6, Fam212b, Fam25c, Fasn, Fgf2, Fhl1, Folr2, Foxo6, Frzb, Fxyd7, G0s2, Gabbr1, Gdf10, Gnai1, Golm1, Gpnmb, Grrp1, Grtp1, H2-Q10, H2-Q7, Hebp1, Hilpda, Hmgn3, Hoxa4, Hoxa5, Hp, I830012O16Rik, Iah1, Il12a, Il17d, Impa2, Irx5, Itgbl1, Klhl34, Krt10, Krtdap, Lce1m, Lfng, Lrrc17, Lrrn1, Ly6d, Mchr1, Mettl21e, Mfap4, Mid1ip1, Mmp11, Mmp3, Mrap, Msantd2, Mss51, Mup2, Musk, Myh6, Myh7, Myh7b, Myl10, Myl12a, Myl3, Myom3, Myoz2, Nanog, Nav2, Nnat, Nog, Nova1, Npr3, Nrm, Orm1, Padi2, Perp, Pf4, Pitx2, Plin3, Pnpla3, Postn, Pparg, Ptger3, Pth1r, Pygl, Rap2b, Rbpms, Retn, Rnase13, Rpusd1, Sbk2, Sbk3, Sbsn, Scd1, Ska2, Slc15a2, Slc16a2, Slc25a1, Slc25a10, Slc25a24, Slc25a30, Slc26a10, Sox7, Stab1, Sult5a1, Syp, Tgfb1, Thrsp, Tkt, Tnfrsf4, Tnmd, Ttc9, Uchl1, Vamp8, Vmn2r29, Vps37b, Xpo4, Zfp385a, Zfp503

Upregulated genes in the skeletal muscle of Dpf3 knockout mice

1700001O22Rik, 1810011O10Rik, 2310007L24Rik, 3110009E18Rik, 6030419C18Rik, 84304-08G22Rik, Actc1, Actr3b, Adamts1, AI118078, Arl4d, Arrdc3, Asb15, Atp1b4, Bola2, Bsg, Cacna2d4, Car14, Car2, Ccl5, Ccl8, Cd24a, Cd276, Cebpd, Ces1d, Chac1, Cks1b, Clu, Cntnap2, Csrnp1, Cst6, Cxcl14, Cyfip2, Cyp4f39, Cyr61, Dapp1, Ddit4, Ddx5, Dkk3, Dnase1, Dpm3, Dupd1, Dusp10, Epb4.1l5, Exoc7, F830016B08Rik, Fam19a3, Fam57b, Fbxo32, Fgfbp1, Fzd9, Gadd45g, Galr2, Gck, Gcnt2, Gm14288, Gm5803, Gpx3, Hist1h3d, Hscb, Hspb6, Htra4, Ifi30, Igtp, Irs1, Kazald1, Kcnab1, Kcnc3, Kcng4, Lars2, Lcn2, Leprel4, Lrtm2, Ly96, Map3k7cl, Mdga1, Me2, Mfsd7b, Mgmt, Mical2, Mrgprg, Mybph, Myh3, Myh8, Npc1, Npnt, Nrtn, Obsl1, Odf3l2, Ostn, Otub2, Pdk4, Pemt, Pfkfb3, Pla2g7, Plac9b, Plac9b, Plac9b, Ppp1r3c, Ptpn4, Rasd2, Rhpn2, Rom1, Rpl36al, Serpinb1c, Serpine1, Sesn1, Sfxn3, Sgk1, Shc2, Six2, Slc16a3, Slc25a22, Slc25a25, Slc38a4, Slc43a1, Slc7a2, Sox4, Sytl2, Tgif1, Thpo, Tiam1, Tmem132b, Tmem140, Tmem255b, Tmem37, Tnfrsf23, Trim63, Trp53inp1, Tsacc, Ttn, Ubc, Ucp3, Vgll3, Wfdc17, Xkrx, Ybx2, Zeb2, Zfp36

Downregulated genes in the siDpf3 knockdown sample (HL-1 cells)

1700007K13Rik, Ak4, Aldh3b1, Ankrd37, Apln, Apoc1, Arap2, Axl, B020004J07Rik, Bend4, Btg2, Casp7, Cd247, Cd274, Cd80, Ces2e, Ces2g, Cmtm6, Dennd1b, Dgat2, Dgka, Dhx58, Dpf3, Egln3, Elk3, Etnk1, Fam161a, Fam20b, Fbxo2, Fgf11, Fhl4, Fignl2, Gchfr, Gfpt2, Gm11544, Gm11992, Gm12794, Gm12942, Gm3258, Gm5595, Gnat1, Gnb3, Gpr135, Gramd1c, Gstm7, Hba-a2, Hmox1, Hs3st6, Icam1, Igf2, Igtp, Irf7, Irgm2, Isg15, Itgb2, Kbtbd11, Lgals3bp, Lrrc3b, Matn4, Mgat4a, Mob3b, Msi1, Myh13, Myom2, Nlrp10, Notch3, Oas1b, Oasl2, Olfr420, Plekha3, Plekhb2, Pnp, Podn, Pp2d1, Pramef25, Pros1, Ptprg, Rabl3, Rell1, Robo3, Rora, Rpl13a, Rprd1a, Samd9l, Scd2, Scgb3a1, Sh3bgrl2, Slc24a4, Slc25a35, Slc29a4, Slc37a2, Slc38a3, Slc7a4, Sp6, Spata6, Sprr1a, Tbc1d30, Them5, Tmem217, Tmem81, Tmem92, Tmod4, Tmtc4, Tnfrsf23, Tppp3, Trim12c, Trp53i11, Trp53inp1, Uhmk1, Usp17le, Usp18, Zbtb38, Zmat3, Zscan4b, Zscan4c, Zscan4d, Zscan4e, Zscan4f

Upregulated genes in the siDpf3 knockdown sample (HL-1 cells)

1190005I06Rik, 1500015O10Rik, 1700020L24Rik, 2210016F16Rik, 2310036O22Rik, 2410124-H12Rik, 2700094K13Rik, 4930404N11Rik, Abhd1, Ablim3, Acvr2b, Adcy1, Akap12, Akap5, Arhgdig, Bex1, Bmp4, Cbr2, Ccdc112, Cdk15, Cgnl1, Chrna1, Cox5b, Crygn, Ctgf, Cxcl1, Cxcr2, Fam171a2, Fance, Fbxo17, Fkbp8, Glipr2, Gm3417, Gm3448, Gm773, Gper1, Gstt1, Gtpbp6, Gtsf1, H1fx, H2afx, Hdhd3, Hist1h1c, Hist1h2ae, Hist1h2ag, Hist1h2bb, Hist1h2bg, Hist1h3c, Hist1h3g, Hist1h4a, Hist1h4b, Hist1h4d, Hist1h4h, Hist1h4k, Hist2h2aa2, Hist-2h2aa2, Hist2h2ac, Hist2h3c2, Hs3st1, Hspb11, Igf1, Il11, Il17d, Inhba, Lcmt2, Lctl, Lims2, Lmod1, Lrrc17, Lst1, Ly6k, Mamld1, Megf6, Metrn, Mex3d, Nanog, Ndufs6, Nppb, Nxf7, Olfml3, Olfr424, P2rx1, P4htm, Pcbp4, Pcp4, Pdlim7, Pfdn4, Pik3r6, Pilra, Pkdcc, Ppapdc3, Ppp1r14a, Prss23, Ptar1, Ptger1, Rpl31-ps12, Rplp1, Rpp25l, Scd3, Scgb1c1, Sec61b, Sectm1a, Sfrp5, Sh3bp4, Shf, Slamf9, Slc23a1, Snx7, Socs1, Tbc1d10a, Thap3, Tm4sf1, Tmem158, Tmsb10, Tmsb15a, Tmsb4x, Tor4a, Tpgs1, Trnp1, Tslp, Tstd1, Wbp5, Zc3h12a, Zfp771, Znhit2

9.2 Additional experimental data

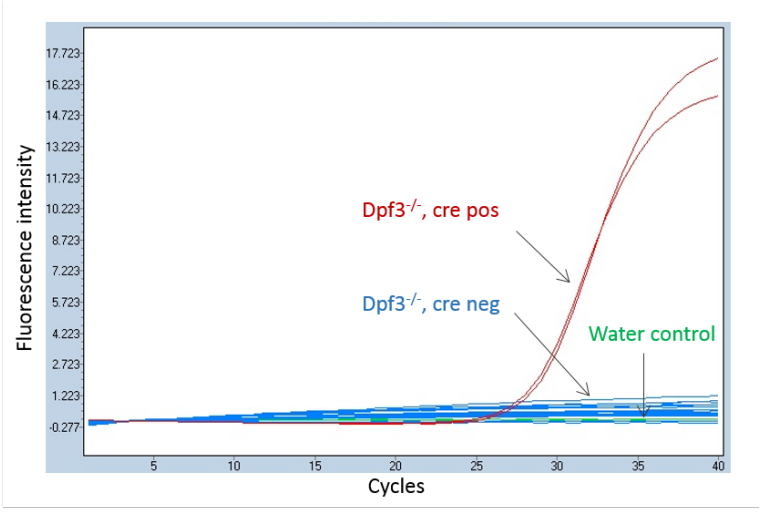

Figure 9.1: Expression of the Cre recombinase in the Dpf3$^{-/-}$ strain.

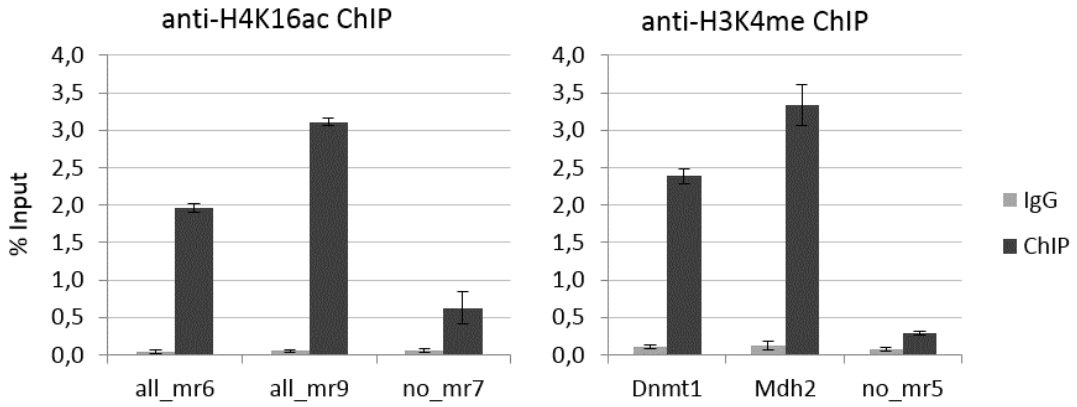

Figure 9.2: Validation of ChIPseq by qPCR. Positive controls: all_mr6, all_mr9, Dnmt1, Mdh2; negative controls: no_mr7, no_mr5.

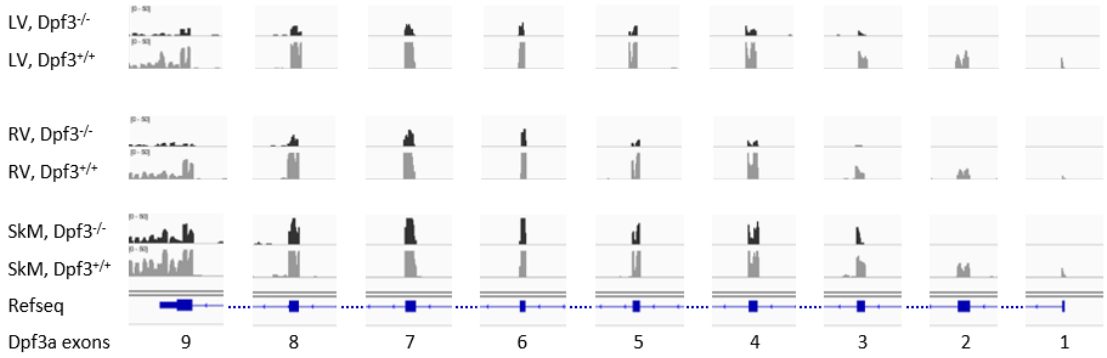

Figure 9.3: RNAseq read densities at exons of Dpf3. LV, left ventricle; RV, right ventricle; SkM, skeletal muscle.

Selbständigkeitserklärung

Hiermit erkläre ich, dass ich diese Arbeit selbständig verfasst habe und keine anderen als die angegebenen Quellen und Hilfsmittel in Anspruch genommen habe. Ich versichere, dass diese Arbeit in dieser oder anderer Form keiner anderen Prüfungsbehörde vorgelegt wurde.

Katherina Bellmann Berlin, März 2016